Dissertations, Theses, and Masters Projects   Theses, Dissertations, & Master Projects

2005

Vibrational lifetimes of hydrogen and oxygen defects in semiconductors

Baozhou Sun
College of William & Mary - Arts & Sciences

Recommended Citation

VIBRATIONAL LIFETIMES OF HYDROGEN AND OXYGEN DEFECTS IN SEMICONDUCTORS

A Dissertation

Presented to

The Faculty of the Department of Applied Science

The College of William & Mary in Virginia

In Partial Fulfillment

Of the Requirements for the Degree of

Doctor of Philosophy

by

Baozhou Sun

2005

APPROVAL SHEET

This dissertation is submitted in partial fulfillment of

the requirements for the degree of

Doctor of Philosophy
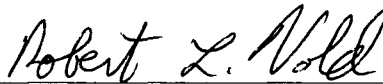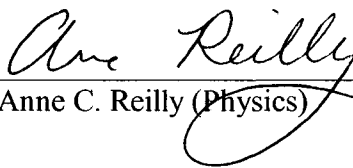
_____

(Baozhou Sun)
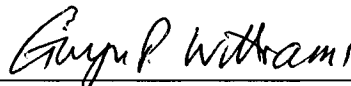
Approved, August 2005

_____
Gunter Lüpke (Advisor)

_____
Robert L. Vold

_____
Anne C. Reilly (Physics)

_____
Gwyn P. Williams (Jefferson Lab)

ii

To my parents and my wife...

Table of Contents

iv

v

vi

ACKNOWLEDGEMENTS

It is my pleasure to acknowledge dozens of people who have given me generous help through my Ph.D. study. First and foremost I would like to express my deepest thanks to Professor Gunter Lüpke, my dissertation advisor, who has guided me with wisdom and patience throughout my graduate career at William and Mary. His overwhelming knowledge and physical insight contributed invaluably to this work. I will always be grateful to him for his advice, support and guidance in this project.

I must also thank all of our collaborators. I gratefully acknowledge the advice and stimulating discussions with Dr. Feldman, Dr. Tolk and Dr. Sunkaranam at Vanderbilt University. Not only did they prepare the proton-implanted samples for me, they also invited me to Vanderbilt on two occasions for wonderful discussions. I also thank Dr. Stavola's group at Lehigh University for providing us silicon samples with low-concentration impurities, as well as the data of the linewidth measurements of local vibrational modes. Dr. Stavola has always been available and helpful to me when I needed help. I have benefited from many insightful discussions with Dr. Pajot in Paris and Dr. Newman in Imperial College London. Particular thanks go to Dr. Pajot for providing silicon samples with oxygen isotopes. I have been fortunate in having so many intelligent scientists to discuss and work with in various projects. Without these collaborators, it is impossible for me to finish this work.

I wish to thank Dr. Xinhui Zhang, who taught me so much about aligning optics in the first year. I would also thank Dr. Qiguang Yang for his help in the nonlinear optics and assistance in the lab. I have learned things of value from the other group members and lab mates including Dr. Yuhang Ren, Haibin Zhao, Shuyang Zhang, Dr. Diyar Talbayev and Dr. Andrea Lucarelli. It is always a pleasure to work with them.

I would like to express my appreciation to the rest of my committee members: Dr. Robert L. Vold of Applied Science, Dr. Anne Reilly of Physics and Dr. Gwyn Williams of Jefferson Lab. I especially appreciate their encouragement during my study at William and Mary and their instructive comments on my thesis.

I also extend my gratitude to the staff at the TJNAF FEL who have given their beam time and equipments for our experiments, and in particular, Joe Gubeli and Dr. Michelle Shinn were always available when I needed their help. I want to thank Prof. Michael Kelley who let me use his FTIR spectrometer many times, and thank him for his encouragement in my career. Thanks also go to Amy Wilkerson at Applied Research Center who always offers me her support on any favor I asked.

I must thank my parents in China for their dedicated love and affectionate encour-

viii

agement throughout my stay in the USA. I also want to express my sincere gratitude to the brothers and sisters in Peninsula Chinese Baptist Church for their love, support and prayers in Jesus Christ.

No words can express how grateful I am to my wife, Min Huang for her sacrifices, understanding, and patience. I would never have finished this Ph.D.work without your undying love and endless care throughout our stay at William and Mary. This dissertation is dedicated to her.

Lastly but most importantly, I thank God for giving me strength and courage to endure and for leading me on this path and illuminating the way even when it is difficult to go through sometimes.

List of Tables

List of Figures

xii

xiii

xiv

ABSTRACT

Characterization of defect and impurity reactions, dissociation, and migration in semiconductors requires a detailed understanding of the rates and pathways of vibrational energy flow and of the coupling mechanisms between local modes and the phonon bath of the host material. Information on the inelastic microscopic interaction can be obtained by measuring the lifetime of local vibrational modes (LVMs). This dissertation presents vibrational lifetime measurements of hydrogen and oxygen defects in semiconductors by means of time-resolved infrared (IR) pump-probe spectroscopy. In these experiments, a picosecond IR pulse excites a vibration of a significant fraction of point defects in a sample. This excitation causes a transient decrease in the absorbance of the sample, as there are fewer defects in the vibrational ground state that can absorb. The transmittance change is measured with a weaker probe pulse that passes through the sample after a variable delay, so that the evolution of the excited vibration can be followed in time. This technique enables the direct time-domain measurement of the lifetime of LVMs.

First, we measured the vibrational lifetime of H- and D-related bending modes in Si and other semiconductors. Time-resolved pump-probe and linewidth measurements reveal that the lifetime of bending modes can be explained by an energy gap law, i.e., the decay time increases exponentially with increasing decay order.

Second, we present the vibrational lifetime measurements of a selection of Si-H stretch modes in crystalline Si. The lifetimes of interstitial-type defects are found to be a few picoseconds, whereas vacancy-type defects have lifetimes up to 300 picoseconds. The strong dependence of lifetime on the defect structure suggests that pseudolocalized modes are involved in the vibrational relaxation of the hydrogen stretch modes in Si. It is found that the energy relaxation of Si-H stretch modes does not decay by lowest order, i.e., low frequency modes are involved in the decay process.

Furthermore, we performed lifetime measurements of interstitial oxygen in Si and Ge. The lifetime of $^{17}O_i$ in Si is half of $^{16}O_i$ and $^{18}O_i$. A calculation of the three-phonon density of states shows that $^{17}O_i$ lies in the highest phonon density resulting in the shortest lifetime. The lifetime of the $^{16}O_i$ mode in Ge is measured to be 10 times longer than in Si. The interaction between the local modes and the lattice vibrations is discussed according to the activity of phonon combination.

These studies elucidate the dynamics of energy dissipation and vibrational decay channels of point defects in semiconductors. They provide a better understanding of the dissociation of Si-H and Si-O bonds and the strong hydrogen and deuterium isotope effect found in H-passivated semiconductor devices. The experimental results provide an indispensable benchmark for future theoretical investigations.

xviii

VIBRATIONAL LIFETIMES OF HYDROGEN AND OXYGEN DEFECTS IN SEMICONDUCTORS

Chapter 1

Introduction

1.1   Light Impurities in Semiconductors

Group IV element semiconductors such as silicon and germanium were identified as the most promising materials in semiconductor industry. Most electronic and optical properties of these semiconductors are determined by the type and concentration of defects they contain. Many defects are present in as-grown semiconductors. They include intrinsic defects (self-interstitial and vacancies) and extrinsic defects or impurities which come from the source materials, the ambient, the crucible, the heating element, etc. Defects may also be introduced during processing of the devices: Etching injects vacancies as well as hydrogen, the growth of layers causes self-interstitial and vacancies in the bulk, ion plantation creates damage [1]. Figure 1.1 shows a simple structure of intrinsic and extrinsic defects in crystalline solids.

The addition of these impurities to a semiconductor will alter its vibrational and electronic properties. For example, dopants can add charge carriers (electrons e^- to the conduction band or holes h^+ to the valence band), which will form an e^-- h^+

2
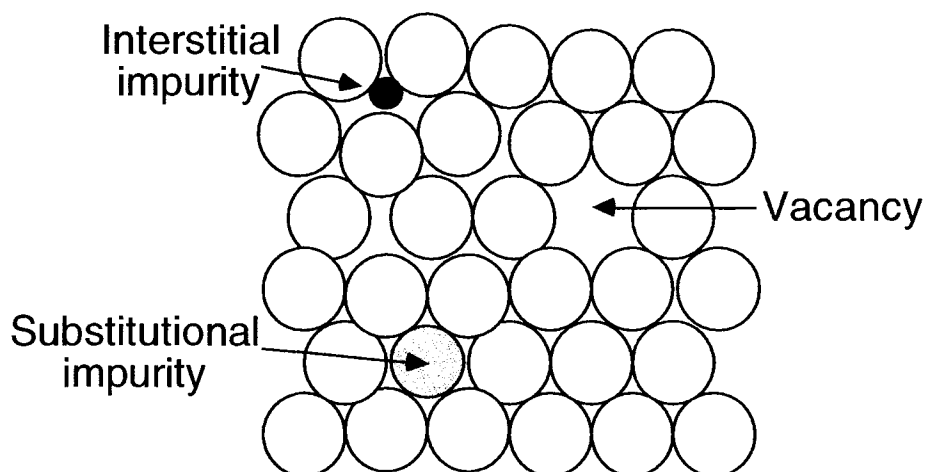
Figure 1.1: Point defects in crystalline solids.

recombination center and reduce carrier lifetimes. In general, defects or impurities break the periodicity of the crystal, introduce local strain, and result in new energy levels which are often in the gap. Depending on the Fermi level and the position of defect level, some defects may exist in several charge states. Furthermore, defects can be mobile, leading to a wide range of reactions between them. Such reactions create new, more complicated, defects with different electronic and optical properties than the original one. Defect diffusion and reaction is enhanced by thermal treatments.

Since defects are very important in semiconductors, it is crucial to understand their fundamental properties, including how they diffuse, interact with the crystal, with each other, and with other defects. The most common impurities in semiconductors are hydrogen and oxygen, which have been of interest for many years because of their simple atomic structures. Experimentally, many techniques are used

to probe their microscopic properties. Fourier transform infra-red (FTIR) absorption and Raman spectroscopy are used to study local vibrational modes (LVMs). Electron paramagnetic resonance (EPR) is a technique to find unpaired electron spins. Deep-level transient spectroscopy (DLTS) is used to probe the gap for defect levels. More macroscopic methods such as secondary-ion mass spectroscopy (SIMS) also provide crucial information. Recently, time-resolved pump-probe experiments have been performed to provide new information about the dynamics of these defects.

1.1.1 Hydrogen

Hydrogen is the simplest element in the periodic table considering the atomic structure. However, hydrogen has very rich chemical properties and forms more molecular compounds than any other element [2].

Hydrogen is a very common impurity in semiconductors. It can be incorporated during crystal growth or processing steps such as wafer polishing, wet chemical etching, or reactive ion etching [3]. It is present at virtually every stage of the processing of devices. This makes it an unavoidable impurity even in devices fabricated with the most perfect single crystals. The solubility of hydrogen in semiconductors is low. For example, the solubility of hydrogen in intrinsic silicon is $\sim 6 \times 10^{15}$ cm^{-3} ($\sim 10^{-2}$ ppm) at 1200°C [4] and $\sim 10^6$ cm^{-3} ($\sim 2 \times 10^{-12}$ ppm) at 300°C [4, 5]. However, the effective solubility at moderate temperatures is determined by the concentration of hydrogen traps, e.g., dopants, dangling bonds, etc., and exceeds the intrinsic value

by several orders of magnitude. Early high-temperature permeation data showed that hydrogen is a rapid diffuser in silicon with the diffusivity

$$D_H = (9 \pm 4) \times 10^{-3}\exp[-\frac{0.48 \pm 0.06eV}{k_bT}]\text{cm}^2/\text{s} \qquad (1.1)$$

in temperature range of 970-1200°C [4]. This high diffusivity is observed only at high temperature or with low impurity concentration, where trapping of hydrogen is negligible. The effective diffusivity is typically several orders of magnitude smaller than the value given by Eq. (1.1). The effect of hydrogen on a semiconductor device can be harmful, or in other cases, beneficially. Hydrogen may also be deliberately introduced. For example, hydrogen annealing is performed as the last step of polycrystalline-silicon solar-cell processing. This boosts the performance of these cells by a substantial amount [6]. Because hydrogen is so important in semiconductor industry, a large amount of work has been done during the last three decades. The properties of hydrogen in semiconductors have been discussed in many recent reviews [3, 6, 7, 8, 9].

When hydrogen is used to passivate deep and shallow defects in semiconductors, it behaves as an amphoteric impurity; that is, it acts as a donor (H^+) in p-type material and an acceptor (H^-) in n-type material. The charge state determines the most favorable location of hydrogen in the lattice. In the positive charge state (H^+) the impurity is essentially a proton. Since the maximum negative charge density is found at the bond-center (BC) site in most covalent semiconductors, H^+ locates at this site [10]. In the negative charge state (H^-) hydrogen prefers regions of low

electronic charge density, in which its distance to the host atoms is maximized. So H^- was found at the tetrahedral interstitial site. Based on the calculations by Van De Walle [10], neutral hydrogen was also found at the BC site, but it is less stable than H^+ at this site.
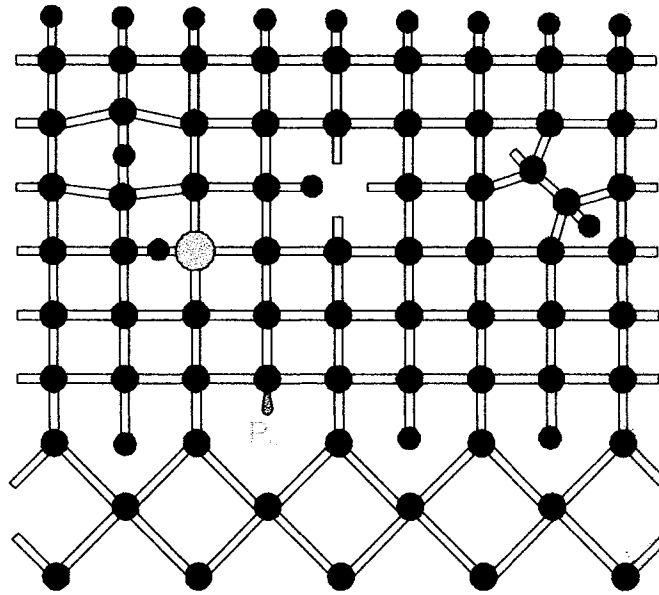
Figure 1.2: Hydrogen defects in semiconductor.

Hydrogen can form strong covalent bonds with many other elements in the periodic table which makes it a very diverse impurity. Hydrogen interacts with virtually any imperfection in the crystal such as impurities, intrinsic defects, interfaces and surfaces. Figure 1.2 shows a two-dimensional illustration of hydrogen defects in semiconductor. The major role of hydrogen is the passivation of both shallow and deep impurity centers and other defects through the formation of complexes. On the surface, H forms covalent bonds with silicon dangling bonds [11]. In the bulk, H forms all

kinds of interstitial, self-interstitial, vacancy-type defects or complexes with other impurities [11]. At the interface, H passivation can reduce the density of P_b centers, which is crucial in semiconductor devices [12]. For example, hydrogen saturates dangling bonds at surfaces [13] and at Si/SiO_2 interfaces [14, 15], which generally removes the electronic levels associated with the dangling bond from the band gap and thus neutralizes its electrical activity. These H-related defects have been well characterized [3, 16].

Hydrogen can also interact with each other and form two types of hydrogen dimer called H_2 molecule and H_2^*. The H_2 molecule locates at a tetrahedral site and its existence in silicon was first predicted by Corbett *et al* [17] in 1983 and confirmed by observation of an H-H vibrational mode with Raman spectroscopy [18] and infrared absorption spectroscopy [19]. Recently, it was proposed that the H_2 molecule behaves as a nearly free rotor [20]. Another hydrogen dimer structure H_2^* has C_{3v} symmetry with one hydrogen close to the bond-center site and the other at an antibonding site. The existence of H_2^* has been predicted by Chang [21] and confirmed by Holbech [22]. Figure 1.3 shows the structure of these two dimers. The H_2 molecule in Si was suggested to be oriented approximately along a $\langle 100 \rangle$ direction and has a symmetry of C_1 point group [23, 24]. H_2^* defect has C_{3v} symmetry with one hydrogen close to the bond-center site and the other at an antibonding site.
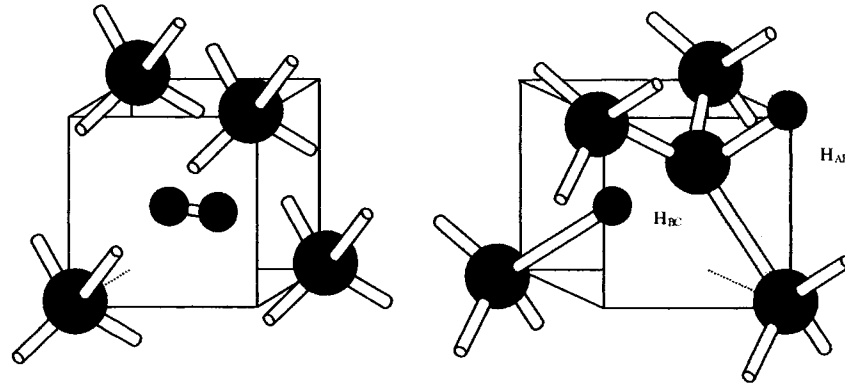
Figure 1.3: (a). Representative model for H_2 in Si proposed by Zhou and Stavola [23]. (b). Structure of H_2^* defect in Si proposed by Holbech [22].

1.1.2 Oxygen

At present about 80 % of all the silicon wafers used for microelectronic circuit fabrication are prepared by the Czochralski (CZ) method or its modification. These silicon wafers contain oxygen on the order of 10^{18} atoms/cm^3. Oxygen impurities critically affect the properties and yield of electronic devices because of the effects on the mechanical and electrical properties of the wafers as well as on the lattice defects incorporated. During the last four decades both academy and industry have devoted a great deal of attention to the investigation of oxygen in silicon [25].

Oxygen is mainly introduced during crystal growth by the CZ pulling technique from a silica crucible. By means of infrared absorption spectroscopy, Kaiser, Keek, and Lange first confirmed that CZ silicon crystals contain oxygen as an impurity in concentration on the order of magnitude higher than usual doping impurities [26]. They found that oxygen atoms incorporated into silicon dominantly occupy the in-

terstitial site, which lies midway between two neighboring silicon atoms along the four equivalent ⟨111⟩ bond directions. The structure is shown in Figure 1.4. Oxygen is located into an off-axis bond-centered position, giving rise to a strong absorption band at 1136 cm^{-1}. Early X-ray diffraction measurements showed that the lattice parameter a_0 is increased when oxygen is present [27]. Due to the high concentration of oxygen in Si, annealing silicon can produce the precipitation of oxygen into various forms of silica (SiO_2) precipitates. This process is reversible and oxygen can be dispersed again by dissolution of the precipitates at very high temperature ($\sim$1300-1350°C). A discussion of the relationship between the shape of the precipitates and their infrared absorption has been given in Reference [28].
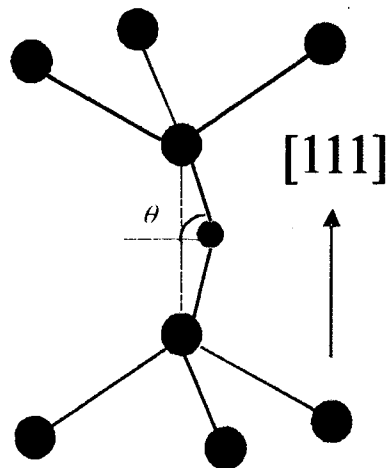
Figure 1.4: Structure of intersititial oxygen in Si and Ge.

Group VI doping elements O, S, Se and Te are double donors in silicon [29]. This electrical activity is explained by a substitutional location of these elements in the

same way as the single donor electrical activity of P, As, or Sb. As-grown CZ silicon displays n-type electrical activity related to oxygen [30]. This n-type behavior comes indeed from a series of donors, which are called thermal donors (TDs). Oxygen could act as a double donor on a substitutional site. This location is unstable because of the small tetrahedral radius of the oxygen atom (0.68 Å), but it has been argued that TDs could be due to substitutional oxygen surrounded by interstitial oxygen to compensate an inward distortion by an outward distortion [31]. The total oxygen concentration of these TDs is typical less than 1% of the total oxygen concentration in as-grown silicon. The study of thermal donors is a very active area of oxygen in semiconductors. Detailed information can be found in some reviews [25]. This thesis will include the studies of vibrational dynamics and oxygen isotope effects in Si and Ge by time-resolved infrared spectroscopy.

1.2 Local Vibrational Modes

In a crystalline semiconductor, atoms collectively oscillate about their equilibrium positions, resulting in quantized vibrational modes, or phonons [32]. Phonons in crystalline materials have a band of phonon frequencies and can propagate through the lattice. In a perfect lattice, phonons have a well-defined frequency w and wave vector q. The w vs q dispersion relation can be experimentally determined by neutron scattering [33]. Most of the phonon modes are Raman active. When an impurity is introduced, the translation symmetry is broken and one or more new vibrational

modes may appear. If an impurity replaces a heavier host atom, its vibrational frequency will be higher than the phonon frequency. Unlike the phonon, the vibrational modes of point defects cannot propagate in the crystal and remain localized near the defects. Hence they are called local vibrational modes or LVMs. The physical description of local vibrational modes closely resembles that of molecular vibrations, except that point defects do not have rotational degrees of freedom. These defects can also induce a dipole moment which makes the vibrational mode infrared active. Much information has been gained from infrared absorption studies of local vibrational modes because they can generally be observed as sharp lines on a monotonous background.

1.2.1 Local Vibrational Mode Spectroscopy

Local vibrational mode spectroscopy has become an important probe of defects in solids and often provides information about defect structures and properties that cannot be obtained by other methods. This technique has been applied extensively to study isolated impurities and impurity complexes in crystalline solids, including ionic crystals [34] and semiconductors [16].

A local vibrational mode interacts with light by absorption and/or Raman scattering. At low temperatures, the population of the excited states of local vibrational modes is negligible. The local mode is infrared active if the light-induced transition is allowed between vibrational states. The transition probability is proportional to the

square matrix element of the electric dipole moment $|\hat{e} \times \mu_{if}|^2$. Here $\hat{e}$ is a unit vector in the direction of the polarization of the light and μ_{if} is the matrix element of the electric dipole moment of the center between the initial and final vibrational states. For harmonic vibrations, a mode is infrared active if the motions of the defect atom or atoms give rise to a change in the dipole moment of the center. Consider the simple example of a linear defect of the form X-Y-X. Their symmetric vibrational mode in which the Y atom is stationary and the X atoms vibrate 180° out of phase is infrared inactive because there is no net oscillating dipole moment (shown in Figure 1.5(a)). The antisymmetric mode in which the X atoms vibrate in phase with each other and opposite to the direction of Y has an allowed electric dipole transition (shown in Figure 1.5(b)). Furthermore, the vibrational mode will only be excited by incident light that has a component of its electric vector polarized along the direction of the oscillating dipole moment. For the simple example of the antisymmetric stretching mode of a linear defect molecule, the direction of the oscillating dipole moment is along the axis of the defect molecule.

Figure 1.5: Schematical description of infrared activity of local vibrational modes.

The integrated absorption coefficient for a defect is well known to be proportional to the concentration of the defect. The commonly used expression for the integrated absorption strength for the local modes of an oscillating defect with mass m and an effective charge q is given by

$$\int \alpha(\sigma)d\sigma = \frac{\pi q^2 N}{\mu \eta c^2},$$ (1.2)

where N is the concentration of defects in cm^{-3}, and η is the refractive index of the host. This equation has been written in CGS units to be consistent with the absorption coefficient, which is conventionally determined in units cm^{-1} and the frequency σ given in wavenumber units, cm^{-1}. An infrared absorption experiment typically allows one to determine the intensity of the absorption line, i.e., the area under the absorption peak. The reduced mass μ is given as [35]

$$\mu^{-1} = \mu_{imp}^{-1} + (\chi \mu_{host})^{-1},$$ (1.3)

where μ_{imp} and μ_{host} are the atomic masses of impurity and host atoms, and χ is a parameter which represents the coupling of the vibrating entity to the crystalline host. The χ parameter depends on the structure of the defect but is presumable close to unity for hydrogen-related local modes in Si and Ge. The frequency and width of an infrared absorption line associated with a local vibrational mode depend on the sample temperature at which the measurement is carried out. The frequency shifts to higher wavenumber and the line becomes sharper with decreasing temperature.

Raman spectroscopy is complementary to infrared absorption spectroscopy and can provide information about vibrational modes that are infrared inactive. For Raman scattering measurements of local vibrational modes, a monochromatic laser beam is incident on a sample. The light is inelastically scattered by the excitation of the crystal. Measurements are usually made at low temperatures and only Stokes scattering processes that excite impurity vibrations have appreciable intensity [16]. In this case, the frequency of light ω_s scattered from local vibrational modes satisfies the relationship

$$\omega_S = \omega_L - \omega_{LVM}, \tag{1.4}$$

where ω_L and ω_{LVM} are the laser and local modes frequencies, respectively. Thus the local modes can be detected from their Raman shifts. Since Raman scattering is a second-order process in perturbation theory, it is subject to different selection rules than electric-dipole allowed optical transitions. The Raman intensity is proportional to $|\hat{e}_S \times \boldsymbol{R} \times \hat{e}_L|^2$, where $\boldsymbol{R}$ is the second-order Raman tensor and $\hat{e}_S$ and $\hat{e}_L$ are unit vectors in the polarization directions of the scattered and incident light.

1.2.2 Dynamics of Local Vibrational Modes

Most spectroscopy studies of LVMs in semiconductors have been carried out in the frequency domain, which probes the time-averaged optical response of the modes. The interaction between local modes and phonons has been studied by temperature dependence of linewidth and frequency shift. As temperature increases, phonon modes are

thermally populated. Two models have been used to understand the coupling between the local modes and phonon bath [32]. These studies are very limited to understand the relaxation process of defects because inhomogeneous broadening may contribute significantly to the observed absorption linewidth. The energy relaxation time cannot be derived from the line width of the linear absorption spectrum [36, 37]. Until now very little was known about the dynamics of local vibrational modes in crystalline semiconductors. The time scales and mechanisms for population and phase relaxation upon excitation were still unknown. The dynamics of local modes is responsible for the flow of energy into and out of impurities and defect complexes. Understanding the dynamics of defects is important for defect migration and reaction. When defects act as recombination or scattering center in semiconductors, the electronic excitation that is deposited at the defects is then available to promote defect migration and reaction. Such information is crucial since excited vibrational states may be involved in the dissociation of the bond between defects and the lattice [38]. This investigation is made possible only recently by the advances in tunable, ultrafast, high-intensity infrared light sources, including optical parametric amplifiers (OPAs) [39, 40] and free-electron lasers (FELs) [41, 42]. The time scale of energy relaxation and dynamics of the elastic and inelastic local interaction can be obtained directly by pump-probe transient bleaching spectroscopy. This dissertation focuses on time-resolved dynamical studies of hydrogen and oxygen defects in silicon and germanium.

1.3 Outline

In Chapter 2, we discuss the important theories for vibrational relaxation dynamics of local vibrational modes. We discuss the relationship between vibrational lifetime and linewidth, multiphonon relaxation, energy gap law, and symmetry of accepting modes.

In Chapter 3, we describe the experimental techniques including FTIR and pump-probe spectroscopy, together with the method for generating short mid-infrared pulses. In Chapter 3, we also give a brief introduction for doing experiments with the Free Electron Laser at Jefferson Lab.

In Chapter 4, we present the first study of the vibrational lifetime of hydrogen bending modes in semiconductors. Time-resolved pump-probe and linewidth measurements reveal that the lifetime of hydrogen bend modes can be explained by an energy gap law, i.e., the decay time increases exponentially with increasing decay order. This study provides a better understanding of the dissociation of Si-H bonds and the strong hydrogen and deuterium isotope effect found in H-passivated devices.

In Chapter 5, we present measurements of the vibrational lifetime of H-related stretch modes in crystalline silicon. The vibrational lifetimes are found to be strongly structure dependent. The interstitial-type defect H_2^* has a lifetime of 4.2 ps at 10 K, whereas the lifetime of the vacancy-type complex $HV \cdot VH_{(110)}$ is 2 orders of magnitude longer (~ 270 ps). The decay channel and relaxation dynamics are also discussed in Chapter 5.

In Chapter 6, we focus on the study of the lifetime of interstitial oxygen and its isotope effects in silicon and germanium. The linewidth of the $^{17}O_i$ mode in Si is two times broader than the corresponding $^{16}O_i$ and $^{18}O_i$ mode. This difference is also observed by time-resolved pump-probe spectroscopy. The lifetimes of interstitial $^{16}O_i$ and $^{17}O_i$ isotopes in Si are measured at 10 K to be 11.5 and 4.5 ps, respectively. We also calculate the three-phonon density of states and found that the ^{17}O mode lies in the highest phonon density resulting in the shortest lifetime, which explains the isotope effect. The lifetime of the $^{16}O_i$ mode in Ge was measured to be 125 ps, i.e., 10 times longer than in Si. The interaction between the local modes and the lattice vibrations is discussed according to the activity of phonon combinations.

In Chapter 7, the last chapter of this dissertation, we give a summary and outlook for future experiments.

Chapter 2

Theoretical Considerations

In this chapter, we present the theoretical description of the vibrational dynamics of local vibrational modes. First, the relationship between vibrational relaxation and linewidth is described. A short introduction to the existing theory of multiphonon relaxation process is given. We will also discuss the important factors which determine the vibrational lifetime of LVMs, including energy gap law, anharmonicity, and symmetry of accepting modes.

2.1 Vibrational Relaxation and Linewidth

Relaxation processes are usually divided into two classes. Figure 2.1 schematically describes the two relaxation processes. The first class is called population relaxation, which changes the quantum number of the LVM, thus causing the states to have finite lifetimes. T_1 characterizes the time scale of energy relaxation of the first excited state. In the low temperature limit the homogeneous absorption linewidth of a LVM is determined by the uncertainty relation. Given the excited state lifetime T_1, the

18

natural linewidth is

$$\Gamma = \frac{1}{2\pi c T_1} \tag{2.1}$$

Population relaxation

Phase relaxation

Characteristic time: T_1

Characteristic time: T_2^*
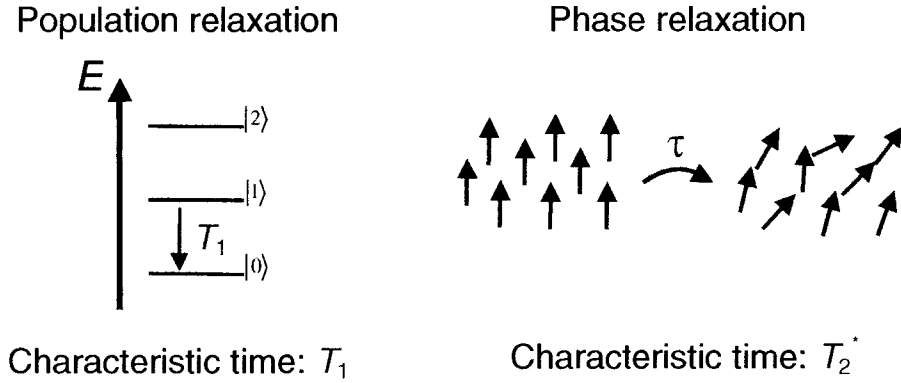
Figure 2.1: Schematic description of the two common relaxation processes: Energy relaxation and pure dephasing.

The second class of relaxation processes are caused by interactions that conserve the quantum number of the LVM, but cause a loss of phase coherence. These are elastic scattering processes which do not contribute to population or energy relaxation. This process is also called pure dephasing. The lifetime of pure dephasing is characterized by T_2^*. The total dephasing time T_2 is determined by both the pure dephasing processes and the energy decay time. The homogeneous linewidth is given by

$$\Gamma = \frac{1}{2\pi c T_1} + \frac{1}{\pi c T_2^*}. \tag{2.2}$$

Since these processes involve exponential decay, the corresponding absorption line shapes are Lorentzian, which is the Fourier transform of an exponential function. In the low temperature limit, the linewidth caused by pure dephasing can be neglected.

At higher temperatures, elastic phonon scattering becomes thermally activated which results in homogeneous dephasing broadening of the absorption line.

In many cases, the line shape is dominated by inhomogenous broadening. In an amorphous host or a crystal solid with high concentration of impurities, each impurity may experience a slightly different local environment. This can affect the vibrational frequency of the LVM through slightly different interactions with the surrounding host atoms. This leads to additional broadening of a LVM. This broadening is referred to as inhomogeneous broadening, which is always occurring in surface vibrations and amorphous host. For example, the lifetimes of Si-H stretch modes were believed to be in the nanosecond range based on direct measurements of the lifetime of Si-H bonds on H-terminated surfaces [43]. Such lifetimes correspond to natural linewidths on the order of 0.005 cm^{-1}, much less than the widths usually observed for LVM's in semiconductors. Knowledge of the linewidth is not sufficient to understand the dynamics of LVMs in semiconductors. However, by decreasing the concentration of H impurities in a crystalline Si sample, Budde *et al* found that the inhomogeneous linewidth can be eliminated or neglected when the concentration of impurities is reduced down to 1 ppm [44]. Based on Budde's observation, at low temperature and low defect concentration the linewidth of a LVM measured in a crystalline semiconductor is a good estimate of its vibrational lifetime.

2.2 Multiphonon Relaxation and Energy Gap Law

The theoretical description of vibrational energy relaxation can be very complicated. The vibrationally or electronically excited impurities in a crystal can, in principle, decay into photons, electronic degrees of freedom, or other vibrational modes. The radiative lifetime can be estimated to be of the order of milliseconds [45], which rules out radiative decay as the dominating mechanism. Electronic decay can also be ruled out in undoped Si and Ge, because the H- or O-related defects studied here cannot introduce shallow electronic levels in the bandgap. Consequently, electronic transitions require more energy than that of local vibrational modes. It is most likely that the LVM decays into vibrational modes of the system consisting of phonon bath or other low frequency modes. If the vibrational relaxation process involves transferring energy directly to the phonons in a single step, and the amount of energy transferred exceeds by many times the maximum energy of a single phonon, then many phonons will have to be created simultaneously. This process is know as *multiphonon relaxation* [46]. One might reasonably imagine that the rate of such a high-order process would be quite small. Therefore, it is remarkable that even if the number of phonons emitted is as high as ten or more, multiphonon processes typically compete successfully with radiative decay, and are in fact often the dominant relaxation mechanism.

Given the wide use and the general importance of multiphonon relaxation, a theory of relaxation rates based on a microscopic Hamiltoniam is clearly desirable. Existing theories involve one of two approaches: The adiabatic (Born-Oppenheimer) or

"Static-coupling"(Crude Born-Oppenheimer) methods. The first method is ususally invoked when discussing relaxation between electronic states, but can be applied to high-frequency vibrations as well. The coordinates are divided into fast (electronic or high-frequency vibration) and slow (phonons) components. One neglects for the moment the kinetic energy of the phonons, and finds the eigenstates of the Hamiltonian for fixed phonon coordinates. The eigenvalues of this procedure generate the usual adiabatic potential surfaces, and transitions between these surfaces are due to the "non-adiabatic" coupling (phonon kinetic energy) term in the full Hamiltonian. Even when this non-adiabatic coupling is taken to lowest order in perturbation theory, multiphonon transitions emerge. This was the approach pioneered by Kubo and Toyozawa [47], Perlin [48], Miyakawa and Dexter [49],and others [50, 51, 52, 53, 54, 55].

The second approach goes by several different names but its essence is as follows: One assumes that the Hamiltonian can be written as

$$H = H_S + H_B + H_I. \tag{2.3}$$

H_S is the Hamiltonian for the LVM (two-level system) of the impurity,

$$H_S = \hbar \omega a^\dagger a, \tag{2.4}$$

where ω is the vibrational frequency, $a^\dagger$ and a are the creation and annihilation operator, respectively. H_B is the Hamiltonian of the bath (phonons), which is given

by

$$H_B = \sum_k \hbar\omega b^\dagger b, \tag{2.5}$$

where $b^\dagger$ and b are the phonon creation and annihilation operator, respectively. In the most common approach, H_I is strictly off-diagonal in the two-level basis of the local vibrational mode [46, 56, 57]. The off-diagonal matrix elements of H_I are expanded to high order in the phonon coordinates, and are treated by lowest-order time-dependent perturbation theory. The interaction Hamiltonian is then given by

$$H_I = \sum_{\{\nu\}} \hbar(G_{\{\nu\}}B_{\{\nu\}}a^\dagger + G^*_{\{\nu\}}B^\dagger_{\{\nu\}}a), \tag{2.6}$$

where $B_{\{\nu\}} = \Pi^{N_\nu}_{i=1}B_{i,\{\nu\}}$, $B^\dagger_{\{\nu\}} = \Pi^{N_\nu}_{i=1}B^\dagger_{i,\{\nu\}}$, and $G_{\{\nu\}}$ denotes the temperature-independent coupling strength of the channel $\{\nu\}$. $\{\nu\}$ is characterized by the set $\{\omega_1^{\{\nu\}}, \omega_2^{\{\nu\}}, \ldots, \omega_{N_{\{\nu\}}}^{\{\nu\}}\}$ of accepting mode frequencies. Energy is conserved in the decay process and the frequency sum is

$$\omega = \sum_{j=1}^{N_\nu} \omega_j^\nu. \tag{2.7}$$

The contribution of the decay rate due to H_I is given by the standard result of first-order time-depended perturbation theory [58]. The total decay rate (inverse lifetime) is given as the sum of the rates of all of the decay channels [46, 56, 57]:

$$\gamma = \frac{1}{T_1} = 2\pi \sum_{\{\nu\}} |G_{\{\nu\}}|^2 n_{\{\nu\}} \rho_{\{\nu\}}. \tag{2.8}$$

The function $n_{\{\nu\}}$ describes the temperature-dependent population of the receiving modes:

$$n_{\{\nu\}} = \frac{exp(\frac{\hbar\omega}{K_bT}) - 1}{\prod_{j=1}^{N_\nu}[exp(\frac{\hbar\omega_j^{(\nu)}}{K_bT}) - 1]}. \tag{2.9}$$

The compound spectral density of accepting states, $\rho_{\{\nu\}}$, can be expressed in terms of a convolution of single spectral densities of states:

$$\rho_{\{\nu\}} = \int d\omega_1^{(\nu)} \ldots \int dw_{N_\nu-1}^{(\nu)} \rho_1^{(\nu)}(\omega_1^{(\nu)}) \ldots \rho_{N_\nu}^{(\nu)}(\omega_{N_\nu}^{(\nu)}). \tag{2.10}$$

In the low-temperature limit $(K_bT \ll \hbar\omega_j^{(\nu)})$, the decay rate reflects spontaneous decay into N_ν accepting modes and $n_{\{\nu\}} \cong 1$. At higher temperatures the decay rate increases due to stimulated emission in a fashion determined by the frequencies of the accepting modes [46, 56, 57].

The general expression for the vibrational relaxation rate Eqs. (2.8) and (2.9) consists in general of a large number of terms corresponding to higher order multiphonon processes. The relaxation rate is determined by the magnitude of the coupling terms between local vibrational modes and accepting modes. It is reasonable to assume that the $|G_{\{\nu\}}|^2$ terms decrease fast with increasing order of the multiphonon process $N_{\{\nu\}}$. As $G_{\{\nu\}}$ is expected to exhibit a very strong dependence on $N_{\{\nu\}}$, the relaxation rate can be approximately expressed by the dominant contribution. The largest term in Eq. (2.8) is determined by the collection of phonon states $\{\nu\} = 1, 2, \cdots, N_{\{\nu\}}$, where $N_{\{\nu\}}$ is the smallest number of phonons that can result in a vibrational relaxation process subjected to the energy conservation [57]. The approximate expression for

the vibrational relaxation rate is now

$$\gamma \simeq \pi |G_{\{\nu\}}|^2 \rho_{\{\nu\}} n_{\{\nu\}}.$$ (2.11)

In very good approximation [57], the coupling constant can be expressed as $G_{\{\nu\}} \simeq$ $C\delta^N$, where C is a constant, $0 < \delta \ll 1$, and N is the decay order which is determined by the energy gap between local vibrational modes and phonon modes. Such a relation together with Eq. (2.11) implies that $\gamma \propto \delta^{2N}$ (at constant T). A phenomenological approach to the energy-gap dependence of relaxation rate γ has been developed in Reference [46, 59, 60]. It is generally believed that the relaxation rate decreases exponentially as the energy gap is increased. The energy gap law can be expressed by

$$T_1 = A exp(B \cdot N),$$ (2.12)

where A and B are two parameters which depend on the coupling constants between LVM and accepting modes.

2.3 Anharmonicity

The decay of LVMs into other modes is an anharmonic process. So the anharmonicity of the defect potential will play an important role in the vibrational lifetime of LVMs. The impurities do not reside in a perfectly parabolic potential, rather, the potential becomes weaker for larger displacements. The interaction between the defect and the

lattice can be described by a Morse potential [61], which is given by

$$V(z - z_e) = D_e\{exp[-2\alpha(z - z_e)] - 2exp[\alpha(z - z_e)]\}, \qquad (2.13)$$

where z_e is the equilibrium value of the vibrational coordinate z, and D_e is the binding energy. The Schrödinger equation can be solved exactly for the Morse potential to give the vibrational frequencies

$$\omega(n) = \omega_e(n + \frac{1}{2}) - \omega_e\chi_e(n + \frac{1}{2})^2, \qquad (2.14)$$

where $\omega_e = \alpha(\hbar D_e/\pi c\mu)^{1/2}$, $\omega_e\chi_e = \hbar\alpha^2/(4\pi c\mu)$ and μ is the reduced mass. The observed fundamental frequency is given by $\omega = \omega_e - 2\omega_x\chi_e$. The second harmonic frequency is given by $\omega_{2nd} = 2\omega_e - 6\omega_e\chi_e$. So the anharominicity parameter can be given by

$$\chi_e = \frac{2\omega_1 - \omega_{2nd}}{2(3\omega_1 - \omega_{2nd})}. \qquad (2.15)$$

The anharmonicity can be estimated from the overtone and fundamental vibrational frequencies. This simple model has been used to explain the difference in the lifetime of VH_4 and VD_4 complexes qualitatively [62]. The D-related stretch mode in VD_4 has smaller vibrational amplitude, which gives rise to smaller anharmonicity and longer vibrational lifetime than VH_4 stretch mode in Si.

2.4 Symmetry of Accepting Modes

In the discussion of the decay process of LVMs, there can be no coupling between vibrational modes belonging to different irreducible representations [63]. That is, to ensure nonzero anharmonic coupling coefficients, the symmetry representation of the high-frequency local mode is required to contain the same irreducible representation of the exchange mode or combination of low-frequency modes. More generally, the Kronecker product of the two irreducible representations has to contain the totally symmetric representation of the space group [64]. So a full-scale space group analysis of the symmetry of local modes and the accepting modes is necessary to understand the coupling between them. Group theory is often employed as a method to determine the symmetry of the normal modes and their optical activity. The first step is to establish the symmetry of the modes such as rotations, reflections and inversions, which leave the system invariant. For a perfect crystal system which has translation symmetry, space groups must be considered [65]. The symmetry of the normal modes can be classified into different groups, which is characterized by character tables. Space group theory allows classification of the local modes and the delocalized states in crystalline solids (electrons, phonon, etc.) with respect to irreducible representations. The introduction to group theory is given in the books by Cardona [66] and Kuzmany [67]. This section focuses on the selection rules of the decay of LVMs.

Quantum-mechanical selection rules determine the transition probability for a

system changing from a state i to f. The relevant quantity is the matrix element

$$M_{f,i} = \langle \Gamma_f | \Gamma_p | \Gamma_i \rangle = \int \psi_f^* p \psi_i dx, \qquad (2.16)$$

where $\Gamma_{i,f}$ are the symmetry representations of the initial and final state, respectively, $\psi_{i,f}$ are the wave functions for the initial and final state, respectively. Γ_p is the symmetry representation of the operator driving the transition. p is the momentum operator. The selection rules can be generalized by expressing the *direct product* $\Gamma_i \otimes \Gamma_p \otimes \Gamma_f$ as a direct sum of irreducible representations [66]

$$\Gamma_i \otimes \Gamma_p \otimes \Gamma_f = \Gamma_a \oplus \Gamma_b \oplus \Gamma_c \ldots \qquad (2.17)$$

To obtain the irreducible representations of Γ_j's, we first multiply the characters of Γ_i, Γ_p and Γ_f column by column. Then, we find a set of representations which add up to the products. If one of the representations is Γ_1, the totally symmetric representation, the integral may be nonzero and the transition is allowed.

In the relaxation process of LVMs, states can interact via a matrix element $\langle \Gamma_k | \delta H | \Gamma_l \rangle$, where δH is a perturbation due to the surrounding atoms and has symmetry Γ_1. The direct product is given by

$$\Gamma_k \otimes \Gamma_1 \otimes \Gamma_l = \Gamma_k \otimes \Gamma_l. \qquad (2.18)$$

States only interact if they have the same symmetry component. For example, Hsu *et al* [68] discussed the interaction between the antisymmetric stretch mode and the

resonant mode of oxygen in Si. The intersititial oxygen in Si belongs to D_{3d} point group. Table 2.1 lists the character table for this defect. The stretch mode and the resonant mode have A_{2u} and E_g symmetries, respectively. They cannot interact with each other because they do not have the same symmetry. From Table 2.1, we know the second harmonics ($n = 2$) of the resonant mode ($E_g \otimes E_g$) have A_{1g}, A_{2g} and E_g symmetries, none of which can interact with the stretch mode (A_{2u}). However, the combination of an E_g and E_u mode is represented by $E_g \otimes E_u = A_{1u} \oplus A_{2u} \oplus E_u$, which contains an A_{2u} component. So the stretch mode (A_{2u}) can interact with the combination mode of E_g and E_u modes.

D_{3d}	E	$2C_3$	$3C_2$	i	$2S_6$	$3\sigma_d$
A_{1g}	1	1	1	1	1	1
A_{2g}	1	1	-1	1	1	-1
E_g	2	-1	0	2	-1	0)
A_{1u}	1	1	1	-1	-1	-1
A_{2u}	1	1	-1	-1	-1	1
E_u	2	-1	0	-2	1	0
$E_g \otimes E_g$	4	1	0	4	1	0
$A_{1g} \oplus A_{2g} \oplus E_g$	4	1	0	4	1	0
$E_g \otimes E_u$	4	1	0	-4	-1	0
$A_{1u} \oplus A_{2u} \oplus E_u$	4	1	0	-4	-1	0

Table 2.1: One example showing the symmetry of the combination modes by using the direct product and sum.

If the accepting modes are propagating phonons in a perfect crystal, they have translation symmetry. Space groups must be considered [65]. Calculating the symmetry of phonon combinations is complicated because the phonons can occur at different symmetry points, and thus have different symmetry point groups. For example, the interstitial oxygen defect has the same symmetry as the L-point, which has D_{3d}

symmetry. One of the allowed phonon decay channels is $TO(L) + TA(L) + TO(X)$. Two of the phonons are at the L-point, but one is at the X-point, and therefore has different symmetry. In general, the symmetry of a three-phonon combination mode consisting of phonons with wave vectors $*\vec{k_1}$, $*\vec{k_2}$ and $*\vec{k_3}$ is the direct product of their irreducible representations:

$$*\vec{k_1} \otimes *\vec{k_2} \otimes *\vec{k_3}. \tag{2.19}$$

The reduction of the direct product of different irreducible representations of the space group into a direct sum of space group irreducible representations is thus the central problem. The coefficients of the irreducible representations in the direct sum have been calculated and tabulated by Birman [69]. One uses the point group of the highest symmetry point since all of the other point groups will be its subgroups. The O_h group is the point group for the Γ point in the diamond crystal structure. For the decay of a LVM with infrared activity, the direct sum of the combibation of accepting modes must contain the $\Gamma^{(15-)}$ irreducible representation in the O_h point group. $\Gamma^{(15-)}$ is the representation of the symmetry of the infrared dipole operator in diamond structure. It is irreducible in O_h point group, but can be reduced to $A_{2u} \oplus E_g$ in D_{3d} point group since D_{3d} at L-point is the subgroup of O_h group at Γ point in the diamond structure. $\Gamma^{(15-)}$ and A_{2u} are expressed by different notations. A_{2u} and E_g notations are often used in molecular physics. Γ plus a superscript i to lable these irreducible representations is common in solid state physics.

Two- and three-phonon decay channels and their activities were also calculated by

Critical Point	Phonon	Symmetry	Critical Point	Phonon	Symmetry
Γ	$O(\Gamma)$	$\Gamma^{(25+)}$	L	$TO(L)$	$L^{(3-)}$
X	$TO(X)$	$X^{(4)}$		$LO(L)$	$L^{(1+)}$
	$L(X)$	$X^{(1)}$		$LA(L)$	$L^{(2-)}$
	$TA(X)$	$X^{(3)}$		$TA(L)$	$L^{(3+)}$

Table 2.2: High symmetry points, phonons and irreducible representation in diamond structure.

Birman [70], but an example is included here to apply this principle to the analysis of the symmetry of multiphonon decay channels. The critical symmetry points, the phonons at those points and their irreducible representations are listed in Table 2.2. Let us consider the symmetry and activity of the phonon combination $TO(L)$ + $TO(X) + TA(L)$, which is one of the decay channels of the interstitial oxygen stretch mode in Si. The calculation of the direct sum is as follows:

$$TO(L) + TA(L) + TO(X) \rightarrow L^{(3-)} \otimes L^{(3+)} \otimes X^{(4)}$$

$$= (\Gamma^{(2-)} \oplus \Gamma^{(12-)} \oplus 2(\Gamma^{(25-)} \oplus X^{(1)} \oplus X^{(2)} \oplus X^{(3)} \oplus X^{(4)})) \otimes X^{(4)}$$

$$= 12(X^{(1)} \oplus X^{(2)} \oplus X^{(3)}) \oplus 11X^{(4)} \oplus 2(\Gamma^{(1+)} \oplus \Gamma^{(1-)} \oplus \Gamma^{(2+)} \oplus \Gamma^{(2-)})$$

$$\oplus 4(\Gamma^{(12+)} \oplus \Gamma^{(12-)}) \oplus 6(\Gamma^{(15+)} \oplus \Gamma^{(15-)} \oplus \Gamma^{(25+)} \oplus \Gamma^{(25-)}) \qquad (2.20)$$

The above three-phonon combination contains $\Gamma^{(15-)}$ with a multiplicity or activity of 6. So it is an allowed decay channel for interstitial oxygen in Si. The detailed theory is given in Ref. [70].

The level of theoretical investigation of the lifetime of local vibrational modes is less advanced. To our knowledge, first-principle calculations of vibrational lifetimes of

point defects in crystalline semiconductors are not available until now. The theoretical considerations presented in this chapter are used as a framework for discussing the vibrational lifetimes of local vibrational modes in semiconductors.

Chapter 3

Experimental Details

In this chapter, the techniques involved in performing these experiments are described in detail. We begin with a discussion of Fourier transform infrared (FTIR) spectroscopy, followed by a description of the use of the Jefferson Lab Free Electron Laser and optical parametric amplifier. We also discuss the vibrational pump-probe spectroscopy in detail in this chapter. A description of sample preparation for each experiment concludes this chapter.

3.1 Fourier Transform Infrared Spectroscopy

Local vibrational modes of an impurity can be excited by infrared light of the proper frequency. In infrared absorption spectroscopy (IRAS) one measures the attenuation of the beam intensity as a function of frequency caused by the penetration of infrared light through a particular sample. The use of FTIR spectrometer allows high resolution IRAS measurements.

Figure 3.1 shows the schematic diagram of a FTIR spectrometer. The main com-

33
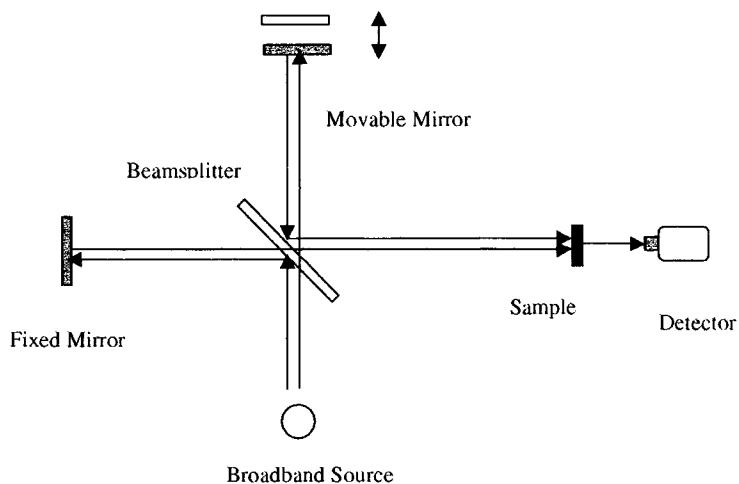
Figure 3.1: Sketch of a FTIR spectrometer. It consists of a light source, a fixed mirror, a movable mirror, a beam splitter and a detector.

ponent of a FTIR spectrometer is a Michelson interferometer. The interferometer consists of a beam splitter, a fixed mirror and a movable mirror. Collimated light is directed to a semitransparent beam splitter, which is designed to transmit half of the light to the movable mirror and half of the light to the fixed mirror. The two beams will reflect off their respective mirrors and recombine at the beam splitter. One beam will travel through the sample, where light is absorbed because of electronic or vibrational excitations. Finally they enter a detector, where the intensity integrated over all frequencies is measured.

The beam splitter splits the beam into two parts of electromagnetic waves moving towards the detector, which have equal electric field amplitudes $E_0(\sigma)$ for a given wave number σ. The electric field at the detector is the sum of the electric fields of

the two waves:

$$E(\sigma) = E_0(\sigma)\{e^{i[wt-2\pi\sigma z_1]} + e^{i[wt-2\pi\sigma z_2]}\}, \tag{3.1}$$

where z_1 and z_2 are the optical path lengths from the source to the detector for the waves reflected from the movable and fixed mirror, respectively. The contribution to the light intensity at the detector from waves with a particular wave number σ (in CGS unit)is given by [71]

$$I(\sigma, x) = \frac{c}{8\pi}|E(\sigma)|^2 = \frac{c}{4\pi}E(\sigma)^2\{1 + \cos[2\pi\sigma z]\}, \tag{3.2}$$

where $z = z_1 - z_2$ is the difference in optical path length of the two waves. When the movable mirror and fixed mirror are at the same distance from the beam splitter, this condition is called *zero path difference*. The detector measures the maximum intensity at this position of the movable mirror. A plot of light intensity versus z is called *interferogram*. When a broadband infrared source with many wavelengths is used, the total interferogram measured by the detector is proportional to the intensity given in Eq. (3.2) integrated over all wave numbers:

$$I(x) = \int_0^\infty I(\sigma, x)dx = \frac{I(0)}{2} + C\int_0^\infty \frac{c}{4\pi}E_0{}^2(\sigma)\cos[2\pi\sigma z]d\sigma, \tag{3.3}$$

where C is a constant, which depends on the design of the detector. The first term in Eq. (3.3) is a constant representing the total energy in the spectrum. This constant is subtracted from the interferogram before the Fourier transform is performed. The

spectrum, $B(\sigma)$ can be obtained by calculating the inverse cosine Fourier transform of the interferogram:

$$B(\sigma) = \frac{c}{8\pi}E_0{}^2(\sigma) = \frac{2}{C}\int_0^\infty [I(\delta) - I(0)/2]\cos[2\pi\sigma z]dz. \tag{3.4}$$

The limits of this integral should extend from 0 to plus infinity. In reality, the movable mirror has finite moving range (0 to L). The interferogram is therefore truncated at some maximum path difference z_{max}. This truncation function is often called a boxcar truncation function.
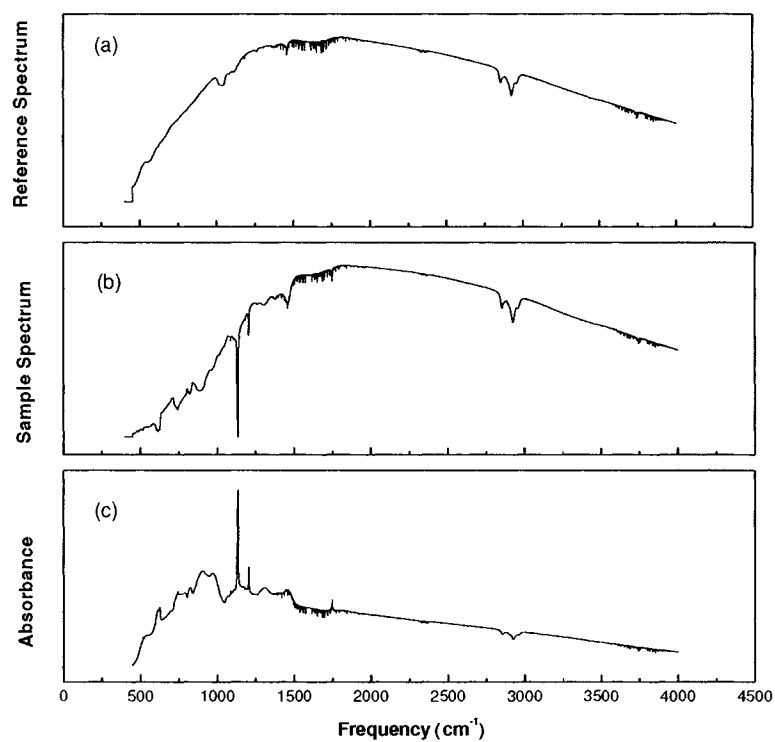
Figure 3.2: An illustration of obtaining a sample absorbance spectrum from an interferogram: (a) reference spectrum, (b) sample spectrum, (c) absorbance spectrum.

In a FTIR experiment a background spectrum must be measured as a reference. As shown in Figure 3.2 (a), the background spectrum contains contribution from the instrument and the environment. Next, an interferogram is measured with a sample containing defects and a raw spectrum is produced as shown in Figure 3.2 (b). It looks similar to the background spectrum except that additional dips are superimposed upon the background spectrum. The line observed around 1136 cm^{-1} corresponds to interstitial oxygen in Si, which will be discussed in detail in chapter 6. To reduce the atmospheric contributions to the spectrum, the raw spectrum must be divided by the background spectrum (See Figure 3.2 (c)). This will produce an absorbance spectrum. We use FTIR spectroscopy to check the absorption line before the lifetime measurement by the pump-probe experiment. This ensures that enough defects are present in the sample. FTIR spectroscopy is also used to measure the natural linewidth of local vibrational modes.

3.2 Generation of Picosecond Mid-Infrared Pulses

3.2.1 Introduction

Time-resolved spectroscopy of vibrational transitions requires ultrashort pulses that are tunable in the mid-infrared region of the electromagnetic spectrum. The pulses have to be intense since local vibrational mode transitions are hard to saturate due to their small absorption cross sections. The dynamics of vibrational transitions occurs

on a picosecond time scale, which requires ultrafast laser pulses.

Continuously tunable pulses in the mid-infrared can be generated by different lasers and techniques, such as free-electron lasers [41, 42], color-center lasers, difference-frequency mixing [72, 73], and optical parametric generation and amplification. The light sources used in this dissertation are the Free Electron Laser at Thomas Jefferson National Accelerator Facility (TJNAF) and an optical parametric amplifier (OPA). FELs do not use atoms or molecules as an active medium, but rather "free" electrons in a specially designed magnetic field. A brief description of the use of the FEL at Jeffeson Lab will be presented in the Section 2.2.3.

3.2.2 Optical Parametric Amplifier

Due to their availabilities, optical parametric devices comprise the vast majority of IR sources. OPA is based on a nonlinear interaction in which two light waves of frequencies ω_1 and ω_2 are amplified in a medium which is irradiated with an intense pump wave of frequency $\omega_3 = \omega_1 + \omega_2$. The higher of the two frequencies ω_1, ω_2 is referred to as the signal, the lower as the idler. For the parametric amplification to occur efficiently, the phase-matching condition $k_3 = k_1 + k_2$ must be satisfied, where k_3, k_1 and k_2 are wave vectors of pump beam, signal and idler, respectively. This is generally achieved by using birefringent nonlinear crystals such as β-BaB_2O_4 (BBO) and $KTiOPO_4$ (KTP). By changing the angle of the optical axis of the crystal with respect to the polarization of one or two of the three interacting fields, a particular

set of frequencies ω_1, ω_2 is selected for which both the conditions of phase matching $(n_3\omega_3 = n_1\omega_1 + n_2\omega_2)$ and energy conservation $(\omega_3 = \omega_1 + \omega_2)$ are fulfilled (n_j is the index of refraction of the medium at frequency ω_j). Figure 3.3 is an illustration of this process.

Nonlinear Crystal
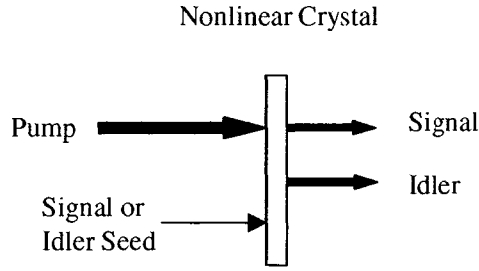
Figure 3.3: Sketch of optical parametric generation.

OPA is a second-order nonlinear optical process. In general, the dielectric polarization $P(t)$ of a medium with nonlinear susceptibility χ can be written as as expansion in powers of the applied field

$$P(t) = \varepsilon_0(\chi^{(1)}E(t) + \chi^{(2)}E^2(t) + \chi^{(3)}E^3(t) + \ldots), \tag{3.5}$$

where $\chi^{(k)}$ is the kth-order susceptibility tensor of rank $k+1$. The electromagnetic wave

$$E(t) = E_1\cos(\omega_1 - k_1 z) + E_2\cos(\omega_2 - k_2 z), \tag{3.6}$$

consists of two components incident on the nonlinear medium. At a fixed position (z=0) the quadratic term $\chi^{(2)}E(t)$ in Eq. (3.5) gives the second-order polarization

$$\begin{aligned}
\widetilde{P}^{(2)} &= \varepsilon_0 \chi^{(2)} E^2 (z = 0) \\
&= \varepsilon_0 \chi^{(2)} (E_1^2 \cos^2 \omega_1 t + E_2^2 \cos^2 \omega_2 t + 2 E_1 E_2 \cos \omega_1 t \cdot \cos \omega_2 t) \\
&= \varepsilon_0 \chi^{(2)} \{ \frac{1}{2} (E_1^2 + E_2^2 + \frac{1}{2} E_1^2 \cos 2\omega_1 t \\
&= \frac{1}{2} E_2^2 \cos 2\omega_2 t + E_1 E_2 [\cos(\omega_1 + \omega_2)t + \cos(\omega_1 - \omega_2)t] \},
\end{aligned}$$
(3.7)

which includes a dc polarization, ac components at the second harmonics $2\omega_1$, $2\omega_2$ and components at the sum or difference frequencies $\omega_1 \pm \omega_2$.

The phase condition can be fulfilled in uniaxial birefringent crystals that have two different indices n_o and n_e for the ordinary and the extraordinary waves. The BBO crystal is a good choice due to its high damage threshold [74] and large bandwidth. BBO crystals are therefore often used in commercial OPA systems. If the OPA is pumped with the fundamental Ti:sapphire wavelength at 800 nm, signal and idler cover a wavelength range of 1-2.6 μm. Longer wavelengths cannot be generated because of the onset of infrared absorption in BBO at $\sim$ 2.6μm [74]. The tuning range can be extended to 20 μm by difference frequency mixing of the signal and idler in a different crystal e.g., AgGaS$_2$ or GaSe, but the resulting intensities are rather low.

In our OPA system depicted in Figure 3.4, a tunable mode-locked Ti:sapphire oscillator (Coherent Mira Model 900-F) is used to generate pulses of 200 fs at a repetition rate of 76 MHz, with a center wavelength of 800 nm. The oscillator is

200 fs, 800 nm
~10 nJ at 76 MHz

Coherent Mira
900-F

Coherent Verdi
5 V pump laser

Quantronic DQ-527
flash lamp pumped

Quantronic Titan
RGA and MPA amplifiers

2.5 ps, 800 nm
2.5 mJ at 1 kHz

Light Conversion TOPAS
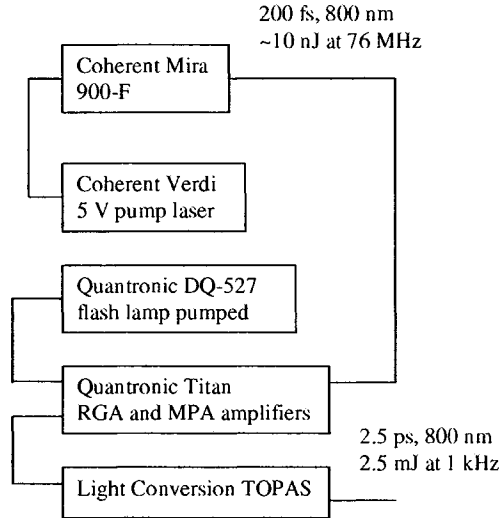
Figure 3.4: The amplified Ti:sapphire laser system consists of an oscillator Mira 900-F, diode-pumped laser Verdi 5V, frequency-doubled Nd:YLF laser DQ527 and TOPAS.

pumped by a Coherent Verdi V-5 Diode-Pumped laser, which has an output power of 5W. The oscillator output pulses are first stretched to a length of several hundreds of picoseconds (ps) by using a single grating. The pulses from the stretcher are used to seed a Quantronix Titan regenerative Ti:sapphire amplifier (RGA), which is pumped by 15% of the beam from a Quantronix DQ527 Nd:YLF laser. The DQ527 Q-switched laser uses a flash lamp to pump the Nd-doped $LiYF_4$ crystal to generate 20-mJ pulses at a wavelength of 527 nm. The seed pulse is coupled into and out of the RGA at a frequency of 1 KHz using a Pockel's cell. A photodiode monitoring the output pulses from the RGA is used together with a frequency divider to trigger the Pockel's cell and the Q-switched DQ527, ensuring that they are synchronized with the seed pulses. The output from the RGA are amplified by a two-pass amplifier,

which is pumped by 85% of the beam from the DQ527. The amplified pulses will be compressed by a pair of gratings. Pulses of 2.5 ps and 2.5 mJ at a repetition rate of 1 KHz are obtained. A typical autocorrelation trace of amplified pulses are shown in Figure 3.5. The pulses from Titan will be used as pump source for the OPA.

Slow-Scan Autocorrelation Trace
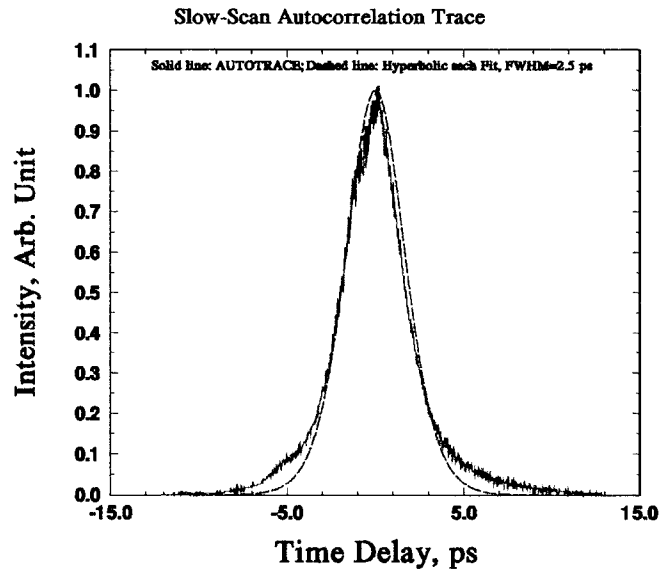
Figure 3.5: Autocorrelation trace of the compressed amplifier output, recorded from a BBO crystal. The solid curve is a sech^2 with a FWHM of 2.5 ps.

The OPA used for lifetime measurements is a commercial traveling-wave optical parametric amplifier of superflurorescence (TOPAS), which can generate signal and idler pulses that are continually tunable from 1 to 2.6 μm. It is based on the one stage for generation of superflurorescence (SFL) and four light amplification stages arranged in the same 5 mm BBO crystal.

The TOPAS is depicted schematically in Figure 3.6. The 800 nm pump beam

Figure 3.6: The traveling-wave optical parametric amplifier TOPAS, the 800 nm pump beam is shown in grey, the signal+idler beam in black. All mirrors are 800 nm high-reflective dielectric mirrors, except M3, M7 and M8 which are metallic mirrors. NC: nonlinear crystal (BBO); TD: birefringent plate to generate delay between signal and idler; GP: glass plate; BS1 and BS2: beamsplitters.

is split into three parts by the beam splitters BS1 and BS2. The first two are used for the fourth and fifth amplification stage. The third one (only 4%) passes through a telescope and is directed to the BBO crystal by the mirrors M1 and M2. There, parametric generation takes place, resulting in a broadband seed pulse. The seed is backward reflected from CM1, through the BBO crystal (NC), to CM2. This is the second pass, which amplifies the collinear component of SFL produced in the first pass. The third pass is the reflection from CM2 through NC to the diffraction grating (DG). In the third pass the beam of amplified SFL goes just above CM1 and hits the center of DG. The beam from DG is relatively weak and broad-band parametric radiation with significant divergence in vertical plane. The beam will be amplified

by the first part of the pump beam, which is directed to the BBO by mirrors M3-5.
It passes through a glass plate GP which compensates the parallel displacement of
the seed when the phase angle of the BBO is changed. The pre-amplified beam goes
through M2 and is reflected from M7 and passes the time delay crystal that separates
signal and idler pulses in time. Then it will be directed to NC by mirrors M8. There
it is strongly amplified by the third and most intense part of the pump beam, directed
to the crystal by mirrors M9-11.

The TOPAS performance is critically dependent on the pump beam parameters,
such as energy, pulse duration, contrast ratio and beam quality to achieve the specified
values. The beam energy from Titan should be over 2.2 mJ. The power from Titan
can be optimized by aligning the pump mirrors of the RGA and multipass amplifier.
The contrast ratio measured by a fast photodiode should be > 100. If the contrast
ratio is less than 100, it can be optimized by turning the screws the of Pockel's cell
slightly. If all these parameters are close to the specification of Titan, the daily
operation of the TOPAS is very easy.

The first step to align the TOPAS is to ensure that the beam goes through the
center of the first two irises. Then block the 4th and fifth path by placing a beam
blocker before M3 and M9. Second, place a card before CM1 and check that the
beams after the first and third passes are in one vertical plane. By scanning in height
of the card, one can see the first and third pass alternatively. By using a small card
before grating (DG) and aligning the pick-up mirror outside of TOPAS, the third
path can be aligned through the center of CL2. Third, one can now unblock the

4th and 5th pass and put a power meter after the TOPAS to observe the output. If the power is too low, then the SFL generated in the third pass is most likely too weak. One reason is that the pulse duration is slightly different from previous setting. The angle of stretcher grating can be tweaked slightly to optimize the dispersion of stretcher in Titan according to the reading of the power meter.
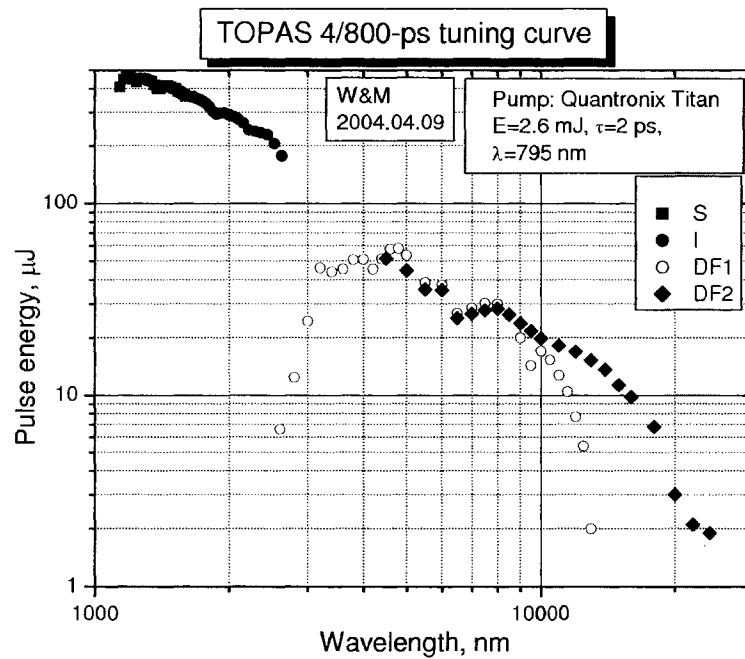
Figure 3.7: Tuning curves of the TOPAS at the College of William and Mary. S: Signal; I: Idler; DF1: Difference Crystal AgGaS$_2$; DF2: Difference Crystal GaSe.

Very high conversion efficiencies can be reached with the TOPAS. Signal+idler energies of 650 μJ can be obtained with pump energy of 2.3 mJ. To extend the tuning range to infrared wavelengths, a difference frequency generator is used to mix the TOPAS signal and idler pulses. Nonlinear crystals for frequency mixing are installed

in computer controlled rotation stage that can be controlled by TOPAS module. Two different nonlinear crystals are used for the difference frequency generation. The wavelength range can be obtained from 2.6-13 μm for $AgGaS_2$ and 4.5-22 μm for GaSe crystal. The tuning curves are shown in Figure 3.7. More details are given in the TOPAS manual (TOPAS manual, Light Conversion).

3.2.3 Free Electron Laser

Overview
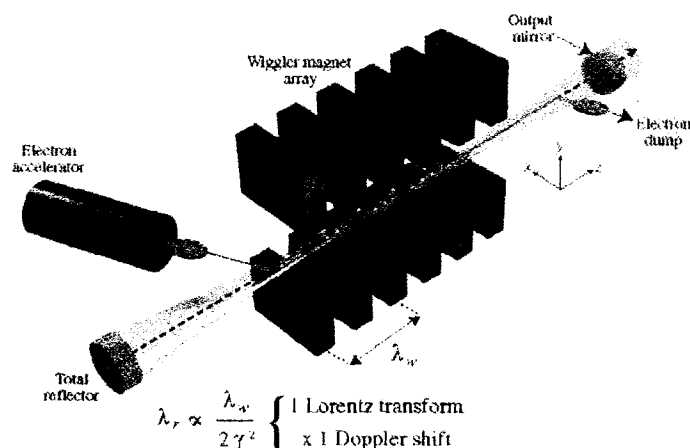
Figure 3.8: Schematic diagram of a free electron laser [75].

A free-electron Laser (FEL) provides intense, powerful beams of laser light that can be tuned to a precise wavelength. FELs differ from most other types of lasers by not having atoms or molecules as an active medium, but rather "free" electrons in a specially designed wiggler. They can absorb and release energy at any wavelength. This key feature enables the FEL to produce intense powerful light over a large

wavelength range. The lack of a lasing medium in the cavity allows the laser to operate at very high power levels without the usual cavity heating problems.

The key components of an FEL oscillator include an electron beam of given energy and intensity and the associated accelerator, a wiggler (also called an undulator), and the electromagnetic (EM) wave and the associated optical components. Figure 3.8 [75] is a schematic representation of an FEL. The principles behind free electron lasers are not discussed here. A detailed description of FEL physics is given in Ref. [76]. Briefly, the electrons are accelerated to the velocity close to light velocity by a superconducting RF linac. The relativistic electron beam oscillates within a cavity with a magnetic field, which is controlled by a linear arrangement of magnets of alternating polarity. Kinetic energy from the electron beam is transfered to EM waves within the cavity, allowing for regenerative energy build-up in the cavity. When the electron beam is accelerated and confined to bunches, the FEL cavity can be synchronously pumped, generating sub-picosecond IR pulses.

The radiation produced by an FEL has a wavelength given by

$$\lambda = \frac{\lambda_w}{2\gamma^2}(1 + a_w^2),\tag{3.8}$$

where λ_w is the wiggler period, and γ is the relativistic Lorentz factor, and a_w is a characteristic of the wiggler. Unlike most conventional solid state or gas lasers, which produce radiation at specific frequencies corresponding to transitions in a gain medium, the FEL wavelength can be quickly and continually tuned merely by vary-

ing the electron beam energy. This wavelength tunability is one of the most useful features of the FEL. A review comparing and contrasting the uses of FEL and optical parametric sources for the study of vibrational dynamics has been presented in Ref. [77].

Characteristics of the IR-Demo FEL at Jefferson Lab

The Jefferson Lab FEL facility is designed to delivery the optical beam to several user stations. The optical beam is transported to each experimental room via an evacuated beam line. A small fraction of the beam is delivered to a diagnostics table where the beam is continuously characterized. These diagnostics consist of macropulse power measurements, spectral wavelength measurements of FEL beam using a monochromator, and the temporal pulse length measurements using an autocorrelator. Table 3.1 summarizes some of the important characteristics of the FEL IR-Demo at Jefferson Lab.

The average power used in our experiments described in Chapter 4 is around 20 W, with a repetition rate of 18.7 MHz. The beam delivers pulses with a duration of $\sim$ 1 ps at 5 μm. The beam size is $\sim$ 2.5 cm in diameter at 5 μm when it is transported to the lab. A telescope has to be used to reduce the beam size.

In order to work in a safe environment, the labs at Jefferson Lab FEL have three different modes of operation. Before running the full power beam, the beam is aligned in a so-called "alignment mode". The laser provides less than 400 mJ of light to the user lab in 2 Hz pulse operation. Users have to wear goggles all time while working in the lab. After the laser is aligned, the laser can be operated in the full power mode.

Basic Characteristics	
Wavelength range	3 - 6.2 μm
Bandwidth (FWHM)	0.3-2%
Pulse length (FWHM)	0.5-1.7 ps
Transverse mode	<2x diffraction limit
Beam diameter at lab	1.5-3.5 cm

Pulse Structure, Energy, and Power	
Repetition Rate	74.85, 37.425, 18.7 MHz
Micropulse energy	up to 70 μJ
Average power	1720 watts

Electron Beam Characteristics	
Electron Energy	42 Mev
Average current	5 mA
Peak Current	50 A

Stability	
Wavelength Stability	< 2 cm^{-1}
Amplitude jitter (RMS)	< 10% p-p
Energy stability (RMS)	4×10^{-4}
Beam position jitter (RMS)	100 μm
Beam Angle jitter (RMS)	250 μrad

Table 3.1: Specification of the FEL IR-Demo at the Jefferson Lab.

An interlocked hutch ensures that users are not exposed to the FEL beam while it is being delivered to the room. This is called "hutch mode". When the interlocked hutch is open and the full power beam is delivered to the experimental table, users are not allowed in the lab during beam delivery. This is called exclusionary mode. All the data acquisition is accomplished by a remote computer in the control room. If the user needs to go to the lab to adjust some optics, the FEL beam has to be shut off by the operator.

3.3   Vibrational Pump-probe Spectroscopy

3.3.1   Experimental Set-up

The vibrational lifetimes in this thesis were measured by pump-probe spectroscopy, also called transient bleaching spectroscopy. The experimental setup is a standard one-color pump-probe set-up which is shown in Figure 3.9. The laser beam of the TOPAS or FEL must be collimated at different wavelengths by a pair of lenses or curved mirrors. The collimated laser beam is split into two beams by a ZnSe beam splitter. One is pump beam, which carries about 90% of the total energy. The other is probe beam, which is much weaker than the pump beam (about 10%). The probe beam will pass through a computer-controlled translation stage. Both pump and probe beams are focused by a pair of parabolic mirrors. The pump and probe are spatially overlapped in the sample. The strong pump beam will excite a significant fraction of the defects to the first excited state, which will cause a transient increase in the transmission coefficient of the sample. By varying the delay between the pump and probe pulses, the evolution of the excitation can be followed in time. The transmitted probe beam is measured by a detector placed after a monochromator. In order to measure the decay time of the first excited vibrational state of the defect, the laser pulse must be significantly shorter than the decay time. The pump beam is chopped at 300 Hz for the OPA system and 3 KHz for the FEL beam. The chopped beam causes a modulation of the pump-probe signal, which is recorded by a lock-in amplifier. In the experiments we use MCT/InSb "sandwich" detectors from Judson

Technologies, LLC. The InSb and MCT detectors can be used at wavelengths at 2 to 6 μm and 6 to 16 μm, respectively. The detected signal is first amplified by a low-noise voltage preamplifier. A SR250 gated integrator and boxcar averager, and a lock-in amplifier are used to average and extract the transient change of the transmitted signal of the probe beam.
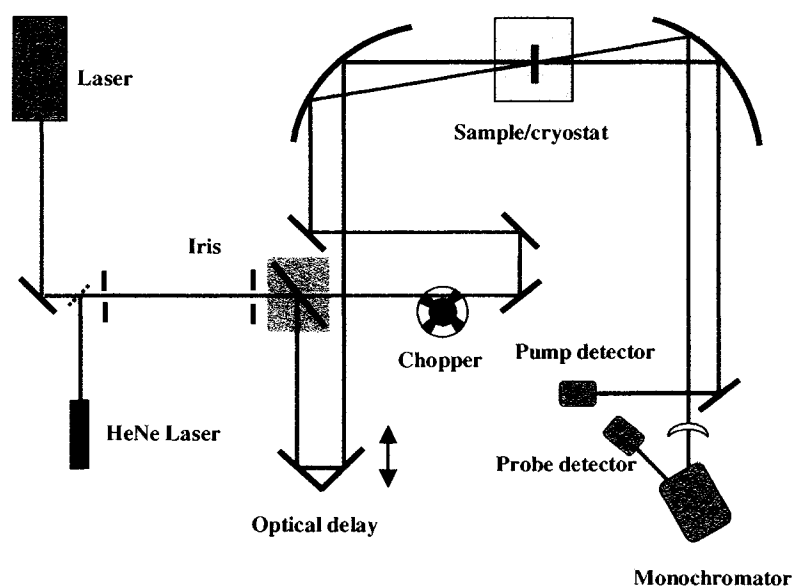
Figure 3.9: Typical set-up for pump-probe experiments.

3.3.2 Alignment of the Infrared Beams

The alignment of the invisible beam is the most immediate challenge to performing any experiment with the IR beam. Basic alignment tasks, trivially performed with a visible laser, become difficult and time-consuming with the infrared beam. It is therefore important to develop alignment methods which are quick and accurate so

that beam alignment can be accomplished efficiently. The most generally useful technique is to coalign a visible beam with the infrared beam to provide a visual reference to guide the alignment of the IR beam. Red Helium-Neon (HeNe) lasers are generally the visible laser of choice, because of their simple operation and excellent transverse mode quality.

In the experimental set-up shown in Figure 3.9, two irises are placed before the beam splitter. During the alignment procedure, the IR laser beam is blocked and the HeNe laser beam is directed into the center of the two irises by a pick-up mirror. The pick-up mirror is mounted on a magnetic base and can be easily removed and placed back. All the optics after the second iris are aligned according to the HeNe laser beam. After all the alignments are finished, one needs to block the HeNe beam, remove the pick-up mirror and let the IR beam go through the two irises. A detector is placed after the irises and the power is optimized when the beam goes through the irises. This ensures that the IR beam passes through the center of both irises.

3.3.3 Experimental Procedures

The vibrational lifetime measurements of local vibrational modes are very challenging due to the small absorption cross section of the defects, especially when they are measured by our OPA system. The measurement is very critically dependent on the alignment and laser stability. Before running the experiment, we must make sure that the lasers run stable and make sure that the laser beam goes through the center of

the first two irises. Generally there are three steps in the experiment. First, we use a reference sample, which gives rise to a strong signal, to check the alignment and the spatial overlap of the pump and probe beam. A pin-hole with a diameter of 50 μm is used to help align the spatial overlap of the two beams. The sample is mounted on a three-dimensional translation stage, which can be moved to optimize the signal. Once the set-up is optimized, a big spike shown in Figure 3.10 can be observed. This spike is independent of wavelength. Next, the sample is mounted in the cryostat and one needs to check whether the spike still exists. Then, the sample is cooled down to 80 K and the OPA is tuned to the absorption resonance of the defect. When the spectrum of the probe beam is measured with the monochromator, an absorption dip will be observed, which is shown in Figure 3.11. This spectrum is measured in a Ge sample with a very high oxygen concentration. The dip corresponds to the absorption of the oxygen stretch mode in Ge. Most defects do not have a strong dip due to their weak absorption. The last step is to lower the temperature to 10 K and measure the vibrational lifetime.

3.4 Sample Preparations

3.4.1 Hydrogen in Silicon

Hydrogentated Si prepared by proton-implantation

The proton-implanted Si samples used in vibrational lifetime measurements are
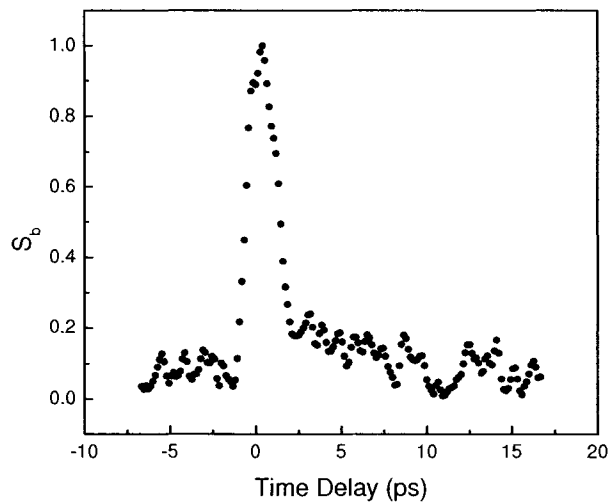
Figure 3.10: Pump-probe signal at room temperature from a Ge sample.
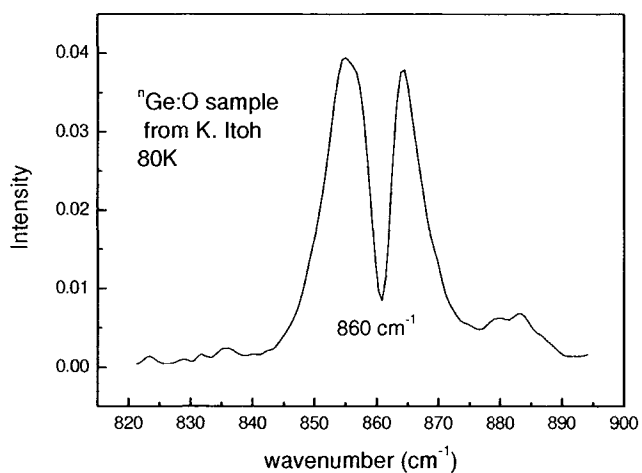
Figure 3.11: Spectrum of a 1.7 ps laser pulse passing through a monochromator. The dip at 860 cm^{-1} corresponds to the absorption of interstitial oxygen in Ge doped by $C_O = \sim 10^{18}$ cm^{-3}.

made by M. Budde [78]. It is a 2-mm thick, high resistivity, disk-shaped Si single crystal, coated with a mid-IR antireflection coating on one side. The coating prevents spurious signals due to internally reflected light. The Si sample is implanted with protons at different energies in the range 1-1.8MeV. A total dose of 2×10^{17} protons/cm^2 is implanted into the uncoated side of the sample at 80 K yielding a 47 μm deep, uniform H concentration profile. Figure 3.12 shows the implantation profile obtained by the software package SRIM [79]. The implantation dose at each energy is adjusted in order to obtain a uniform hydrogen concentration of 0.02%. The sample temperature is kept at 80 K during the implantation, and the background pressure is about 10^{-6} torr. A uniform H concentration of 1.7×10^2 ppm is formed from the surface to a depth of 47 μm by variable-energy implantation of the uncoated side of the sample at 80 K.
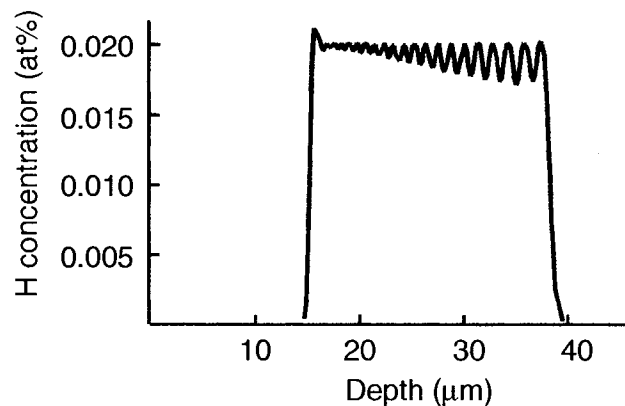
Figure 3.12: Hydrogen implantation profile.

Hydrogentated Si prepared by electron-irradation

The samples which are used in high resolution IRAS measurements are prepared by electron irradiation at Lehigh University. An advantage of producing these defects by electron irradiation, rather than by proton implantation, is that the defects can be distributed uniformly with lower concentrations throughout bulk samples and, therefore, have reduced inhomogeneous broadening and have narrower vibrational linewidths. The samples consist of n-type Si ($[As]=3 \times 10^{14}$ cm^{-3}) grown by the floating zone (FZ) method. The samples have dimensions $7 \times 7 \times 15$ mm^3 with the optical viewing direction along the long axis. The viewing surfaces of the samples are polished with SiC and Al_2O_3 grits and 0.5 μm diamond paste. The samples doped with H (Si:H) or D (Si:D) are annealed at 1250° for 30 min in quartz ampules containing H_2 or D_2 gas at 0.66 atm. The anneals were terminated by a rapid quench in water to room temperature. The concentration of H or D is determined to be 10^{16} cm^{-3} by measuring the intensity of the 3618.4 cm^{-1} line assigned to H_2. The H and D defects are created by irradiating the samples with 2.5 MeV electrons at RT to a total dose of 10^{17} cm^{-2}. The samples are irradiated with half the total dose from opposite sides to make the defect concentration nearly uniform. The defect concentration in the samples is estimated to be $\sim 10^{16}$ cm^{-3}, which is $\sim$50 times smaller than in the proton implanted samples.

3.4.2 Oxygen in Si and Ge

The oxygen isotopes ^{17}O and ^{18}O are diffused into FZ-Si doped with boron concentration of 5.7×10^{15} cm^{-3} at the University of Paderborn [80]. In order to avoid contamination with transition metals such as Fe or Ti, the diffusion was done under extremely clean conditions using an IR heat chamber. The sample is placed into an O_2-gas atmosphere enriched with ^{17}O and ^{18}O in a cooled quartz ampoule onto a short quartz rod. The sample is held for about 14 days at an oxygen pressure of 3 bars at 1400°C. The temperature gradient is within 5% over 50 mm of the sample length. The hottest point in the ampoule and support system could be held below 900°C by forced air cooling, thus over 500°C less than the sample temperature. The sample is cooled slowly from 1400°C to 800°C at a rate of 200°C/hour and then quenched at room temperature.

The $^nGe:O$ sample is an as-grown sample taken from a CZ Ge:O n-type ($n \sim 1.6 \times 10^{14}$ cm^{-1}) crystal grown by Métallurgie Hoboken Overlept in Belgium about 20 years ago.

Chapter 4

Hydrogen Bending Modes in

Semiconductors

4.1 Introduction

Hydrogen passivation of defects is a standard processing step in the production of metal-oxide-semiconductor (MOS) electronic devices. This process reduces the density of P_b centers, the most abundant electrically active defect at the Si/SiO_2 interface, by 3 orders of magnitude [12, 81]. Recently, an isotope effect of Si-H and Si-D bonds has been observed during this passivation process. By using deuterium instead of hydrogen to passivate Si dangling bonds of P_b centers at the Si/SiO_2 interface, Lyding, Hess, and Kizilyalli found that hot-electron degradation of MOS transistors was reduced by factors of 10-50 [82]. This reduction increased the operational lifetime of a silicon chip. A similar isotope effect has been observed in a study of the dissociation kinetics of Si-H and Si-D complexes in GaAs. Chevallier *et al.* observed that, for a given incident ultraviolet (UV) photon density, the concentration of dissociated Si-D

58

complexes is 10-20 times below the concentration of dissociated Si-H complexes [83].
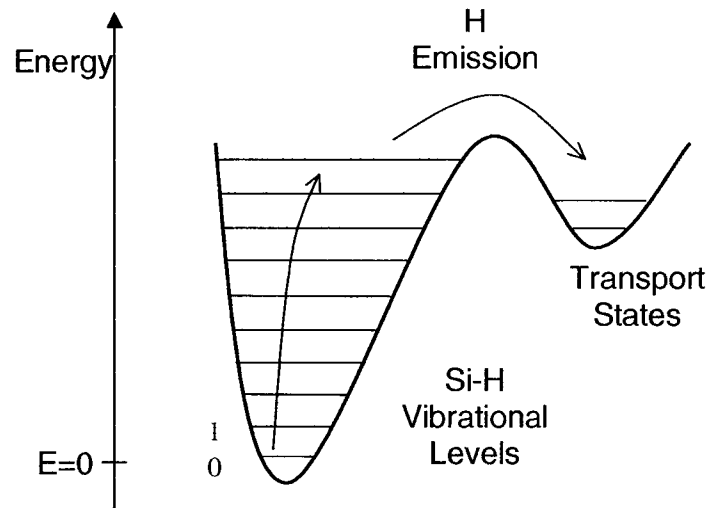
Figure 4.1: Schematic potential energy surface for a Si-H bending mode, showing vibrational energy levels in the first energy well. When H is vibrationally excited to the top of the well, it may be emitted to transporting states and dissociate the bond.

The isotope effect of H and D implies that Si-D bond-breaking is slower than for Si-H. The origin of this isotope effect is not well established and many possible mechanisms have been proposed [82, 84, 85, 86]. The key feature is that the electronic properties of Si-H and Si-D are identical, and only their vibrational properties are different. It is believed that the dissociation of Si-H and Si-D bonds is caused by inelastic electron scattering, which excites the defect to either a dissociative electronic state or to excited vibrational states. The vibrational excitation mechanism of hydrogen-related modes has been described by the truncated harmonic oscillator model [84, 87, 88, 89], which is shown in Figure 4.1. This model describes the Si-H and Si-D bonds as harmonic oscillators. Si-H bonds can be excited to a more ener-

getic vibrational state by non-radiative electron-hole (e-h) recombination or by hot electrons at Si/SiO_2 interfaces. If the excited Si-H oscillation can be sustained, hydrogen can be emitted over the barrier to a mobile transport state (Figure 4.1), causing the Si-H bond to dissociate. Within this model, the desorption rate is approximately given by

$$R \sim \frac{N_{max} + 1}{T_1} \left(\frac{\Gamma_{exc}}{\Gamma_{exc} + 1/T_1} \right)^{N_{max}+1}, \tag{4.1}$$

where T_1 is the lifetime of the vibrational state $|1\rangle$ and Γ_{exc} is the excitation rate of the transition $|0\rangle \rightarrow |1\rangle$. From Eq. (4.1) the vibrational lifetime T_1 is an important parameter for the dissociation rate of Si-H or Si-D bonds.

Chris G. Van de Walle $et\ al.$ proposed that carrier-enhanced dissociation mechanism is most likely controlled by the Si-H bending mode [90]. Based on their calculations by density functional theory, the bending mode at anti-bonding sites provides a more favorable dissociation path than the Si-H stretch mode [91]. The vibrational frequency of bending mode for Si-H was calculated to be around 650 cm^{-1}, and the estimated frequency for Si-D is around 460 cm^{-1}, which is close to the frequency of bulk TO phonon states at the X point (463 cm^{-1}). So one may expect that the coupling of the Si-D bending mode to the Si bulk phonons results in an efficient channel for de-excitation. Evidence for the coupling between the Si-D bending mode and Si-Si lattice vibrations is found at the Si/SiO_2 interface [92] and in deuterated amorphous silicon [93]. To our knowledge the vibrational lifetimes of Si-H and Si-D bending modes in Si have never been measured and vibrational dynamics of bending modes is

essentially unknown. These experiments are difficult to perform because the bending modes lie close to the phonon bath and the laser pulses are weak in that wavelength range.

This chapter presents the first measurement of H-related bending modes in Si. The lifetime of the H_2^* bending mode in Si at 817 cm^{-1} is measured to be $T_1 = 12.2 \pm 0.8$ ps by transient bleaching spectroscopy. The temperature dependence of the lifetime and calculations of phonon-density of state indicate that the bending mode of H_2^* decays into two phonons (LA + TO phonons at the X point). The vibrational lifetimes of other H-related bending modes are estimated from their infrared absorption linewidths. The different lifetimes of H and D-related bending modes can be described by an energy gap law [93].

4.2 Experimental

The sample consists of a 2-mm thick disk cut from single crystalline high-resistivity Si. The sample was polished on both sides, and coated with a mid-IR antireflection coating on one side to prevent spurious signals arising from multiple internal reflections. A uniform H concentration of 1.7×10^2 ppm was formed from the surface to a depth of 47 μm by variable-energy implantation of the uncoated side of the sample at 80 K. After the implantation, infrared absorption spectroscopy was performed with a commercial Nicolet Nexus 670 FTIR spectrometer at the Applied Research Center of Jefferson Lab. Figure 4.2 shows the spectrum of the bending mode at 817 cm^{-1}.

The inset shows the defect structure: one H close to the bond-center side (BC) and the other near the antibonding (AB) site. The H_2^* in Si gives rise to four absorption lines at 817, 1599, 1838, 2062 cm^{-1}. The 1838- and 2062 -cm^{-1} lines were assigned to the stretch modes at the AB side and the BC site, respectively. The 817-cm^{-1} line corresponds to the bending mode of hydrogen at the AB site. 1599-cm $^{-1}$ line is the overtone of the 817-cm^{-1} mode.
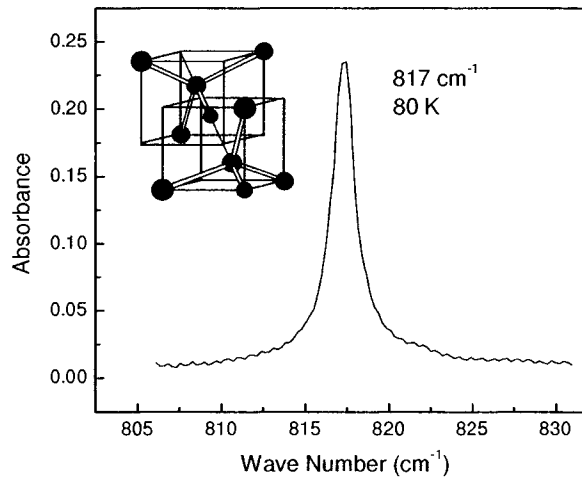
Figure 4.2: Absorbance spectrum of proton-implanted Si showing the 817 cm^{-1} bending mode of H_2^*, shown in the inset.

The IR pump-probe setup is described in Chapter 3. The laser source is the TOPAS which delivers pulses at 1-kHz repetition rate with a time duration of ~2 ps, spectral width of 10 cm^{-1}, and a pulse energy of 12 μJ at 817 cm^{-1}. The transient bleaching signal S_b is detected using an amplified liquid nitrogen-cooled MCT detector. To allow for low temperature measurements, all experiments are performed with the sample mounted in an optical cryostat. The Si samples used for linewidth

measurements are 15 mm thick, grown by the float-zone method, and prepared by electron irradiation in Prof. Stavola's group at Lehigh University. The details about the electron irradiation are described in Chapter 2. The IR absorbance spectra are measured with a resolution of 0.1 cm^{-1} using a Bomen DA 3.16 Fourier transform infrared spectrometer.

4.3 Results and Discussions

4.3.1 Lifetime Measurements of Bend Mode of H_2^* in Si and Ge
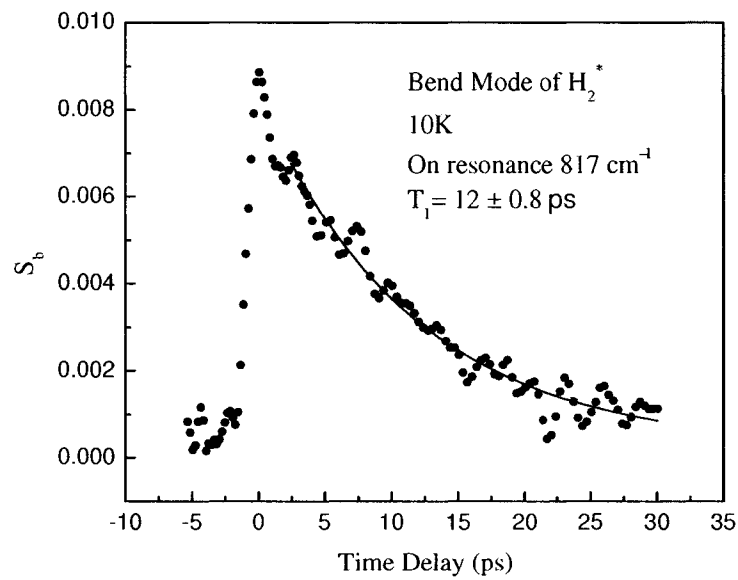
Figure 4.3: Decay of the transient bleaching signal S_b from the 817-cm^{-1} mode of H_2^* measured at 10 K with the TOPAS. S_b decays exponentially with a time constant of $T_1 = 12 \pm 0.8$ ps.

Figure 4.3 shows a semi-log plot of the transient bleaching signal versus time delay measured at 10 K with the laser frequency centered on the 817-cm^{-1} mode. The signal decreases with a time constant $T_1 = 12 \pm 0.8$ ps. Figure 4.4 shows the spectrum of our laser pulses. The dip at 813-cm^{-1} corresponds to the absorption of the bending mode of H_2^* at room temperature. Figure 4.4 also shows the band width with a FWHM of 10 cm^{-1} at 12.2 μm. When the wavelength is tuned off 817 cm^{-1} by 10 cm^{-1}, the exponential decay S_b disappears. Measurements of S_b vs wavelength show that the transient bleaching signal originates from the 817 cm^{-1} mode.
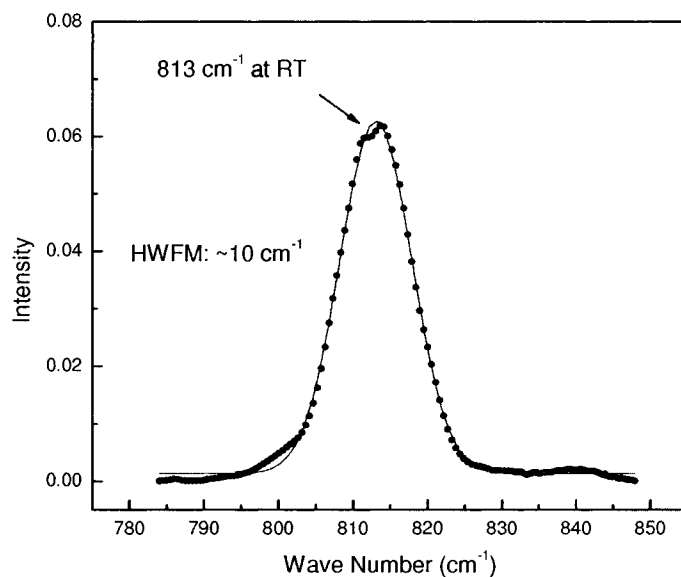
Figure 4.4: Spectrum of a 1.7 ps laser pulse passing through a monochromater, showing the absorption of the H_2^* bending mode at 813 cm^{-1} at room temperature.

As discussed in Chapter 2, the vibrational lifetime of the excited state of a local

vibrational mode can be estimated from

$$T_1 = \frac{1}{2\pi c \Gamma_0}, \tag{4.2}$$

where Γ_0 corresponds to the natural linewidth, which has to be measured at the highest resolution possible using samples with very low defect concentrations. The sample must be cooled to below 10 K for the absorption measurement to insure that the line broadening due to pure dephasing is negligible.

Figure 4.5(a) shows the absorption spectrum of H_2^* measured at 5 K using samples with H concentration of $\sim 1 \times 10^{16}$ cm^{-3}. The line shape of H_2^* is fitted by a Lorentzian with a FWHM of 0.42 cm^{-1}, which corresponds to a lifetime of 12.2 ps calculated by Eq. (4.2). This result shows that the lifetime measured in the time domain is exactly consistent with the one obtained in the frequency domain. The absorption linewidth is dominated by the homogeneous natural linewidth. The lifetime estimated from this low concentration sample is reliable. Since the vibrational lifetime of D_2^* is hard to measure due to the weak laser pulses at ~ 17 μm, we obtained the lifetime of D_2^* at 588 cm^{-1} by measuring its linewidth. The silicon sample containing D_2^* is prepared in the same way as H_2^*, and the line broadening at 5 K is dominated by its natural linewidth. From Figure 4.5(b) we obtain the absorption line width of 0.46 cm^{-1}, which corresponds to a lifetime $T_1 = 11.6$ ps. For this special case, it is very interesting to find that the lifetimes of H_2^* and D_2^* bending modes are almost the same. In the following, we will show that this result can be explained by the energy gap law, i.e., both modes fall into the two-phonon band of Si. To gain further insight, the

relaxation channel and decay mechanism need to be understood.
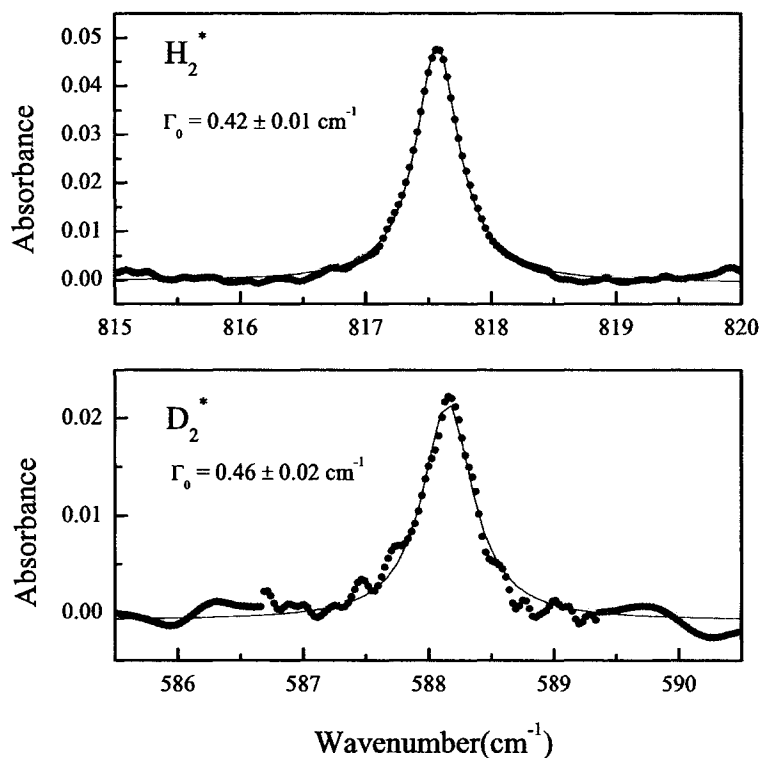
Figure 4.5: IR absorbance spectrum of e-irradiated, H-doped Si, showing the lines of H_2^* and D_2^*.

4.3.2 Decay Channel of the H_2^* Bend Mode

The nature of the accepting modes of H-related stretch modes is unknown [44, 94]. They can be Si-H bending modes, pseudolocalized modes, and/or phonon modes. In contrast, the decay channel of the bending modes may be less complicated because they are low-frequency modes and may decay directly into the phonon bath. To identify the relaxation channel we measured the temperature dependence of the lifetime.
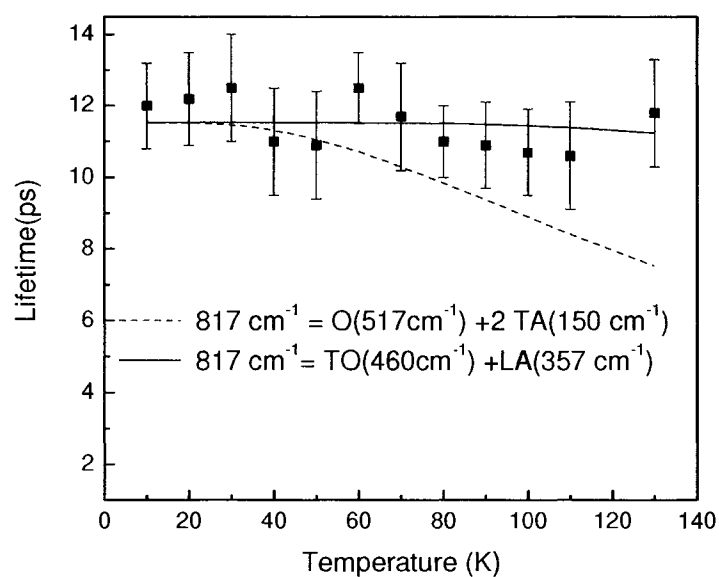
Figure 4.6: Temperature dependence of T_1 of the 817-cm^{-1} mode of H_2^*. The dashed and solid lines are the theoretical predictions for decay into three phonons {517, 150, 150} and two phonons {460, 357} cm^{-1}, respectively.

Figure 4.6 shows T_1 versus temperature for the bending mode of H_2^* at 817 cm^{-1} in silicon. T_1 is nearly constant up to 130 K. The lifetime measured above 130 K is not reliable due to the low signal-to-noise ratio. The solid line in Figure 4.6 shows a fit using Eq. (2.9) in Chapter 2 with the vibrational relaxation channel of the 817-cm^{-1} mode represented by two accepting modes {460 and 357} cm^{-1}. The dashed line is a fit using three accepting modes {517, 150 and 150} cm^{-1}, which corresponds to the phonon combination of one optical phonon at Γ point and two TA phonons. It is clear that the bending mode at 817 cm^{-1} decays via two-order process. The phonon decay channels are not uniquely determined by the temperature dependence of the lifetime. They can also be fitted well by other two-order processes. For example, the temperature dependence of the 817 cm^{-1} is equally well represented by 409 and 408 cm^{-1} accepting modes. However, any three-order process will not fit the data points. Since D_2^* and H_2^* fall into the two-phonon band of Si, we would expect that D_2^* also decays via the two-order process. Figure 4.7 shows the calculation of the two-phonon density of states by straightforward convolution of the one-phonon density of states according to Eq. (2.10) in chapter 3. The H_2^* bending mode at 817 cm^{-1} falls on the peak of the TO+LA phonon combination, whereas the D_2^* bending mode at 588 cm^{-1} coincides with TA+TO phonon combination. According to the symmetry selection rules described in Chapter 2, the decay channels of H_2^* and D_2^* are infrared active and the two-phonon decay channels are allowed.
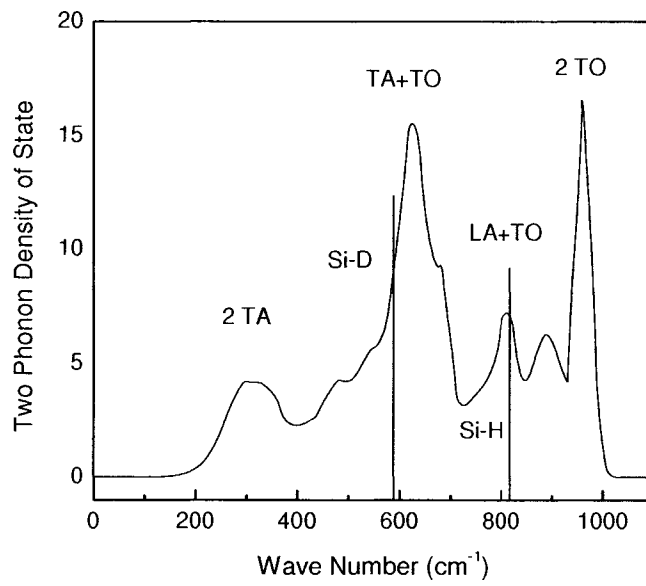
Figure 4.7: Two-phonon density of states in Si. The H_2^* bending mode at 817 cm^{-1} coincides with LA+TO phonons, whereas the D_2^* bending mode at 588 cm^{-1} lies in the TA+TO phonon band.

4.3.3 Lifetime of Other H-related Bend Modes and Energy Gap Law

Nitzan *et al.* developed a theory of vibrational energy relaxation in solids, which is described in Chapter 2. The vibrational relaxation rate is expressed in Eqs. (2.8), (2.9), and (2.10). The relaxation rate is determined by the magnitude of the coupling terms between local vibrational modes and accepting modes. Since the hydrogen bending mode decays by lowest order, it is reasonable to assume that the $|G_{\{\nu\}}|^2$ terms decrease fast with increasing order of the multiphonon process $N_{\{\nu\}}$. According to Eq. (2.12), the relaxation rate decreases exponentially as the energy gap between local modes and phonon modes or decay order is increased. The energy gap law can be expressed by [95, 96]

$$T_1 = Ae^{BN}, \tag{4.3}$$

where N is the decay order according to the lowest-order decay, and A and B are two parameters which depend on the coupling constants between the local vibrational modes and the accepting modes.

Figure 4.8 shows a plot of the vibrational lifetimes of H(D)-related bending modes vs decay order for various impurities in different semiconductors. The linewidth of Si-H bending mode in Si-doped GaAs at 896 cm^{-1} is $\sim$0.02 cm^{-1} [97], which corresponds to a lifetime of $\sim$260 ps. Since the maximum phonon frequency in GaAs is at 291 cm^{-1}, there must be at least 4 phonons involved in the decay process. The linewidth of Si-H bending mode at 890 cm^{-1} in Si-doped AlAs is 0.07 cm^{-1} [97], which corresponds
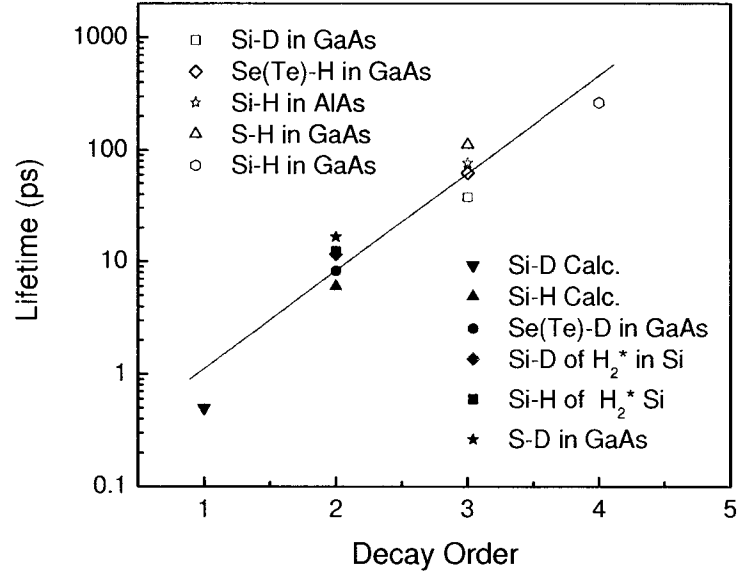
Figure 4.8: Vibrational lifetimes of H-related bending modes vs decay order in different hosts. The line is a fit to Eq. (4.3) with two parameters, $A = 0.15$ ps and $B = 2.01$

to a lifetime of $\sim$75 ps. The maximum phonon frequency of AlAs is 402 cm^{-1}, which leads to a decay order of 3. The linewidth of Si-D in GaAs at 641 cm^{-1} is around 0.13 cm^{-1} corresponding to $T_1 \simeq 40$ ps [98]. S (Se,Te)-H modes have almost the same frequencies with a linewidth of 0.045-0.09 cm^{-1} corresponding to $T_1 = 55$-110 ps [99], and a three-order process. In contrast, the linewidth of the corresponding D-modes are 0.3-0.6 cm^{-1} ($T_1 = 8$-16 ps) due to their two-order decay process. Tight-binding molecular dynamics simulations predict a lifetime of 0.3$\sim$0.5 ps for Si-D at 460 cm^{-1} and 5-6 ps for Si-H at 640 cm^{-1}. The solid line in Figure 4.8 is a fit using Eq. (4.3). This fit reveals the general trend that the vibrational lifetime of H(D)-related bending modes does follow closely an energy gap law. The data points are fitted with the values

$A = 0.15$ ps and $B = 2.01$. A is determined by the time scale of the first-order decay and B depends only logarithmically on the coupling constant and on N [95]. The coupling constant $B = 2.01$ is close to the value of the CN^- stretch mode in silver halides, which also follows the energy gap law with the fitting parameter $B = 1.94$ [96]. The variation of B from host to host is therefore small enough to justify the data analysis.

The overall fitting of the data point is satisfactory, but by no means perfect. There are a few possible errors in the lifetime of H(D)-related bending modes plotted in Figure 4.8: (1) Most of the lifetimes are estimated from their linewidths measured at low temperatures, which may have some inhomogenous broadening and not their real natural linewidth. (2) The linewidth may contain the instrumental broadening, especially those sharp lines. (3) Isotope broadening may contribute to the linewidth of Se (Te)-H or D modes in GaAs [100]. (4) The coupling constant can be slightly different in different hosts even though the calculations by Biswas [89] indicate that lifetimes of bending modes are insensitive to the environment. (5) The calculated Si-H lifetime is about half of our measured lifetime of H_2^*. We measured the Si-H lifetime to be ~ 12 ps, while the calculated lifetime of Si-H bending mode is only 5-6 ps. So the lifetime for Si-D mode may be larger as well, i.e., $\sim$ps according to the experimental data.

We already know that the Si-H stretch modes do not follow the energy gap law. For example, the H_2^* and $HV \cdot VH_{(110)}$ complex in Si have nearly the same frequency but very different lifetimes by two-orders of magnitude [101, 94]. Likely, the coupling

constant, accepting modes and decay mechanism of stretch modes are different and show a strong structure dependence as discussed in the next chapter. Our lifetime measurement of bending modes and analysis of energy gap law clearly shows that the lifetime of bending mode critically depends on the decay order, i.e., the energy gap between the local vibrational modes and accepting modes. The energy relaxation time can be different by 3 orders of magnitude when the bending mode decays into different number of phonons. Since the energy of the bending mode is smaller for deuterium than for hydrogen the former may decay via lower-order process which results in shorter lifetime. This result can explain the giant H (D) isotope effect and supports the finding that the dissociation of Si-H and Si-D bonds is controlled by the dynamics of hydrogen bending modes.

4.4 Conclusion

In conclusion, we have measured the vibrational lifetimes of Si-H and Si-D bending modes of H_2^* in Si and extended this study to many other bending modes in semiconductors. This study is key to understanding the physics of the giant isotope effect. We show that the vibrational lifetime of bending modes can be described by an energy gap law. The lifetime increases dramatically with increasing decay order.

Chapter 5

Hydrogen Stretch Modes in Silicon

5.1 Introduction

For a complete understanding of the vibrational dynamics of hydrogen in semiconductors, it is important to study also the lifetime of hydrogen stretch modes. In contrast to the bending modes, the stretch modes are high-frequency modes and can decay into phonons, bending modes, and/or pseudolocalized modes related with hydrogen defects. In 1975, Stein reported a pioneering infrared absorption study of crystalline silicon implanted with protons at room temperature (RT) [102]. The spectrum observed by Stein after implantation at ~ 80 K is dominated by an intense absorption line at 1990 cm^{-1} [103], which was identified as bond-center hydrogen (H$_{BC}^{(+)}$) shown in Figure 5.1(a). In proton-implanted Si, more than ten absorption lines are observed in the range 1800$\sim$2250 cm^{-1} at RT (Figure 5.2). The lines shift down in frequency by a factor of $1/\sqrt{2}$ when deuterons are implanted instead of protons. These Si-H or Si-D absorption lines can also be observed in Si grown in a H$_2$ ambient and subsequently irradiated with electrons [104, 105] or neutrons [106]. Local vibrational mode spec-

74

troscopy and uniaxial-stress techniques have been used to assign these Si-H stretch modes to specific hydrogen-related defects.

(a). $H_{BC}^{(+)}$ (b). H_2^* (c). IH_2

(d). $HV \cdot VH_{(110)}$ (e). VH_2 (f). VH_4
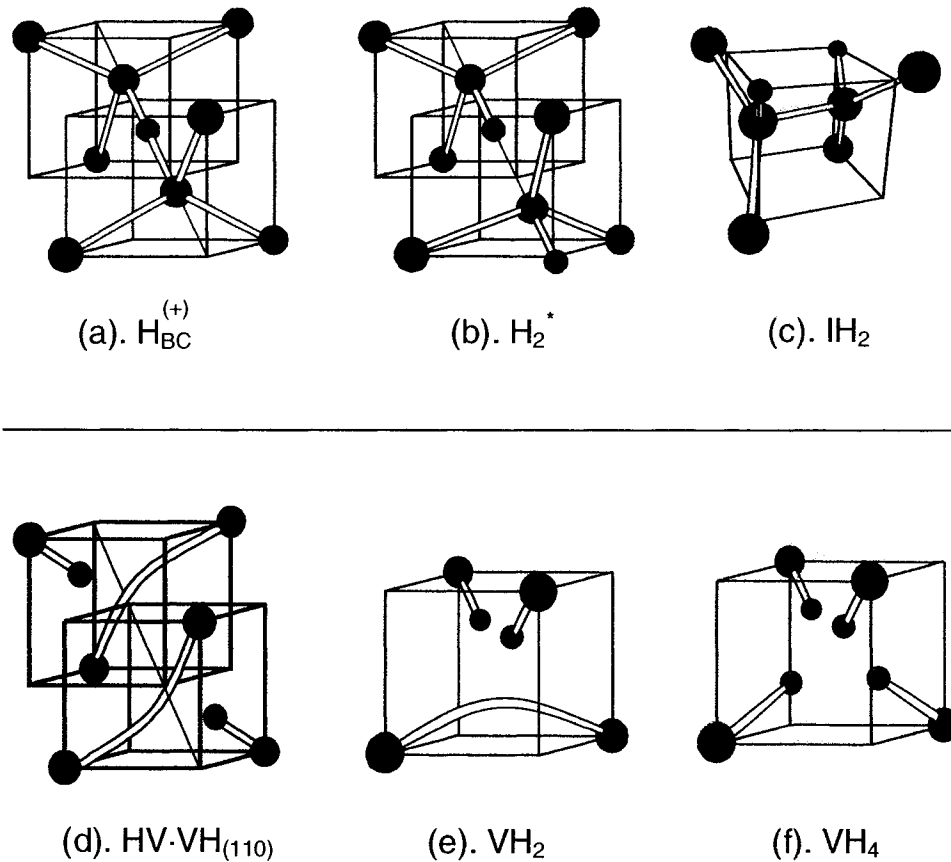
Figure 5.1: Structures of the interstitial-type defects (top), and the vacancy-type complexes (bottom). Large spheres are Si, whereas small spheres are H.

A number of defects have been identified, part of which are shown in Figure 5.1. Figure 5.1(a) shows the bond-center hydrogen defect in Si. It gives rise to an intense absorption line at 1998 cm^{-1} due to the excitation of the stretch mode, where the hydrogen vibrates parallel to the Si-H-Si bond axis. Figure 5.1(b) depicts the H_2^*
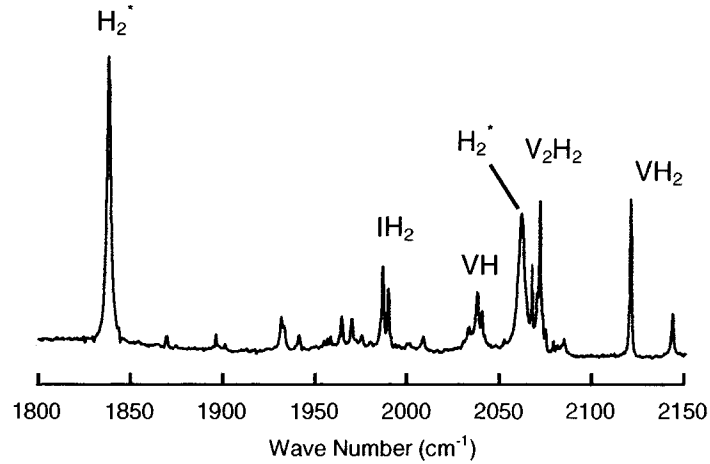
Figure 5.2: Absorption lines of hydrogen stretch modes in proton-implanted Si: H_2^* gives rise to two absorption lines at 1838 (BC site) and 2062 cm^{-1}(AB site); IH_2 is a self-interstitial defect and has two absorptions lines at 1987 and 1990 cm^{-1}; V_2H_2 has two Si-H stretch modes, but only one Si-H mode is IR active at 2072 cm^{-1}; VH consists of one hydrogen atom saturating a dangling bond of the vacancy, which was assigned to be 2038 cm^{-1}; VH_2 gives rise to two absorption lines at 2267 and 2316 cm^{-1}.

defect, which is described in Chapter 1 and 4. Figure 5.1(c) shows the self-interstitial hydrogen defects in Si. This defect contains two nearly perpendicular and equivalent Si-H bonds that are almost aligned with the [011] and [0$\bar{1}$1] directions and has a C_2 axis parallel to the [001] direction [107].

Vacancy type defects are also fundamental, intrinsic point defects in crystalline Si. Theoretical calculations [91, 108, 109, 110] predicted that a dangling Si bond represents the strongest trap for hydrogen in bulk Si and that a vacancy may trap up to four H atoms. The vibrational stretch frequencies were also calculated and exhibited a steady increase with increasing n for the VH_n complex. The atomic configuration of V_mH_n complexes are shown in Figure 5.1(d), (e) and (f). V_2H_2 was identified

by Suezawa in a hydrogenated Si sample by electron-irradiation [111]. This complex with a divacancy binding two H atoms is named $HV \cdot HV_{(110)}$ to emphasize that the Si-H bonds are located in the same (110) plane, in separate halves of the divacancy. VH_2 has C_{2v} symmetry and consists of two hydrogen atoms each saturating a dangling bond of the vacancy. VH_2 has two Si-H stretch modes at 2122 and 2145 cm^{-1}. VH_4 has all four dangling bonds of the vacancy saturated by hydrogen, which renders the complex electrically inactive. This complex has T_d symmetry and gives rise to a absorption line at 2223 cm^{-1}.

In order to understand the dynamics of these defects, the vibrational lifetimes of these local modes need to be measured. Initial vibrational lifetime measurements of H in crystalline Si were done by Budde [44] et al. for the bond-center hydrogen at 1998 cm^{-1}. The vibrational lifetime of the $H_{BC}^{(+)}$ stretch mode was measured to be 7.8 ps. The temperature dependence of vibrational lifetime showed that the $H_{BC}^{(+)}$ stretch mode does not decay via lowest order. The lifetimes of other H-related stretch modes were also estimated from their spectral widths. A structure dependence of the lifetime was found from the linewidth analysis in samples with very low defect concentrations [44]. The lifetimes of interstitial-type defects are much shorter than vacancy-type defects. This disparity in measured lifetimes is unexpected based on simple theories and is as yet unexplained [56, 57]. Experimentally, the most straightforward way to characterize a multiphonon relaxation rate from a given vibrational level is from the temperature dependence of its lifetime. In this chapter, we will discuss a detailed comparison of the temperature dependence of the vibrational lifetime of two structurally

distinct point defects in crystalline Si, H_2^*, an interstitial defect, and HV·VH$_{(110)}$, a vacancy complex. The very different temperature dependences show that these vibrationally excited defects decay into markedly different accepting vibrational modes, giving new insights into the origin of the observed large difference in their lifetimes.

5.2 Experimental
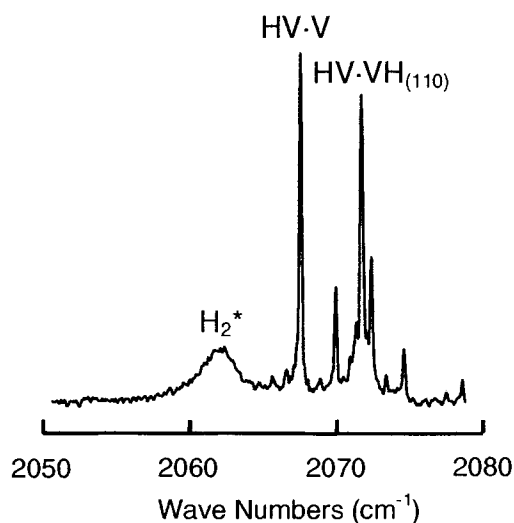
Figure 5.3: Absorbance spectrum of proton-implanted Si showing the 2062.1-, 2068-, and 2072.5-cm^{-1} lines of H$_2^*$, HV·V, and HV·VH$_{(110)}$.

The Si sample used for the lifetime measurement of H$_2^*$ bending mode is the same one used for stretch mode measurements as described in Chapter 4. After warming to room temperature, IR absorbance measurements from the implanted sample revealed a series of strong absorption lines in the Si-H stretch region, including lines at 2062.1, 2068, and 2072.5 cm^{-1}. Figure 5.3 shows an absorbance spectrum taken with 0.15-

cm^{-1} resolution at 10 K from a Si-H sample with a low H concentration ($\sim$7 ppm) to clearly resolve the different absorption lines. The 2068-cm^{-1} line has been assigned to the divacancy binding one H atom HV·V [112], and was $\sim$3 times smaller than the 2072.5-cm^{-1} line of V_2H_2 in the sample with the high H concentration. Since the linewidth is inversely related to the lifetime, it is immediately apparent that H_2^* and the vacancy complexes have very different excited state lifetimes. However, a direct determination of the lifetime from the width may be uncertain due to inhomogeneous broadening, instrumental resolution, and dephasing at elevated temperatures. Therefore, a transient bleaching (pump-probe) technique was used for time domain measurements of the lifetimes.

The transient bleaching signal S_b was measured as a function of time delay between the pump and probe pulses, as described in Chapter 2. The experiments were performed using the high-power, IR free-electron laser (FEL) at the Thomas Jefferson National Accelerator Facility (TJNAF). The FEL delivered pulses with a time duration of $\sim$1 ps, spectral width of 12 cm^{-1}, and pulse energy of 1 μJ at a pulse repetition rate of 18.6 MHz.
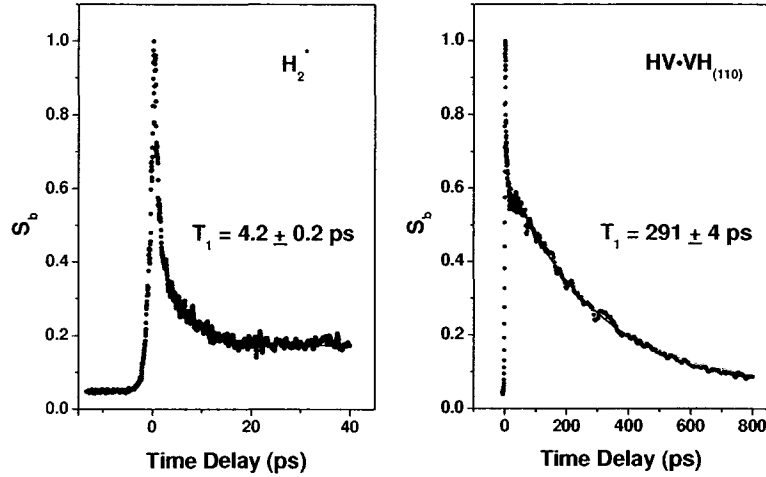
Figure 5.4: Transient bleaching signal from the 2062-cm^{-1} (left side) and the 2072-cm^{-1} (right side) mode measured at 10 K.

5.3 Results

5.3.1 Vibrational Lifetime of H$_2^*$ and HV·VH$_{(110)}$

Figure 5.4 shows the transient bleaching signal versus time delay measured at a temperature of 10 K with the laser frequency centered either on the 2062-cm^{-1} (left) or the 2072-cm^{-1} line (right). The signal of the former decreases with a time constant $T_1 = 4.2 \pm 0.2$ ps (left side of Figure 5.4). The lifetime of $T_1 = 4.2 \pm 0.2$ ps obtained directly from the transient bleaching experiment is longer than the $T_1 = 1.9$ ps estimated from the width of the 2062.1-cm^{-1} line measured in a low hydrogen concentration sample [101]. This indicates that the low-temperature linewidth is still broadened by intrinsic (homogeneous) dephasing processes. In addition, a long-lived tail is clearly present in the decay of S$_b$. Since the laser spectrum has a FWHM

of ~ 12 cm^{-1}, we expect that S_b also exhibits a response from the 2068- and 2072-cm^{-1} modes. Indeed, by centering the laser frequency on the 2072-cm^{-1} mode, the long-lived component of S_b is enhanced; i.e., it corresponds to the stretch mode of $HV \cdot VH_{(110)}$, possibly with a small contribution from $HV \cdot V$ (right side of Figure 5.4). The lifetime of the $HV \cdot VH_{(110)}$ stretch mode is constant within experimental error up to 60 K, with a mean value of $T_1 = 291 \pm 4$ ps. The contribution of the 2068-cm^{-1} line to S_b is expected to be very small since the transient bleaching signal is a nonlinear function of the laser intensity. In addition, the HV·VH$_{(110)}$ and HV·V defects are structurally very similar, and we therefore expect them to have similar lifetimes. Both signals in Figure 5.4 exhibit a fast transient, which coincides with the pump pulse. This instantaneous response results from the nonresonant excitation of the bulk crystal.

5.3.2 Temperature Dependence of Lifetime and Decay Channels

Figure 5.5 shows T_1 versus temperature for H_2^* (left side) and HV·VH$_{(110)}$ (right side). In the case of the 2062-cm^{-1} mode, T_1 is nearly constant up to ~ 60 K, where it starts to decrease, reaching half of its low-temperature value at 130 K. The solid lines in Figure 5.5 are fits using Eq. (2.9) in chapter 3 with the vibrational relaxation channel of the 2062-cm^{-1} mode represented by a set of six accepting modes {165, 165, 165, 522, 522, 522} cm^{-1}. This set of accepting modes is very similar to that
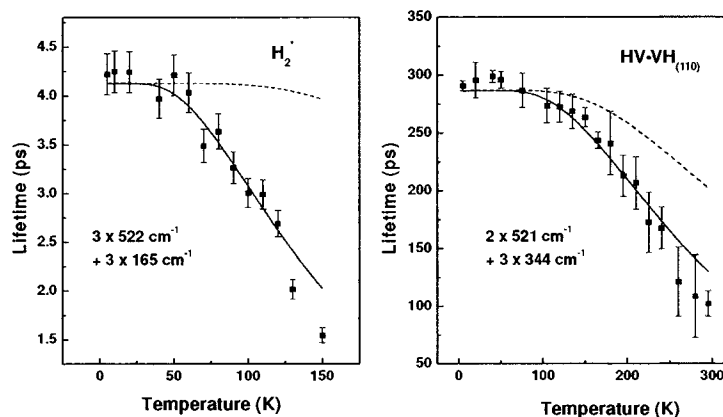
Figure 5.5: Temperature dependence of T_1 of the 2062-cm^{-1} mode of H_2^* (left side) and the 2072-cm^{-1} mode of HV·VH$_{(110)}$ (right side). The solid lines are fits from Eq. (2.9) in chapter 2 for decays into the sets of accepting modes $\{165, 165, 165, 522, 522, 522\}$ cm^{-1} and $\{343, 343, 343, 521, 521\}$ cm^{-1} of the 2062- and 2072-cm^{-1} modes. The dashed lines are fits of lowest-order decay channels.

of the 1998-cm^{-1} mode of bond-center H in Si, which is well described by decays

into six accepting modes, $\{150, 150, 150, 516, 516, 516 \}$ cm^{-1} [44]. In contrast,

the lifetime of the 2072-cm^{-1} mode starts to decrease at 120 K reaching half of its

low-temperature value at 250 K. The decay channel of the 2072-cm^{-1} mode is well

represented by five accepting modes with frequencies $\{343, 343, 343, 521, 521\}$ cm^{-1}.

We note that the vibrational relaxation channels are not uniquely determined by the

temperature dependence of the lifetimes. In particular, the high-frequency phonon

modes of the decay channels do not have a strong influence on the temperature

dependence of the lifetimes. For example, the temperature dependence of the 2072-

cm^{-1} mode is equally well represented by a set of accepting modes of $\{343, 343, 343,$

$343, 700\}$ cm^{-1}. However, the wave number of the accepting mode with the lowest

frequency is quite well determined by the onset of the temperature dependence of T_1, for example, 60 K for H_2^* and 120 K for HV·VH$_{(110)}$. Figure 5.5 also shows that in both cases the calculations using Eq. (2.9) deviate from the measured lifetimes at elevated temperatures, indicating that additional relaxation channels may increase the decay rate at higher temperatures. We note that the low-frequency accepting modes of 165 cm^{-1} for H_2^* (and 150 cm^{-1} for bond-center hydrogen) nearly coincide with transverse acoustic phonons of the undistorted Si crystal (Figure 5.6), which have been calculated in Reference [113]. Likewise, the 343-cm^{-1} modes involved in the decay of the stretch mode of HV·VH$_{(110)}$ nearly coincide with the peak in the longitudinal acoustic phonon density (Figure 5.6). The nature of these accepting modes is still unknown. However, likely candidates are perturbed optical, acoustic and/or pseudolocalized modes (PLMs) of these defects.
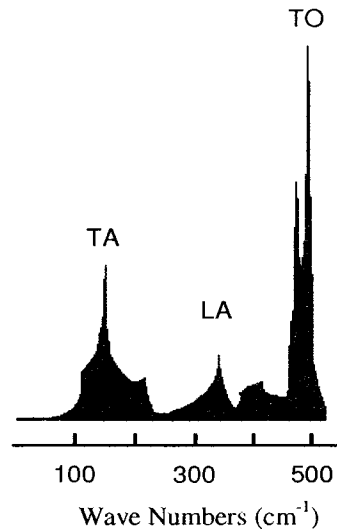
Figure 5.6: Phonon spectrum of Si adapted from Reference [113].

It has been accepted that high-frequency vibrational modes decay by lowest order according to Nitzan's theory [56, 57]. The coupling strengths are proportional to the derivative of the potential energy surface with respect to the normal coordinates of the Si-H stretch mode and the N_i accepting modes, corresponding to anharmonic terms of order $N_i + 1$. Since the magnitude of the anharmonic terms is believed to fall off rapidly with increasing order, channels with small N_i are likely to dominate the decay. The decay channel of both H_2^* and $HV \cdot VH_{(110)}$ with lowest order is the decay into four modes with frequencies at about 515 cm^{-1}, corresponding to optical phonons or possibly Si-related LVMs split off from the phonon bands by the strain fields in the vicinity of the defects. Figure 5.5 also shows that the temperature dependence of T_1 is incompatible with the Si-H stretch modes decaying predominantly into four modes at about 515 cm^{-1}. This is consistent with the fact that a combination of four optical phonons are not infrared active [69, 70] and therefore are not allowed as a decay channel. A low-frequency mode must be involved in the decay process of Si-H stretch modes in Si. This is different with the Si-H modes in amorphous Si, which decays into bending modes via lowest order [114] since phonons do not show high symmetry in amorphous hosts.

5.3.3 Structural Dependence of Lifetime of Hydrogen Defects

The H_2^* and $HV \cdot VH_{(110)}$ complexes show 2-orders-of-magnitude difference in their vibrational lifetimes. This is surprising at first glance considering that both Si-H stretch modes have nearly the same frequency and symmetry, and the compound density of accepting phonon states of the unperturbed lattice is almost identical. The vibrational lifetimes of other Si-H modes measured by infrared absorption spectroscopy at the highest resolution possible using samples with very low defect concentrations also show a strong structural dependence [101]. Table 5.1 shows that the lifetimes of Si-H stretch modes depend strongly on the bonding configuration of the defects. For instance, the interstitial-type defects H_2^* , IH_2 , and $H_{BC}^{(+)}$ have lifetimes of $4.2 - 12$ ps, whereas the lifetimes of vacancy-hydrogen complexes are at least $42 - 295$ ps. The strong structural dependence might be explained by either pseudolocalized modes or LVMs being involved in the decay process. Being localized around the defect, such modes have much larger vibrational amplitudes on the atoms close to the Si-H bond than, e.g., lattice phonons, which may cause a strongly enhanced anharmonic coupling to the Si-H stretch mode. However, significant distortions of the Si-Si bonds in the vicinity of the defects are required for pseudolocalized modes or LVMs to form [34] which is consistent with highly distorted interstitial-type defects having shorter lifetimes than vacancy-type defects. Furthermore, to explain the large difference in lifetimes, one should also consider the anharmonic coupling strength between

the stretch mode and the low-frequency modes. In the HV·VH$_{(110)}$ center, it certainly seems plausible that the relatively large open volume of the vacancies would lead to a small interaction between the hydrogen and the surrounding silicon atoms. This small interaction would lead to a longer vibrational lifetime.

Defect	Si-H ω (cm^{-1})	Si-H T_1 (ps)
H_2^*	2062.1	1.9 (4.2)
IH_2	1987.1	12
IH_2	1990.0	11
VH_2	2122.3	60
VH_2	2145.1	42
VH_4	2223.0	56
$HV \cdot VH_{(110)}$	2072.5	262 (295±6)

Table 5.1: Lifetimes of H-related stretch modes in Si measured at 10 K. To obtain the lifetimes shown in column 3, the linewidths were corrected for instrumental broadening and then entered into equation $T_1 = 1/(2\pi c\Gamma_0)$.

The coupling term of H$_2^*$ and HV·VH$_{(110)}$ has been simulated by Budde [78, 115] using a simple Morse potential, which includes anharmonic effects and is known to represent the bonding of diatomic molecules quite accurately. The model hamiltonian of the two coupled oscillators is given by

$$H = -\frac{\hbar^2}{2\mu_1}\frac{\partial^2}{\partial r_1^2} - \frac{\hbar^2}{2\mu_2}\frac{\partial^2}{\partial r_2^2} + D_1[e^{-a_1 r_1} - 1]^2 + D_2[e^{-a_2 r_2} - 1]^2 + f_{12}r_1 r_2, \qquad (5.1)$$

where μ_1 and μ_2 are the effective masses, and r_1 and r_2 are the displacement coordinates corresponding to bond stretching. $f_{12}r_1 r_2$ is the coupling term which determines the coupling strength of the two oscillators. In this simulation, the coupling constant f_{12} of H$_2^*$ is about 50 times larger than of HV·VH$_{(110)}$. This calculation shows that the

two Si-H stretch modes strongly couple to each other in H_2^* and the energy dissipation is much faster than in HV·VH$_{(110)}$.

5.4 Conclusion

Vibrational lifetime measurements of Si-H stretch modes have great significance in excitation processes which involve the dynamics of energy dissipation in solids. A specific example is the desorption of H at the Si/SiO$_2$ interface [116, 88, 90]. The rate of H loss is a sensitive function of the excitation to vibrational states of the Si-H bond and the lifetimes of these states. The results presented here indicate that the relevant lifetime is a strong function of the local defect configuration. Thus quantitative models of these processes require detailed knowledge of the local structure and the associated local phonons. In conclusion, we have measured the vibrational lifetime of the Si-H stretch mode of two structurally distinct point defects in Si, H_2^*, and HV·VH$_{(110)}$, as a function of temperature. We have shown that the dominating decay channels of these defects are significantly different, involving low-frequency accepting modes (165 and 343 cm^{-1}) of very different symmetry. It is suggested that this highly selective behavior is due to the nature of the local distortions and the associated pseudolocalized phonon modes. A more detailed understanding of the nature of these PLMs is required to fully elucidate the vibrational energy relaxation and transfer channels in solids.

Chapter 6

Interstitial Oxygen in Si and Ge

6.1 Introduction

Oxygen is one of the most common and technologically important impurities in Czochralski (CZ)-grown silicon and germanium, which are the dominant materials used for the fabrication of electronic devices. Si grown by CZ has a high concentration of oxygen ($\sim 10^{18}$ cm^{-3}), which is incorporated as a result of the dissolution of the SiO$_2$ crucible at the growth temperature. The concentration of oxygen is less than 10^{16} cm^{-3} in crystals prepared by the floating zone method. The oxygen impurity critically affects the properties and yield of the devices. At high temperatures it forms aggregates or clusters within silicon, as well as interstitial dislocation loops. These all disrupt the lattice and lead to defect states in silicon. At lower temperatures oxygen can still be a problem, for example through the formation of thermal donors which occur when silicon is annealed at temperatures of around 450°C. These defects are electrically active, and act as electron-hole recombination centers, lowering the mobility, etc. For this reason, it is essential to understand exactly how oxygen behaves

88

in silicon. A full understanding of the bonding and structure, as well as the diffusion and kinetics of oxygen, will yield to improved manufacturing processes. This in turn should lead to faster, cheaper, and more efficient microchip technology [117].

Because oxygen is lighter than Si and Ge atoms, it forms local vibrational modes in Si and Ge crystals. The most well studied oxygen LVM absorption is known as the 9-μm line appearing at 1107 cm^{-1} at room temperature [118, 119]. Oxygen in germanium, first investigated at about the same time [120, 121], has a similar structure as oxygen in Si and gives rise to an absorption line at 11.7 μm. Due to the lower melting point and lower oxygen affinity of Ge, the intensity of the 11.7-μm band is two orders of magnitude smaller than that of the corresponding 9-μm band in crucible-grown Si. Recently, oxygen in Ge has been reinvestigated more actively, due to progress in spectroscopy and to the availability of quasi-monoisotopic (qmi) germanium samples [122, 123, 124, 125, 126, 127].

In the early work by Kaiser et al. [118], a model was proposed in which the oxygen atom occupies an interstitial position, bonded to two Si neighbors, similar to the Si-O-Si unit in quartz. The uniaxial stress experiments done by Corbett [121] confirmed that Si-O-Si complexes are aligned along $\langle 111 \rangle$ direction. The structure is shown in Figure 6.1. From *ab initio* calculations [128], it was found that the Si-O bond length is 1.59 Å and the Si-O-Si angle is 172°. While in equilibrium geometry the Ge-O bond length is 1.70 Å and the Ge-O-Ge angle is 140° [127].
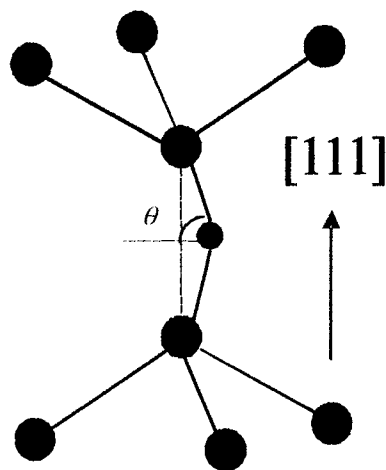
Figure 6.1: Structure of interstitial oxygen in Si and Ge

6.1.1 Vibrational Spectroscopy of Interstitial Oxygen in Si and Ge

Infrared vibrational spectroscopy is one of the most powerful techniques to characterize oxygen defects in Si and Ge. The interstitial oxygen in Si and Ge has been assigned to the virtual molecule with C_{2v} symmetry [129, 130, 131]. Early studies on interstitial oxygen in silicon (Si:O_i) showed two main absorption features in the infrared (519 cm^{-1} and 1136 cm^{-1}) and another structure in the far infrared (29 cm^{-1}). The three main features were associated with the three fundamental vibrational modes of a puckered Si$_2$O molecule, ν_1 (the 519 cm^{-1} peak), ν_2 (the 29 cm^{-1} band), and ν_3 (the 1136 cm^{-1} or 9 μm stretching band), as displayed in Figure 6.2. The analysis of the fine structure of the high- and low-frequency features [129] offered insight into the nature of the microscopic structure of the oxygen center and

its dynamics. In spite of the correctness and merit of this analysis, it was only recently shown that the puckered image was misleading, a better one being that of a pseudo-molecule Si_3 $\equiv Si$-O-$Si\equiv$ Si_3 with dynamic D_{3d} symmetry [132]. The assignments were consequently revised: the 519 cm^{-1} peak is not a vibration of the Si_2O pseudomolecule (not shown in Figure 6.2), but a backbond Si-Si vibration of E_u symmetry of the corresponding D_{3d} point group. The stretching mode (ν_3) remains essentially unchanged, being of A_{2u} symmetry. The equivalent to the ν_1 mode is an A_{1g} symmetric stretching mode invisible to the infrared, located at around 600 cm^{-1}. The observed combination mode at 1750 cm^{-1} is a combination of the A_{1g} and A_{2u} modes, or ($\nu_1+\nu_3$). Its isotope shift strongly supports this new model [133].
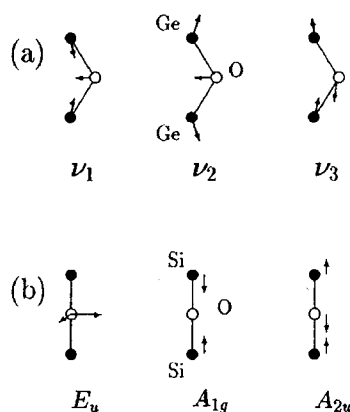
Figure 6.2: Fundamental vibrational modes of (a) the puckered Ge_2O and (b) the linear Si_2O quasimolecule. The traditional molecular nomenclature has been adopted for Ge_2O. For Si_2O the nomenclature corresponds to the D_{3d} point group, appropriate for the linear structure.

In the case of interstitial oxygen in germanium ($Ge:O_i$), infrared-absorption bands have been reported near 860 and 1270 cm^{-1}, which are equivalent to the 1136 and

1750 cm^{-1} bands in Si:O$_i$. Low-energy absorption lines have also been detected by phonon spectroscopy, at a much lower energy scale than the far-infrared absorption in Si [123], but there is no report on any feature in the intermediate frequency range.

The excitation dynamics of oxygen in Si and Ge has been well studied. It was observed that there are a few side bands on the low-energy side of 1136 cm^{-1} line when the temperature was raised above 20 K [129] (see Figure 6.3). Yamada-Kaneta [132, 134] et al. have quantified the coupling interaction by formulating the Hamiltonian for the problem as the sum of the low-energy mode with a phenomenological potential $\alpha r^2 + \beta r^4$, the one-dimensional simple harmonic ν_3 mode, and an anharmonic coupling between them. This model proposes a two dimensional low energy anharmonic excitation of the oxygen complex due to the coupled A$_{2u}$ and A$_{1g}$ modes. This coupling causes the fine structure of 9-μ band.
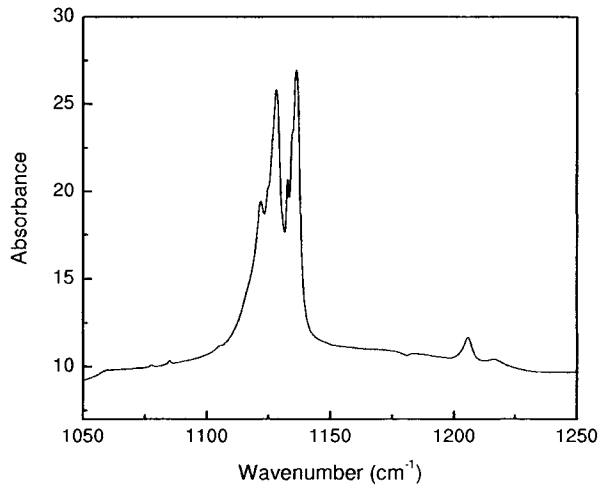
Figure 6.3: Absorption spectrum of the asymmetric mode of ^{16}O$_i$ in Si measured at 60 K showing the side bands on the lower energy side.
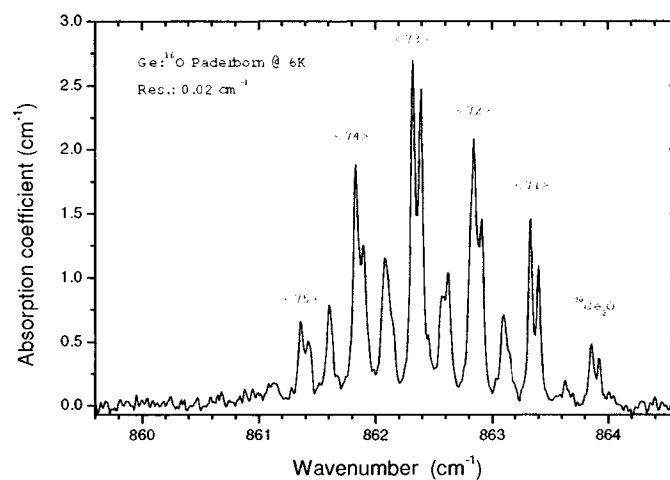
Figure 6.4: Absorption spectrum of the asymmetric mode ν_3 of O_i in natural Ge at 6 K. The spectrum shows the complex fine structure arising from different Ge isotopes and pairs of lines due to coupling between ν_3 mode and oxygen rotational motion. Each peak is identified by the average Ge isotopic mass. The average linewidth is ~ 0.04 cm^{-1}.
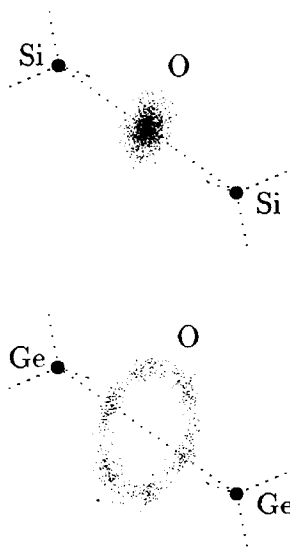
Figure 6.5: Delocalization of oxygen in Si:O_i and Ge:O_i in the plane perpendicular to the Si-Si (Ge-Ge) axis. The O_i motion is radial in Si and rotational in Ge.

The absorption band of oxygen stretch mode in Ge (ν_3) has a different structure than in Si. Unlike Si, where ^{28}Si is much more abundant than ^{29}Si and ^{30}Si, the Ge isotopes occur with comparable abundances. As a result, at very low temperatures, the ν_3 mode of oxygen in Ge exhibits a complex spectrum as shown in Figure 6.4, with as many as 44 sharp lines within a 5-cm^{-1} range associated with the 11 distinct isotopic combinations of the two Ge atoms [125]. On the other hand, oxygen in Ge does not show a two-dimensional motion, but a rotation (see Figure 6.5). The coupling of this rotational motion and asymmetric stretch mode ν_3 gives rise to additional lines.

The microscopic structure of the defect center and the excitation dynamics of interstitial oxygen in Si and Ge are well understood. This is an ideal system for studying vibrational relaxation mechanisms in semiconductors, which are important to elucidate diffusion and defect reactions involving oxygen impurities [135]. Recently, McCluskey and co-workers used hydrostatic pressure to bring the asymmetric stretch mode of ^{18}O$_i$ in Si into resonance with a spatially extended mode and studied the resonant interaction between these two modes [68]. The authors stated that the transition from a localized to an extended mode might be the first step toward decay into lattice phonons. However, little is known about the actual decay dynamics of the local vibrational mode into lattice phonons.
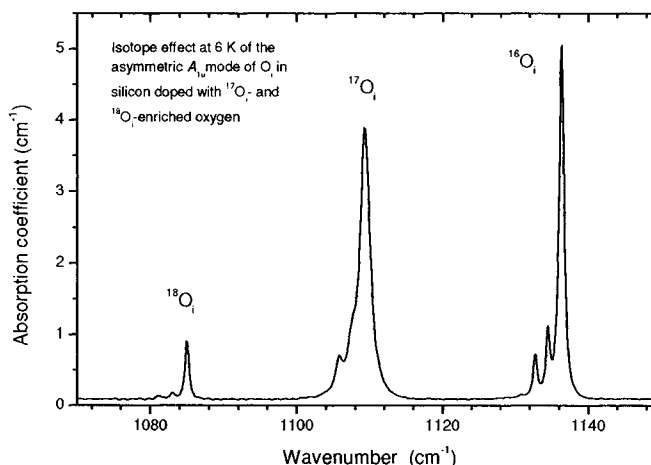
Figure 6.6: Absorption spectrum of the asymmetric stretch mode of O_i for different O isotopes in Si samples enriched with ^{17}O and ^{18}O. The linewidth of ^{17}O mode is 1.2 cm^{-1}, while it is 0.6 cm^{-1} for ^{16}O and ^{18}O.

6.1.2 Isotope Effect of Oxygen in Si

In the past, isotope substitution of the oxygen center with ^{16}O, ^{17}O, and ^{18}O has been useful for experimental understanding of oxygen-related LVMs in Si and Ge. However, the full width at half maximum (FWHM) of the asymmetric stretch mode of $^{17}O_i$ in Si (1109 cm^{-1}) is a factor of 2 larger than for the $^{16}O_i$ (1136 cm^{-1}) and $^{18}O_i$ mode (1085 cm^{-1}) as shown in Figure 6.6, a puzzle that has not been solved since 1995 [133]. This broadening does not depend on the ^{17}O concentration and it is not observed for the low-frequency mode at 29 cm^{-1}. Thus, the ground state is not broadened. The broadening must be from the excited state. In principle, a broadening could result from the splitting of the 5/2 spin level of ^{17}O by quadrupole interaction with an electric field gradient in the vibrational excited state. However,

in order to explain the observed broadening for ν_3 (^{17}O), one would need a very large field gradient, about a hundred times larger than typically found for ground states in semiconductors [133]. The effect was not observed in Ge which rules out that it is intrinsic to ^{17}O. The effect may be related to the vibrational lifetime and to the coupling between the local modes and the lattice phonons. It is therefore crucial to measure the vibrational lifetimes of oxygen isotopes in Si.

The other interesting question is that the linewidth of ^{16}O in Ge is much sharper than in Si. Infrared absorption measurements show that the average line width of ^{16}O mode in Ge is 0.04 cm^{-1}, i.e., a factor of 10 narrower than in Si [122]. Interstitial oxygen in Si and Ge have similar defect structures and excitation dynamics. The different linewidths may indicate different relaxation dynamics of these two modes in Si and Ge. Figure 6.4 shows the absorption spectrum measured at 7 K at a resolution of 0.02 cm^{-1} in Ge sample.

6.2 Experimental

Natural Si is made up from ^{28}Si (92.2%), ^{29}Si (4.7%) and ^{30}Si (3.1%), and its isotope shift of vibrational lines can be observed by infrared absorption spectroscopy. The composition of oxygen in Si consists of ^{16}O (99.76%),^{17}O (0.04%) and ^{18}O (0.2%). A float-zone grown silicon sample enriched with oxygen isotopes by diffusion is used for the lifetime experiment. The concentrations of ^{16}O, ^{17}O and ^{18}O isotopes are 20, 25 and 2.4×10^{16} cm^{-3}, respectively. The germanium sample contains isotopes ^{70}Ge,

^{72}Ge, ^{73}Ge, ^{74}Ge, ^{77}Ge, with relative (natural) abundances of 0.205, 0.274, 0.078, 0.365 and 0.079, respectively. The oxygen concentration of the Ge sample is 4.9×10^{16} cm^{-3}. The lifetime of the asymmetric stretch mode of interstitial oxygen isotopes is measured directly by transient bleaching spectroscopy. We use an IR pump-probe setup, as described in Chapter 3. The TOPAS used in this experiment delivers pulses at 1-kHz repetition rate with a time duration of ~ 1.7 ps, spectral width of 16 cm^{-1}, and a pulse energy of 18 μJ at 1136 cm^{-1} and 1109 cm^{-1}, and 9 μJ at 861 cm^{-1}. The transient bleaching signal S_b is detected using an amplified liquid nitrogen-cooled HgCdTe detector. To allow for low temperature measurements, all experiments are performed with the sample mounted in an optical cryostat.

6.3 Results and Discussions

6.3.1 Lifetime Measurements

Figure 6.7 shows a semi-log plot of S_b vs time delay from the asymmetric stretch mode of $^{16}O_i$ and $^{17}O_i$ in Si at 10 K. Both decay profiles fit well to a single exponential function, yielding a lifetime $T_1 = 11.5 \pm 1$ ps for $^{16}O_i$, and $T_1 = 4.5 \pm 0.4$ ps for $^{17}O_i$. We could not measure the lifetime of the $^{18}O_i$ mode because of its low concentration. The data shown in Figure 6.8 are measured at a center frequency of 1123 cm^{-1}, i.e., between the two modes. The curve does not exhibit any decay process, but only the laser pulse with 1.7-ps width. The TOPAS spectrum with a FWHM of 16 cm^{-1}
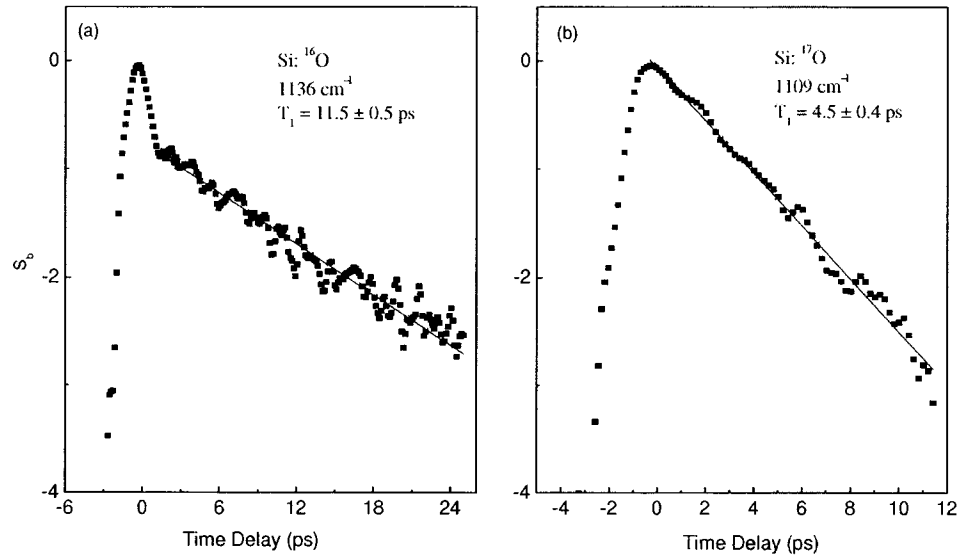
Figure 6.7: (a) The transient bleaching signal S_b decays exponentially with a time constant $T_1 = 11.5\pm1$ ps for the asymmetric stretch mode of $^{16}O_i$ in Si at 10 K; (b) while $T_1 = 4.5\pm0.4$ ps for $^{17}O_i$.

(Figure 6.9) is therefore narrow enough to distinguish between the two vibrational modes of the oxygen isotopes in Si.

The narrow band width enables us to tune the wavelength into resonance with the $^{16}O_i$ and $^{17}O_i$ mode in Si. The 1.7-ps pulse width and 16 cm^{-1} band width are ideal parameters to measure the vibrational lifetime of these two modes. If the band width is too narrow, the pulse will be too long to measure the lifetime of $^{17}O_i$ mode since the lifetime of $^{17}O_i$ is only 4.5 ps. If the band width is too wide, it will not distinguish the two modes.

Figure 6.6 shows the infrared absorption spectrum of the asymmetric stretch mode of different oxygen isotopes measured from the Si sample by B. Pajot in Paris. This
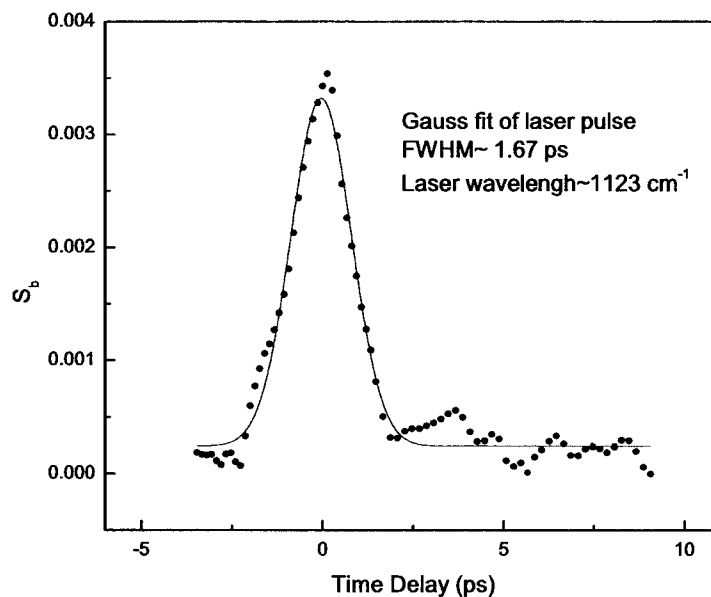
Figure 6.8: The transient bleaching signal S_b measured at a center frequency of 1123 cm^{-1}, which lies between the $^{16}O_i$ and $^{17}O_i$ mode. The signal does not show any decay. It is fitted by a Gaussian function, giving the pulse width of ~ 1.7 ps.
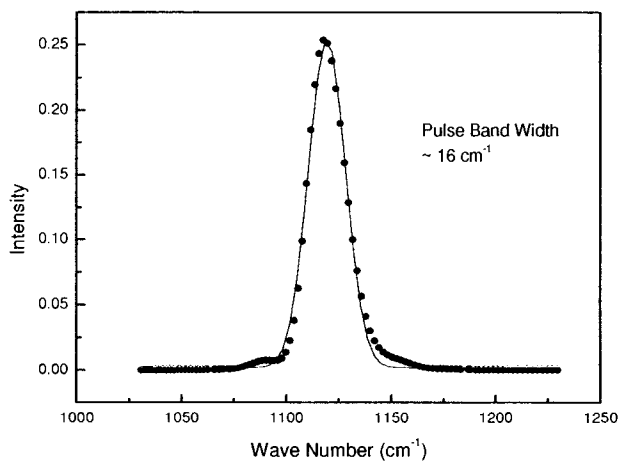
Figure 6.9: The laser pulse spectrum has a band width of 16 cm^{-1} at ~ 9 μm measured with a monochromator.

measurement was performed at liquid helium temperature using a BOMEN DA3 Fourier transform spectrometer with spectral resolution of 0.1 cm^{-1}. The shape of an absorption line is generally given by the convolution of its homogeneous line shape with a function describing the inhomogeneous broadening [136]. The FWHM of the $^{17}O_i$ line is $\sim$1.2 cm^{-1}, while for $^{16}O_i$ and $^{18}O_i$ it is $\sim$0.6 cm^{-1} at 7.5 K. We also measured the linewidth of $^{16}O_i$ mode in a Si sample with lower oxygen concentration ($\sim 10^{16}$ cm^{-3}). The linewidth of the $^{16}O_i$ mode at 10 K was found to be $\Gamma = 0.55$ cm^{-1}, which is shown in Figure 6.10.
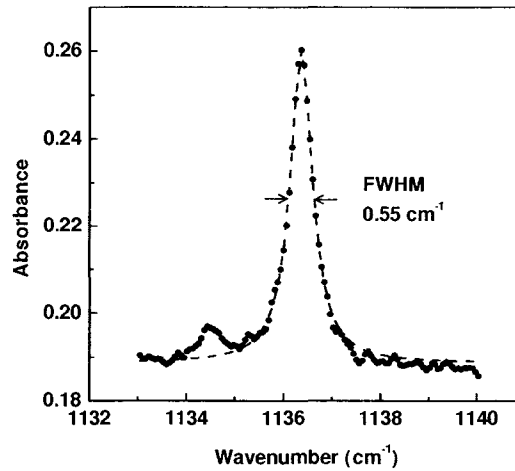
Figure 6.10: Absorption spectrum of the asymmetric stretch mode of $^{16}O_i$ measured in a float-zone Si sample with oxygen concentration of $\sim$ 0.2 ppm. The linewidth is 0.55 cm^{-1}.

The natural linewidth deduced from the lifetime is 1.12 cm^{-1} for $^{17}O_i$, and 0.44 cm^{-1} for $^{16}O_i$. Our results in the time domain are therefore consistent with those in the frequency domain, which shows that the absorption lines of interstitial oxygen are homogeneously broadened in crystalline silicon at low temperature. This consistency

has been shown for hydrogen-related models in crystalline silicon in the time and frequency domain [44, 101]. We can therefore deduce the lifetime of the $^{18}O_i$ mode from the linewidth to be $\sim$10 ps, close to that for $^{16}O_i$. The difference (factor of two) between the linewidths of $^{17}O_i$ compared with $^{16}O_i$ and $^{17}O_i$ is also observed in their lifetimes.
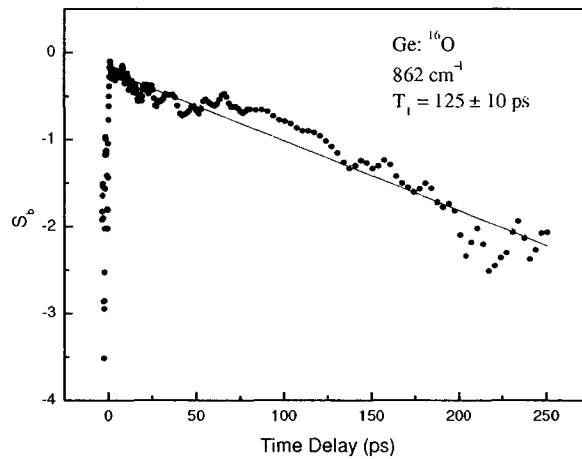
Figure 6.11: The transient bleaching signal S_b decays exponentially with a time constant $T_1 = 125 \pm 10$ ps for the asymmetric stretch mode of $^{16}O_i$ in Ge at 10 K.

In order to elucidate the difference of the linewidth of $^{16}O_i$ in Si and Ge, we measured the vibrational lifetime of $^{16}O_i$ in Ge. Figure 6.11 shows the lifetime of the asymmetric stretch mode, which was measured to be $T_1 = 125 \pm 10$ ps at 10 K. Since the absorption lines of the $^{16}O_i$ mode for different Ge isotopes are very close, our laser pulses can measure only an average lifetime. This corresponds to an average linewidth of 0.04 cm^{-1}, which is consistent with the absorption spectrum shown in Figure 6.4. This indicates that at low temperature and low defect concentration the

$^{16}O_i$ mode in Ge is dominated by the natural linewidth.

6.3.2 Multiphonon Density of States and Decay Channels

The asymmetric stretch mode of O_i lies in the three-phonon continuum of Si and is expected to decay by a three-phonon process. It is therefore necessary to calculate the compound three-phonon density of states. The compound three-phonon density is given by

$$\rho_{\{\nu\}} = \int dE_1 \int dE_2 \ldots \int dE_{N-1} \rho_1(\hbar\omega - E_1)\rho_2(E_1 - E_2)\ldots\rho_N(E_{N-1}). \quad (6.1)$$

The one-phonon density of states was obtained from *ab initio* calculations, which are available in the literature [137, 138]. The dispersion curves in Figure 6.12 are for Si and Ge. The graphs on the far right side show the density of states, which are obtained by integrating over the dispersion curves, giving the density of phonon modes as a function of frequency (in unit of wavenumber, cm^{-1}). Si and Ge have identical crystal structure, so their dispersion and density of states curves are very similar, with Ge having lower frequencies because its mass is higher than Si. Phonon-dispersion relations can be determined experimentally by inelastic neutron scattering. The markers along the curves in Figure 6.12 are experimental data points. The theoretical calculations are very reliable.

Figure 6.13 shows the three-phonon density of states for Si calculated by straightforward convolution of the one-phonon density of states according to Eq. (6.1). The
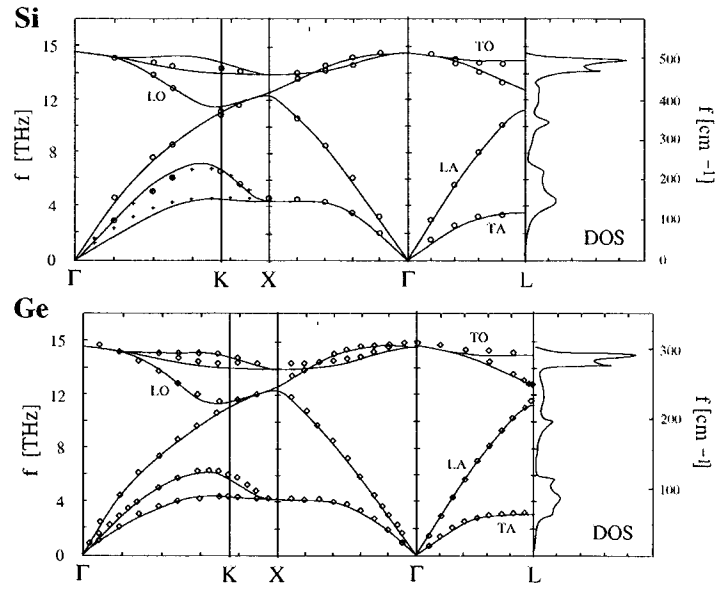
Figure 6.12: Phonon dispersion curves and density of states for Si (top) and Ge (bottom). Si figure is courtesy of Wei [138], Ge figure is courtesy of Giannozzi *et al* [137].

$^{17}O_i$ mode happens to fall right on the peak of the 2TO + 1TA phonon combination, whereas the $^{16}O_i$ and $^{18}O_i$ mode are on both sides with smaller combined phonon densities. High phonon density corresponds to a short lifetime. The difference of the phonon density provides a satisfactory explanation for the difference of the lifetimes. The ratio of the phonon densities at the frequencies of the $^{17}O_i$ and $^{16}O_i$ mode is ~1.3, which is smaller than the ratio of the lifetimes (~2.5). The overall agreement between the calculations and the experiment is satisfactory, but is by no means perfect. In a full treatment of vibrational relaxation by anharmonic coupling between LVM and lattice phonon modes, one should consider modifications introduced by the distortion of the lattice because of the impurities, which may affect the phonon density of states

locally [139].
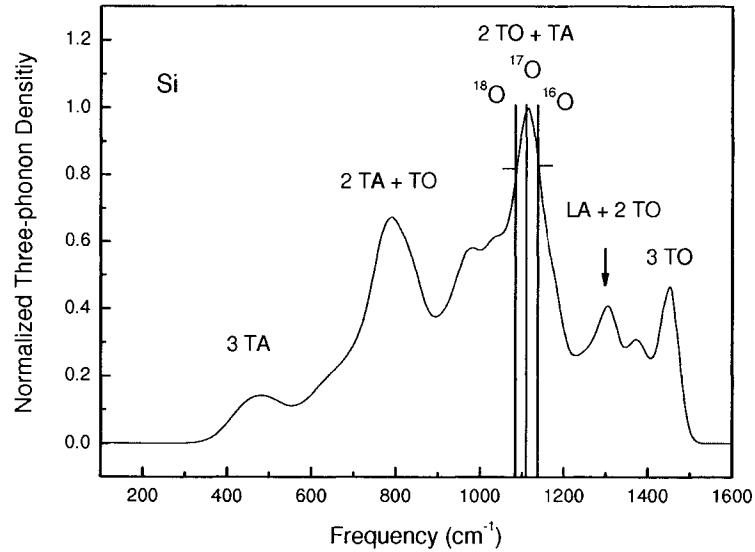
Figure 6.13: Normalized three-phonon density of states in Si at 0 K. The asymmetric stretch mode of $^{17}O_i$ coincides with the highest three-phonon density in Si, whereas the $^{16}O_i$ and $^{18}O_i$ modes are on both sides of the 2TO + 1TA phonon peak.

Recently, Kato and coworkers reported a surprisingly large effect of Si isotopic mass disorder on the linewidth of the asymmetric stretch mode of $^{16}O_i$, which cannot be explained well by their calculations [140]. Our lifetime measurements indicate that the line broadening of the $^{16}O_i$ mode is dominated by the natural linewidth at low temperatures. The linewidth of this mode in quasi-mono-isotopic (qmi) ^{29}Si and ^{30}Si samples are narrower than those in natural Si and ^{28}Si. This can be explained by the isotopic shift of the phonon frequency rather than the isotopic mass disorder. Passing from ^{28}Si to ^{30}Si, the phonon frequency will shift to a lower wave number, which results in lower phonon densities for ^{29}Si and ^{30}Si than for natural Si at the

frequency of the $^{16}O_i$ mode.
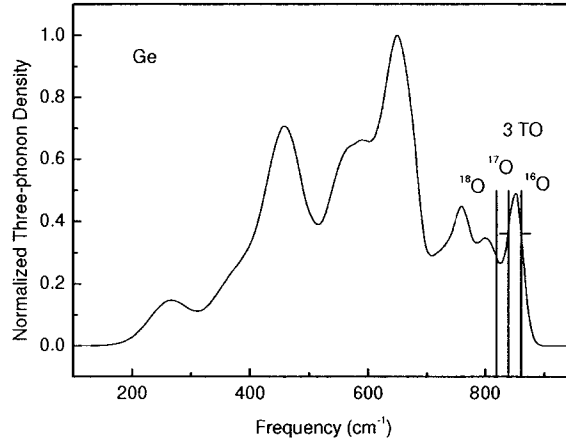
Figure 6.14: Normalized three-phonon density of states in Ge at 0 K. The $^{16}O_i$ and $^{17}O_i$ modes lie in the 3TO phonon band, whereas the $^{18}O_i$ mode coincides with a 2TO + 1LO phonon process.

To elucidate the long lifetime of the asymmetric stretch mode of $^{16}O_i$ in Ge requires knowledge of the decay channels and phonon density of states. The 862-cm^{-1} mode falls into the three-phonon continuum since the cut-off frequency of phonons in Ge is 306 cm^{-1}. Figure 6.14 shows the calculated three-phonon density of states in Ge similar to the one of Si. The $^{16}O_i$ and $^{17}O_i$ modes fall on the 3TO phonon peak in Ge while they coincide with 2TO + TA phonon processes in Si. The oxygen isotope effect has been investigated also in Ge [141]. A resonant broadening of the $^{17}O_i$ absorption line compared with $^{16}O_i$ and $^{18}O_i$ has not been observed in Ge, but the individual lines of $^{18}O_i$ are broader than those for $^{16}O_i$ and $^{17}O_i$. The $^{16}O_i$ and $^{17}O_i$ lines coincide with the same peak (3TO phonons), both of them have the same decay channel and their three-phonon density of states is close. So they show the same linewidth in

Ge. The $^{18}O_i$ mode in Ge may have different coupling constant since it decays into a different channel (2TO + LO phonons).

6.3.3 Symmetry Analysis

The difference in phonon density between the 2TO + 1TA and 3TO phonon combinations is only a factor of 2~3, which is not enough to explain the large difference in lifetimes of $^{16}O_i$ in Si and Ge. Since the decay channels are different, it is necessary to account for the different coupling constants $G_{\{\nu\}}$, representing the strength of the interaction between the local mode and the accepting modes. The asymmetric stretch mode of interstitial oxygen in Si and Ge has A_{2u} symmetry, which is infrared active in the D_{3d} point group of the O_i defect. The three-phonon combinations must contain A_{2u} symmetry [20], or otherwise the decay channel is not allowed. The infrared dipole operator whose irreducible representation in the O_h group is $\Gamma_{15'}$ can be reduced to $A_{2u} + E_u$ symmetry in the D_{3d} group, since D_{3d} (group of L in the diamond structure) is a subgroup of O_h. So we need to look into the infrared activity of three-phonon processes in the diamond structure. This has been published in Ref. [70]. Table 6.1 lists the combinations of 2TO + TA phonons in Si and 3TO phonons in Ge which are infrared active [70]. Activity (M) is the coefficient of $\Gamma_{15'}$ in the reduction of the direct sum of symmetry elements of three-phonon combinations. Larger M corresponds to a more infrared active three-phonon process [70]. Table 6.1 shows that the combinations of 2TO + TA phonons are more IR-active than 3TO phonon processes.

The interaction will be stronger between the A_{2u} local mode and 2TO + TA phonons than with 3TO phonons. In addition, there are more channels for the A_{2u} mode to decay into 2TO + TA phonons, which results in a shorter lifetime of the oxygen mode in Si.

Activity (M)	Phonon combinations	Frequency (cm^{-1})
	Silicon	
3	$TO(X) + O(\Gamma) + TA(X)$	1129
6	$TO(L) + O(\Gamma) + TA(L)$	1122
3	$2TO(L) + TA(X)$	1134
6	$TO(L) + TO(X) + TA(L)$	1071
2	$2TO(X) + TA(X)$	1078
	Germanium	
1	$2TO(X) + O(\Gamma)$	856
3	$2TO(L) + O(\Gamma)$	888

Table 6.1: Three-phonon processes in Si and Ge close to the frequency of the asymmetric stretch mode of interstitial oxygen. The infrared activity M is also listed.

6.4 Conclusion

In conclusion, we have measured the vibrational lifetimes of the asymmetric stretch mode of oxygen isotopes in silicon and germanium. In silicon, the $^{17}O_i$ mode lies in the highest density of three-phonon states, which gives rise to a shorter lifetime (T_1 = 4.5 ps) than for the $^{16}O_i$ and $^{18}O_i$ modes ($T_1 \simeq 10$ ps). We also measured the lifetime of $^{16}O_i$ modes in Ge, which show a much longer lifetime, $T_1 = 125$ ps, than in Si. We argue that the oxygen modes in Si decay into 2TO + TA phonons, while they decay into 3TO phonons in Ge. These phonon combinations have different infrared

activities, which result in different coupling strengths and very different lifetimes. A more quantitative understanding of the vibrational energy relaxation and transfer channels in solids requires detailed knowledge of anharmonic coupling between LVM and lattice phonon modes and phonon density of states modified by impurities. The measured lifetimes presented here have great significance in elucidating the stability and diffusivity of impurities in semiconductors as well as complex formation and will generate renewed interest in the dynamics of energy dissipation from local modes into solid-state phonon bath.

Chapter 7

Summary and Future Work

7.1 Summary

The study of relaxation dynamics of local vibrational modes down to the picosecond timescale is a new emerging field. In this dissertation, we have studied in detail the vibrational lifetime of various defects in semiconductors by vibrational pump-probe spectroscopy. This study of vibrational lifetimes elucidates the decay dynamics of local vibrational modes and provides unique information about energy relaxation processes to solid-state phonon bath. According to our studies in this dissertation, there are five important factors which determine the lifetime of local vibrational modes: (1)*Order of decay channel*, (2)*symmetry of the accepting modes*, (3)*density of states of accepting phonon modes*, (4)*anharmonicity*, and (5)*defect structure*.

Vibrational lifetimes of H- and D-related bending modes are determined by the decay order, i.e., the decay time increases exponentially with increasing decay order. This provides an estimate of the lifetimes of many other hydrogen bending modes in solids. For instance, when the local mode couples to only one phonon, the decay time

109

is around 1 ps or less. Two-order decay of hydrogen bending modes corresponds to a decay time of ~10 ps, three-order processes correspond to 40-100 ps, while the decay time of four-order processes can be longer than 250 ps. This so-called energy-gap law shows that the lifetime of D-related bending modes are generally shorter than H-related bending modes. This result can explain the large H/D isotope effect in H-passivasted semiconductor devices.

In contrast, vibrational lifetimes of H-related stretch modes critically depend on defect structure. The interstitial-type defect H_2^* at 2062 cm^{-1} has a lifetime of 4.2 ps at 10 K, whereas the lifetime of the vacancy-type complex $HV \cdot VH_{(110)}$ at 2072 cm^{-1} is 2 orders of magnitude longer. The decay mechanism of stretch modes is more complicated than for bending modes. The accepting modes of hydrogen stretch modes can be phonons, bending modes, and/or pseudolocalized modes. More theoretical work is needed.

The study of interstitial oxygen and its isotope effects in Si and Ge shows that both density of states and symmetry of accepting modes are important to determine their vibrational lifetimes. The lifetimes of interstitial ^{16}O and ^{18}O mode is two times longer than ^{17}O mode in Si. A calculation of the three-phonon density of states shows that ^{17}O lies in the highest phonon density resulting in the shortest lifetime. The lifetime of ^{16}O modes in Ge is measured to be ~10 times longer than in Si. Symmetry analysis reveals that the accepting modes of interstitial oxygen in Si are more infrared active and have more decay channels than in Ge .

Until now, no first-principle calculations have been done of the vibrational life-

times of hydrogen or oxygen in crystalline semiconductors. The level of theoretical investigations into the dynamics of these modes is less advanced. We believe that the measured lifetimes presented in this dissertation provides an indispensable benchmark for future theoretical calculations.

7.2 Future Work

In this dissertation, the vibrational lifetimes of H- and O- related defects are investigated in intrinsic semiconductors and the decay of LVMs are governed by multiphonon relaxation processes. The decay of LVMs via electronic processes represents an exciting new direction for this project. Although the energy of LVMs is small compared to the band-gap of an intrinsic semiconductor, both p- or n- doped semiconductors and laser-induced free carriers provide energetically accessible electronic channels. The existence of electronic pathways will undoubtedly influence the population lifetimes and linewidths.

One of the most interesting systems is the O-H complex in ZnO, which is a wide-band gap semiconductor that has attracted tremendous interest for optical, electronic, and mechanical applications [142, 143]. It provides a possible alternative to GaN for use in optoelectronic devices. Bulk ZnO single crystals can be grown and they nearly always exhibits n-type conductivity. Recently, Van De Walle performed theorectical calculations and proposed that H impurity in ZnO is a shallow donor that may be introduced into the bulk during growth or processing [144]. This is unexpected be-

cause in all other semiconductors, interstitial hydrogen has been found to counteract the prevailing conductivity caused by extrinsic dopants. In ZnO, however, hydrogen occurs exclusively in the positive charge state, which can explain the typical n-type conductivity of ZnO [145, 146].

By annealing ZnO in H_2 gas at elevated temperature, McCluskey *et al.* have observed a vibrational line at 3326.3 cm^{-1} and have associated this line with O-H stretch mode of a H-related donor [147]. Figure 7.1 shows the structure and the absorption line of this stretch mode:
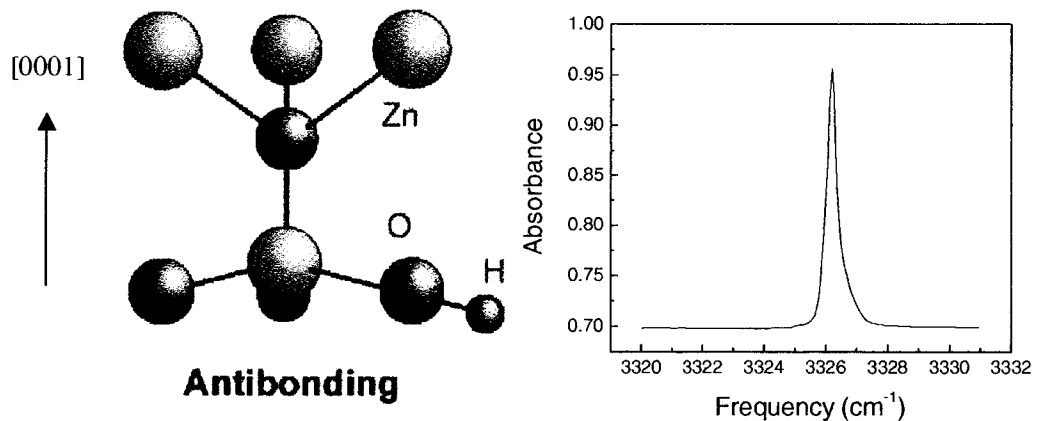
Figure 7.1: Structure of O-H bond in ZnO and absorption spectrum at 3326 cm^{-1} [151].

We note that the absorption line of the O-H vibrational mode at 3326.3 cm^{-1} is asymmetric. With decreasing concentration, the line becomes sharper and more symmetric. In boron-doped Si, this phenomenon was observed by M. Stovala [148]. The acceptor-H vibrational bands are asymmetric and broadened by a Fano interaction with the continuum absorption due to residual free carriers. Fano interaction

effects are well known in Raman studies of heavily doped materials. Both the Si optical phonon at 520 cm^{-1} and the B local-mode features at 620 and 644 cm^{-1} show pronounced Fano-interaction effects in Si with high free-carriers concentration [149, 150].

The O-H stretch mode at 3326 cm^{-1} is associated with the H-related donors. With decreasing the H concentration, the free-carrier concentration will also decrease. At low hydrogen concentration, the Fano-shape is less pronounced [151]. To the best of our knowledge, nobody has studied how this interaction between local mode and free carriers will affect the vibrational lifetime of local modes. It will be interesting to study how the vibrational lifetime will change with different H concentrations.

Through the temperature dependence of lifetime measurements, we learn about the relaxation channel. As discussed above, relaxation through free carriers may provide another channel for vibrational modes. The interaction between local mode and free carriers may increase the relaxation rate. This exciting new direction will lead to a better general understanding of relaxation mechanisms.

Bibliography

[1] S. K. Estreicher. Structure and dynanmics of point defects in crystalline silicon. *PHYSICA STATUS SOLIDI B*, 217:513, 2000.

[2] F. A. Cotton, G. Wilkinson, and P. L. Gaus. *Basic Inorganic Chemistry*. Wiley, New York, 1987.

[3] S. J. Pearton, J. W. Corbett, , and M. Stavola. *Hydrogen in Crystalline Semiconductors*. Springer-Verlag, Berlin, 1992.

[4] A. Van Wieringer and N. Warmholz. *Physica*, 22:849, 1956.

[5] T. Ichimiya and A. Furuichi. *Int. J. Appl. Radiat. Isot*, 19:573, 1968.

[6] Stefan K. Estreicher. Hydrogen-related defects in crystalline semiconductors: a theorist's perspective. *Materials Science and Engineering*, R14:319, 1995.

[7] J. J. Pankove and N. M. Johnson. *Hydrogen in Semiconductors I: semiconductors and semimetals. vol.34*. Academic Press, New York, 1991.

[8] S. M. Myers, M. I. Baskes, H. K. Birnbaum, G. G. Deleo J. W. Corbett, S. K. Estreicher, E. E. Haller, and S. J. Pearton. Hydrogen interactions with defects in crystalline solids. *Physical Review B*, 64:559, 1992.

[9] Norbert H. Nickel. *Hydrogen in Semiconductors II: semiconductors and semimetals. vol.61*. Academic Press, New York, 1999.

[10] Chris G. Van de Walle, P. J. H. Denteneer, Y. Bar-Yam, and S. T. Pantelides. Theory of hydrogen diffusion and reactions in crystalline silicon. *Physical Review B*, 39:10791, 1989.

[11] G.S. Higashi, Y.J. Chabal, G.W. Trucks, and K. Raghavachari. Ideal hydrogen termination of the Si (111) surface. *Applied Physics Letters*, 56:656, 1990.

[12] A. Stemans. Dissociation kinetics of hydrogen-passivated P_b defects at the (111)Si/SiO$_2$ interface. *Physical Review B*, 61:8393, 2000.

[13] Y. J. Chabal. *Physica B*, 170:447, 1991.

[14] K. L. Brower. *Physical Review B*, 38:9657, 1988.

[15] K. L. Brower. *Physical Review B*, 42:3444, 1990.

[16] M. Stavola. *Hydrogen in Semiconductors II: semiconductors and semimetals. vol.51.* Academic Press, New York, 1999.

[17] J. W. Corbett, S. N. Sahu, T. Si. Shi, and L. C. Snyder. *Physics Letters*, 93A:303, 1983.

[18] A. W. R. Leitch, V. Alex, and J. Weber. Raman spectroscopy of hydrogen molecules in crystalline silicon. *Physical Review Letters*, 81:421, 1998.

[19] R. E. Pritchard, M. J. Ashwin, J. H. Tucker, and R. C. Newman. Isolated interstitial hydrogen molecules in hydrogenated crystalline silicon. *Physical Review B*, 57:15048, 1998.

[20] E Elinor Chen, Michael Stavola, W. Beall Fowler, and J. Anna Zhou. Rotation of molecular hydrogen in Si: Unambiguous identification of ortho-H_2 and para-D_2. *Physical Review Letters*, 88:245503, 2002.

[21] K. J. Chang and D. J. Chadi. Diatomic-hydrogen-complex diffusion and self-trapping in crystalline silicon. *Physical Review Letters*, 62:937, 1989.

[22] J. D. Holbech, B. Bech Nielsen, R. Jones, P. Sitch, and S. Öberg. H_2^* defect in crystalline silicon. *Physical Review Letters*, 71:875, 1993.

[23] J. Anna Zhou and Michael Stavola. Symmetry of molecular H_2 in Si from a uniaxial stress study of the 3618.4 cm^{-1} vibrational line. *Physical Review Letters*, 83:1351, 1999.

[24] J. Anna Zhou, E. Chen, and Michael Stavola. *Physica B*, 273-274:200, 1999.

[25] Fumio Shimura. *Oxygen in Silicon.* Academic Press, London, 1994.

[26] W. Kaiser, H. L. Frisch, and H. Reiss. Mechanism of the formation of donor states in heat-treated silicon. *Physical Review*, 112:1546, 1958.

[27] Y. Takano and M. Maki. *Semiconductor silicon.* Electrochemical Society, NJ, 1973.

[28] P. Gaworzewshi, E. Hild, F. G. Kirscht, and L. Vecsernyes. *PHYSICA STATUS SOLIDI A*, 85:133, 1984.

[29] J. Wagner, K. Thonke, and R. Sauer. *Physical Review B*, 29:7051, 1984.

[30] W. Kaiser and P. H. Keck. *Journal of Applied Physics*, 28:882, 1957.

[31] W. W. Keller. *Journal of Applied Physics*, 55:3471, 1984.

[32] M .D. McCluskey. Local vibrational modes of impurities in semiconductors. *Journal of Applied Physics*, 87:3593, 2000.

[33] B. N. Brockhouse and P. K. Iyengar. *Physical Review*, 111:747, 1958.

[34] A. S. Barker Jr. and A. J. Siever. *Review of Modern Physics*, 47:S1, 1975.

[35] R. S. Leigh and R. C. Newman. *Semicond. Sci. Technol.*, 3:84, 1988.

[36] Y. J. Chabal. *Surf. Sci. Rep.*, 8:211, 1988.

[37] Y. J. Yan and S. Mukamel. *Journal of Chemical Physics*, 94:179, 1991.

[38] G. Lüpke, N. H. Tolk, and L. C. Feldman. *Journal of Applied Physics*, 92:2317, 2003.

[39] C. L. Tang and L. K. Cheng. *Fundamentals of Optical Parametric Processes and Oscillators*. Harwood Academic, Amasterdam, 1995.

[40] J. Y. Zhang, J. Y. Huang, and Y. R. Shen. *Optical Parametric Generation and Amplification*. Harwood Academic, Amasterdam, 1995.

[41] W. B. Colson, E. D. Johnson, M. J. Kelley, and H. A. Schwettman. *PHYSICS TODAY*, 55:35, 2002.

[42] G. R. Neil, C. L. Bohn, S. V. Benson, G. Biallas, D. Douglas, H. F. Dylla, R. Evans, J. Fugitt, A. Grippo, J. Gubeli, R. Hill, K. Jordan, R. Li, L. Merminga, P. Piot, J. Preble, M. Shinn, T. Siggins, R. Walker, and B. Yunn. Sustained kilowatt lasing in a free-electron laser with same-cell energy recovery. *Physical Review Letters*, 84:662, 2000.

[43] P. Guyot-Sionnest, P. Dumas, Y. J. Chabal, and G. S. Higashi. Lifetime of an adsorbate-substrate vibration: H on Si (111). *Physical Review Letters*, 64:2156, 1990.

[44] M. Budde, G. Lüpke, C. Parks Cheney, N. H. Tolk, and L. C. Feldman. Vibrational lifetime of bond-center hydrogen in crystalline silicon. *Physical Review Letters*, 55:1452, 2000.

[45] B. H. Bransden and C. J. Joachain. *Physics of Atoms and Molecules*. Prentice Hall, Harlow, 2003.

[46] S. A. Egorov and J. L. Skinner. On the theory of multiphonon relaxation rates in solids. *Journal of Chemical Physics*, 103:1533, 1995.

[47] R. Kubo and Y. Toyozawa. *Prog. Theoret. Phys.*, 13:160, 1955.

[48] Y. E. Perlin. *Sov. Phys. Usp.*, 6:542, 1964.

[49] T. Miyakawa and D. L. Dexter. *Physical Review B*, 1:2961, 1970.

[50] F. K. Fong, S. L. Naberhuis, and M. M. Miller. *Journal of Chemical Physics*, 56:4020, 1972.

[51] S. H. Lin. *Journal of Chemical Physics*, 65:1053, 1976.

[52] S. H. Lin. *Radiationless Transitions*. Academic Press, New York, 1980.

[53] R. Englman. *Non-radiative Decay of Ions and Molecules in Solids*. North Holland, Amsterdam, 1979.

[54] B.-Z. Zhang, Y.-X. Li, M.-R. Lin, and W.-J. Chen. *Chin. Phys.*, 10:876, 1990.

[55] F. K. Fong. *Theory of Molecular Relaxation*. Wiley, New York, 1975.

[56] A. Nitzan and J. Jortner. *Mol. Phys.*, 25:713, 1973.

[57] A. Nitzan, S. Mukamel, and J. Jortner. *Journal of Chemical Physics*, 60:3929, 1974.

[58] R. P. Feynman and A. R. Hibbs. *Quantum Mechanics and Path Integrals*. McGraw-Hill, New York, 1965.

[59] L. A. Riseberg and H. W. Moos. *Physical Review Letters*, 19:1423, 1967.

[60] L. A. Riseberg and H. W. Moos. *Physical Review*, 174:429, 1968.

[61] P. M. Morse. *Physical Review*, 34:57, 1929.

[62] B. Pajot, B. Clerjaud, and Z.-J. Xu. *Physical Review B*, 59:7500, 1999.

[63] G. Herzberg. *Molecular Spectra and Molecular Structure. II. Infrared and Raman Spectra of Polyatomic Molecules*. Van Nostrand, New York, 1990.

[64] J.-K. Wang, C.-S. Tsai, C.-E. Lin, and J.-C. Lin. Vibrational dephasing dynamics at hydrogenated and deuterated semiconductor surfaces: Symmetry analysis. *Journal of Chemical Physics*, 113:5041, 2000.

[65] T. Inui, Y. Tanabe, and Y. Onodera. *Group Theory and Its Applications in Physics*. Springer-Verlag, Berlin, 1990.

[66] Peter Y. Yu and Manuel Cardona. *Fundamentals of Semiconductors : Physics and Materials Properties*. Springer-Verlag, Berlin, 1996.

[67] H. Kuzmany. *Solid-State Spectroscopy: An Introduction*. Springer-Verlag, Berlin, 1998.

[68] L. Hsu, M. D. McCluskey, and J. L. Lindstro. Resonant interaction between localized and extended vibrational modes in Si: ^{18}O under pressure. *Physical Review Letters*, 90:095505, 2003.

[69] Joseph L. Birman. Space group selection rules: Diamond and zinc blende. *Physical Review*, 127:1093, 1962.

[70] Joseph L. Birman. Theory of infrared and Raman processes in crystals: Selection rules in diamond and zincblende. *Physical Review*, 131:1489, 1963.

[71] YR. J. Bell. *Introductory Fourier Transform Spectroscopy*. Academic Press, New York, 1972.

[72] M. R. X. de Barros, R. S. Miranda, T. M. Jedju, and P. C. Becker. High-repetitionrate femtosecond mid-infrared pulse generation. *Optics Letters*, 20:480, 1995.

[73] P. C. M. Planken, E. Snoeks, L. D. Noordam, H. G. Muller, and H. B. van den Linden van den Heuvell. Generation of intense sub-picosecond pulses in the midinfared. *Optical Communications*, 85:31, 1991.

[74] V. Petrov and F. Noack. Tunable femtosecond optical parametric amplifier in mid-infrared with narrow-band seeding.

[75] George R. Neil and Lia Merminga. Technical approaches for high-average-power free-electron lasers. *Review of Modern Physics*, 74:685, 2002.

[76] E. L. Saldin, E. A. Schneidmiller, and M. V. Yurkov. *The Physics of Free Electron Lasers*. Springer-Verlag, New York, 2000.

[77] A. E. Siegman. *Lasers*. University Science Books, Mill Valley, CA, 1986.

[78] M. Budde, B. Bech Nielsen, R. Jones, J. Goss, and S.Öberg. Local modes of the H_2^* dimer in germanium. *Physical Review B*, 54:5485, 1996.

[79] J. F. Ziegler, J. P. Biersack, and U. Littmark. *The stopping and Ranges of Ions in Solids*. Pergamon Press, New York, 1985.

[80] J. Michel, J. R. Niklas, and J. M. Spaeth. Structure of thermal donors (NL8) in silicon: A study with electron-nuclear double resonance. *Physical Review B*, 40:1732, 1989.

[81] A. Stesmans. Interaction of p_b defects at the (111)Si/SiO$_2$ interface with molecular hydrogen: Simultaneous action of passivation and dissociation. *Journal of Applied Physics*, 88:489, 2000.

[82] J. W. Lyding, K. Hess, and I. C. Kizilyalli. *Applied Physics Letters*, 68:2526, 1996.

[83] J. Chevallier, M. Barbé, E. Constant, D. Loridant-Bernard, and M. Constant. Strong isotope effects in the dissociation kinetics of Si-H and Si-D complexes in GaAs under ultraviolet illumination. *Applied Physics Letters*, 75:112, 1999.

[84] T.-C. Shen, C. Wang, G. C. Abeln, J. R. Tucker, J. W. Lyding, Ph. Avouris, and R. E. Walkup. *Science*, 268:1590, 1995.

[85] Ph. Avouris, R. E. Walker, A. R. Rossi, H. C. Akpati, P. Nordlander, T. C. Shen, G. C. Abeln, and J. W. Lyding. *Chemical Physics Letter*, 254:148, 1996.

[86] J.-H. Wei, M.-S. Sun, and S.-C. Lee. A possible mechanism for improved light-induced degradation in deuterated amorphous-silicon alloy. *Applied Physics Letters*, 71:1498, 1997.

[87] K. Hess, L. F. Register, B. Tuttle, J. Lyding, and I. C. Kizilyalli. *Physica (Amsterdam)*, 3E:1, 1998.

[88] E. T. Foley, A. F. Kam, J. W. Lyding, and Ph. Avouris. *Physical Review Letters*, 80:1336, 1998.

[89] R. Biswas, Y.-P. Li, and B. C. Pan. Enhanced stability of deuterium in silicon. *Applied Physics Letters*, 72:3500, 1998.

[90] C. G. Van de Walle and W. B. Jackson. *Applied Physics Letters*, 68:2526, 1996.

[91] C. G. Van de Walle and R. A. Street. *Physical Review B*, 49:14766, 1994.

[92] Zhi Chen, Jun Guo, and Pangleen Ong. Evidence for energy coupling from the Si-D vibration mode to the Si-Si and Si-O vibration modes at the SiO_2/Si interface. *Applied Physics Letters*, 83:2151, 2003.

[93] An Shih, Si-Chen Lee, and Chih ta Chia. Evidence for coupling of Si-Si lattice vibration and Si-D wagging vibration in deuterated amorphous silicon. *Applied Physics Letters*, 74:3347, 1999.

[94] G. Lüpke, X. Zhang, B. Sun, A. Fraser, N. H. Tolk, and L. C. Feldman. Structure-dependent vibrational lifetimes of hydrogen in silicon. *Physical Review Letters*, 88:135501, 2002.

[95] A. Nitzan, S. Mukamel, and J. Jortner. *Journal of Chemical Physics*, 63:200, 1975.

[96] U. Happek, C. E. Mungan, W. von der Osten, and A. J. Sievers. Relaxation of the CN^- stretching vibration in silver halides: The role of accepting modes. *Physical Review Letters*, 72:3903, 1994.

[97] E. Tuncel and H. Sigg. Temperature dependence of the vibrations of the si-h complex in GaAs and AlAs. *Physical Review B*, 58:5225, 1993.

[98] B. Pajot. private communication.

[99] J. Vetterhöffer and J. Weber. Hydrogen passivation of shallow donors S, Se, and Te in GaAs. *Physical Review B*, 53:12835, 1996.

[100] *Note.* The natural isotope of S is dominated by ^{32}S(95.02%), so the isotope broadening can be neglected. The isotope broadening is much larger for Se(Te)-H(D) modes due to the comparable aboundances: ^{82}Se(9.2%), ^{80}Se(49.8%), ^{78}Se(23.5%), ^{77}Se(7.6%), ^{76}Se(9.0%),^{74}Se(0.9%) and ^{130}Te(34.5%), ^{128}Te(31.7%), ^{126}Te(18.7%), ^{125}Te(7%), ^{124}Te(4.6%), ^{123}Te(0.9%), ^{122}Te(2.5%), ^{120}Te(0.1%).

[101] M. Budde, G. Lüpke, E. Chen, X. Zhang, N. H. Tolk, L. C. Feldman, E. Tarhan, A. K. Ramdas, and M. Stavola. Lifetimes of hydrogen and deuterium related vibrational modes in silicon. *Physical Review Letters*, 87:145501, 2001.

[102] H. J. Stein. Bonding and thermal stability of implanted hydrogen in silicon. *Journal of Electronic Materials*, 4:159, 1975.

[103] H. J. Stein. Vacancies and the chemical trapping of hydrogen in silicon. *Physical Review Letters*, 43:1030, 1979.

[104] G. R. Bai, M. W. Qi, L. M. Xie, and T. S. Shi. *Solid State Commum.*, 56:277, 1985.

[105] T. S. Shi, L. M. Xie, G. R. Bai, and M. W. Qi. *PHYSICA STATUS SOLIDI B*, 131:511, 1985.

[106] X. T. Meng, Y. C. Chang, and Y. D. Fan. *PHYSICA STATUS SOLIDI A*, 101:619, 1987.

[107] M. Budde, B. Bech Nielsen, P. Leary, J. Goss, R. Jones, P. R. Briddon, and S.Öberg.

[108] H. Xu. *Physical Review B*, 46:1403, 1992.

[109] C. G. Van de Walle. *Physical Review B*, 49:4579, 1994.

[110] M. A. Roberson and S. K. Estreicher. *Physical Review B*, 49:17040, 1994.

[111] M. Suezawa. *Physical Review B*, 63:035201, 2001.

[112] P. Stallinga, P. Johannesen, S. Herstrom, B. Bech Nielsen, and J. R. Byberg. *Physical Review B*, 58:3842, 1998.

[113] C. Flensburg and R. F. Stewart. *Physical Review B*, 60:284, 1999.

[114] Marjolein van der Voort, Chris W. Rella, Lex F. G. van der Meer, Andrey V. Akimov1, and Jaap I. Dijkhuis. Dynamics of Si-H vibrations in an amorphous environment. *Physical Review Letters*, 84:1236, 2000.

[115] M. Budde. unpublished.

[116] B. N. J. Persson and Ph. Avouris. *Surf. Sci.*, 390:45, 1997.

[117] R. Jones. http://newton.ex.ac.uk/research/qsystems/jones/projects/oxygen/.

[118] W. Kaiser, P. H. Keck, and C. F. Lange. *Physical Review*, 101:1264, 1956.

[119] H. J. Hrostowshi and R. H. Kaiser. *Physical Review*, 107:966, 1957.

[120] W. Kaiser. *J. Phys. Chem. Solids*, 23:255, 1962.

[121] J. W. Corbett, R. S. McDonald, and G. D. Watkins. *J. Phys. Chem. Solids*, 25:873, 1964.

[122] B. Pajot and P. Clauws. In O. Engstrom, editor, *Proceedings of the 18th International Conference on the Physics of Semiconductors*, page 911, Singapore, 1987. World Scientific.

[123] M. Gienger, M. Glaser, and K. La beta mann. *Solid State Commun.*, 86:285, 1993.

[124] A. Lizon-Nordstrom and F. Yndurain. *Solid State Commun.*, 89:819, 1994.

[125] A. J. Mayur, M. D. Sciacca, M. K. Udo, A. K. Ramdas, K. Itoh, J. Wolk, and E. E. Haller. *Physical Review B*, 49:16293, 1994.

[126] E. Artacho and F. Yndurain. *Mater. Sci. Forum*, 196-201:103, 1995.

[127] A. J. Mayur, M. D. Sciacca, M. K. Udo, A. K. Ramdas, K. Itoh, J. Wolk, and E. E. Haller. *Physical Review B*, 49:16293, 1994.

[128] R. Jones, A. Umerski, and S. Oberg. *Physical Review B*, 45:11321, 1992.

[129] D. R. Bosomworth, W. Hayes, A. R. L. Spray, and G. D. Watkins. *Proc. R. Soc. London Ser. A*, 317:133, 1970.

[130] M. Stavola. *Applied Physics Letters*, 44:514, 1984.

[131] B. Pajot, H. J. Stein, B. Cales, and C. Naud. *J. Electrochem. Soc.*, 132:3034, 1985.

[132] Hiroshi Yamada-Kaneta, Chioko Kaneta, and Tsutomu Ogawa. Theory of local-phonon-coupled low-energy anharmonic excitation of the interstitial oxygen in silicon. *Physical Review B*, 42:9650, 1990.

[133] B. Pajot, E. Artacho, C. A. J. Ammerlaan, and J. M. Spaeth. Theory of local-phonon-coupled low-energy anharmonic excitation of the interstitial oxygen in silicon. *J. Phys., Condens. Matter.*, 7:7077, 1995.

[134] Hiroshi Yamada-Kaneta. Theory of local-phonon-coupled low-energy anharmonic excitation of the interstitial oxygen in silicon. *Physica B*, 308-310:309, 2001.

[135] M. Ramamoorthy and S. T. Pantelides. Coupled-barrier diffusion: The case of oxygen in silicon. *Physical Review Letters*, 76:267, 1996.

[136] D. D. Dlott. *Laser Spectroscopy of Solids II, edited by W. M. Yen, chapter 5.* Springer-Verlag, Berlin, 1989.

[137] Paolo Giannozzi, Stefano de Gironcoli, Pasquale Pavone, and Stefano Baroni. Ab initio calculation of phonon dispersions in semiconductors. *Physical Review B*, 43:7231, 1991.

[138] Siqing Wei, Changlin Li, and M. Y. Chou. Ab initio calculation of thermodynamic properties of silicon. *Physical Review B*, 50:14587, 1994.

[139] J. F. Angress, A. R. Goodwin, and S. D. Smith. *Proc. R. Soc. London*, A287:64, 1965.

[140] Jiro Kato, Kohei M. Itoh, Hiroshi Yamada-Kaneta, and Hans-Joachim Pohl. Host isotope effect on the localized vibrational modes of oxygen in isotopically enriched ^{28}Si, ^{29}Si, and ^{30}Si single crystals. *Physical Review B*, 68:035205, 2003.

[141] B. Pajot, P. Clauws, J. L. Lindstrom, and E. Artacho. O isotope effects and vibration-rotation lines of interstitial oxygen in germanium. *Physical Review B*, 62:10165, 2000.

[142] D. C. Look. Recent advances in ZnO materials and devices. *Materials Science and Engineering B*, 80:283, 2001.

[143] D. P. Norton, Y. W. Heo, M. P. Ivill, K. Ip, S. J. Pearton, M. F. Chisholm, and T. Steiner. *Materials Today*, 7:34, 2004.

[144] C. G. Van de Walle. Hydrogen as a cause of doping in zinc oxide. *Physical Review Letters*, 85:1012, 2000.

[145] D.M. Hofmann, A. Hofstaetter, F. Leiter, H. Zhou, F. Henecker, B. Meyer, S.B. Orlinskii, J. Schmidt, and P.G. Baranov. Hydrogen: A relevant shallow donor in zinc oxide. *Physical Review Letters*, 88:045504, 2002.

[146] S. F. J. Cox, E. A. Davis, S. P. Cottrell, P. J. C. King, J. S. Lord, J. M. Gil, H. V. Alberto, R. C. Vil?o, J. Piroto Duart, N. Ayres de Campos, A. Weidinger, R. L. Lichti, and S. J. C. Irvine. Experimental confirmation of the predicted shallow donor hydrogen state in zinc oxide. *Physical Review Letters*, 86:2601, 2001.

[147] M.D. McCluskey, S.J. Jokela, K.K. Zhuravlev, P.J. Simpson, and K.G. Lynn. Infrared spectroscopy of hydrogen in ZnO. *Applied Physics Letters*, 81:3807, 2002.

[148] M. Stavola, S. J. Pearton, J. Lopata, and W. C. Dautremont-Smith. *Physical Review B*, 37:8313, 1988.

[149] F. Cerdeira, T. A. Fjeldly, and M. Cardona. *Physical Review B*, 8:4734, 1973.

[150] F. Cerdeira, T. A. Fjeldly, and M. Cardona. *Physical Review B*, 9:4344, 1974.

[151] G. Alvin Shi, Marjan Saboktakin, Michael Stavola, and S. J. Pearton. "Hidden hydrogen" in as-grown ZnO. *Applied Physics Letters*, 85:5601, 2004.

VITA

Baozhou Sun

Baozhou Sun was born on November 13, 1977 in Wuhan, Hubei province of China. He entered Jilin University in Changchun in 1996 and obtained his Bachelor degree in Electronic Engineering in 2000. In August of the same year, he entered graduate school in the Department of Applied Science at the College of William and Mary, where he received his Master degree in 2002. He married his wife, Min Huang on August 28, 2004. Sun completed his Ph.D degree under the supervision of Dr. Gunter Lüpke in 2005. During his study at William and Mary, Sun was elected to be a member of Sigma Xi in 2005 and he has been a member of American Physical of Society since 2003.

124